A proposed Climatic scenario for the Martian Mid-Latitude Glaciation

Jean-Baptiste Madeleine

Advisors :

James W. Head III

Planetary Group, Brown University

François Forget

Laboratoire de Météorologie Dynamique, Paris

March - August 2006

Abstract

Recent geological observations in the northern mid-latitudes of Mars show evidence for past glacial activity during the Late Amazonian period (~ 300 Ma), similar to the integrated glacial systems in the Dry Valleys of Antarctica. The accumulation of ice required to create the observed glacial flows points to an intense regional glaciation due to spin orbital parameter-driven climate changes. The LMD (Laboratoire de Météorologie Dynamique) Martian GCM (General Circulation Model) is able to reproduce with an excellent agreement the present-day water cycle, and to predict past deposition of ice consistent with geological observations. However, the mid-latitude glaciation has never been observed by the model. Here, we study the response of the GCM to different orbital configurations and water ice reservoirs, and show that during periods of high mean obliquity ($\epsilon = 25 - 35^o$), broad scale glaciation in the mid-latitudes occurs if we suppose an equatorial source of water on the great volcanoes and a high dust opacity ($\tau = 1 - 2.5$). Surface ice deposits show a strong correlation with the geological observations, the inhomogeneity of distribution within the mid-latitude band resulting from the topographic forcing of stationary planetary waves and transient weather systems. Ice accumulation rates of $\sim 10 mm.yr^{-1}$ can account for the formation of a $500 - 1000$m thickness regional ice sheet within an order of magnitude of the observations. These results allow us to propose a scenario for the martian mid-latitude glaciation.

Résumé

De récentes études géologiques de Mars effectuées entre 20^oN et 50^oN ont permi d'identifier une intense période de glaciation durant la fin de l'Amazonien (~ 300 Ma), montrant une géomorphologie très proche des Dry Valleys en Antarctique. Les écoulements observés nécessitent une considérable accumulation de glace dans cette bande de latitude durant d'intenses changements climatiques dus aux larges variations d'obliquité de la planète. Le Modèle de Circulation Générale (GCM) de Mars développé au LMD (Laboratoire de Météorologie Dynamique) permet une étude détaillée du cycle de l'eau martien et reproduit de nombreux dépôts glaciaires avec une impressionnante exactitude. Cependant, les dépôts des moyennes latitudes n'ont jamais été expliqués jusqu'à présent. Nous avons donc étudié la réponse du cycle de l'eau martien à de nombreuses configurations orbitales et réserves d'eau en surface, et ainsi trouvé un mécanisme climatique à l'origine de la glaciation lorsqu'une source d'eau est initialement placée au pied d'Olympus Mons et des volcans de Tharsis, pour des valeurs d'obliquité comprises entre 25 et 35^o, et d'opacité en poussières comprise entre 1 et 2.5. Les zones d'accumulation de glace sont en excellent accord avec les observations géologiques, et s'avèrent contrôlées par le forçage topographique des ondes stationnaires et baroclines. Des taux d'accumulation de glace d'environ 10 mm par an peuvent permettre le développement d'une calotte de 500-1000 m d'épaisseur dans les régions de forte glaciation, un résultat qui s'avère en accord avec les observations géologiques. Nous finissons donc par décrire un scénario climatique qui pourrait expliquer cette intense glaciation dans le passé récent de Mars.

CONTENTS

CHAPTER 1

Introduction

Amazonian climate-related processes

Since the arrival of Mariner 9 in 1971 and the discovery of wonderful valley networks and channels such as Nirgal Vallis (30^oS-35^oW - map B.1), a large variety of geomorphological features has revealed the essential role of water in Martian history. During the Noachian period (4.6 - 3.5 Gyr), valley networks, created by running of liquid water, formed in the old uplands of Mars and have been associated with a "warm and wet" early martian climate. After a transition to a cold and dry climate, gigantic outflow channels [Masson et al., 2001], resulting from the release of groundwater by tectonic cracking of the cryosphere, appeared near the Chryse-Acidalia basin (20^oN-30^oW - map B.1), in Elysium Planitia (10^oN-150^oE), east of Hellas Basin (30^oS-90^oE) and south of Amazonis Planitia (15^oN-180^oW), and converged into the northern lowlands, mostly during the Hesperian period (3.5 - 3 Gyr). Maybe the most impressive proof of the large amount of liquid water on Mars has been discovered by Opportunity in Meridiani Planum (2^oS-6^oW), where the rover saw evidence for depositional processes by liquid water, and distinct sedimentary units in the Burns Cliff outcrop (see image D.1 and [Squyres and Knoll, 2005]).

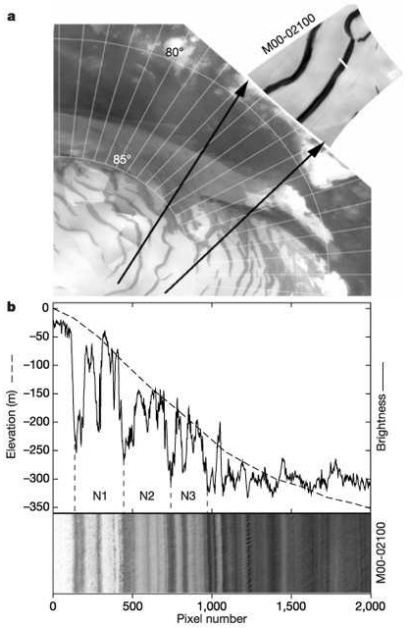

Figure 1.1: PLDs
a) Wide-angle MOC image of the north polar cap
b) Narrow-angle MOC image of the alternating layers
From [Laskar et al., 2002].

More recently in Martian history, glacial and periglacial landforms [Head et al., 2001, Masson et al., 2001] also indicate a significant resurfacing by water. These landforms, mainly created during the Amazonian period (3 Gyr - today), have a clear atmospheric origin, and thus represent an integrated resurfacing of Mars by major climatic changes.

The main glacial record of the past climatic changes is given by the North polar cap, where alternating dark and bright layers [Laskar et al., 2002, Milkovich and Head, 2005] contain a climatic signal (see the Polar Layered Deposits (PLDs) in figure 1.1), similar to the terrestrial Milankovitch cycles observed in oceanic sediments or polar ice cores. These dark and bright layers would be the result of alternating sublimation and deposition periods (the sublimation leaving a dark dust lag), driven by the large spin-axis and orbital variations of Mars (see section 3.1).

A second major glacial landform of the high latitudes is the polar mantling deposit [Head et al., 2003b] of both hemispheres. These deposits show a "basketball" texture resulting from the past degradation of surface water-ice, and are latitude dependent ($30-60^o$ latitude band), suggesting an atmospheric origin of the sublimated deposits.

Finally, in the northern mid-latitudes, geological evidence for significant glaciation is found all along the dichotomy boundary[1], and also in the southern mid-latitudes, in the eastern part of Hellas basin and Argyre Planitia. A map of the northern mid-latitude glaciation is given in figure 1.2.

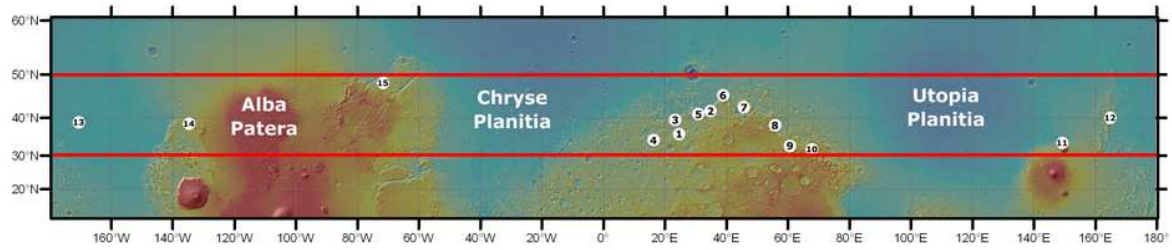

Figure 1.2: Distribution of the major glacial regions all along the dichotomy boundary.
From [Head and Marchant, 2006].

All the different pointed regions in figure 1.2 show evidence for glacial activity, through 1) lobate debris aprons (LDA), resulting from ice-assisted mass wasting of topographic highs, and 2) lineated valley fill (LVF), formed by convergence of debris-covered glaciers flowing down individual alcoves [Head and Marchant, 2006]. The mechanism proposed by [Head et al., 2006b] is the preferential accumulation of snow in preserved alcoves and the falling of debris onto the ice to form debris-covered glaciers, which merge into the main valleys, resulting in a whole integrated glacial system as found on Earth, for example in the Dry Valleys of Antarctica. An excellent example is given in figure 1.3, where a T-shaped glacial system is sustained by different local alcoves and a 15-km-diameter crater (panel 1. arrow A, C, E), resulting in a convergence of the streamlines (panel 2.) into a lobate distal glacier (panel 1. arrow I). In the western part of the T, a lineated valley fill emerges from a smaller valley and is carried eastward by the general flow (panel 1. arrow G). By analyzing high resolution images of the Deuteronilus-Protonilus region (40^oN-30^oE) and developing new glacial identification criteria, [Head et al., 2006a] found geological evidence for past regional glaciation, and came to the conclusion that current lineated valley fill could be remnants of a regional ice sheet [Head et al., 2006a], formed by major episodes of precipitation in the mid-latitudes.

[1]The topographic slope between the northern lowlands and the southern uplands.

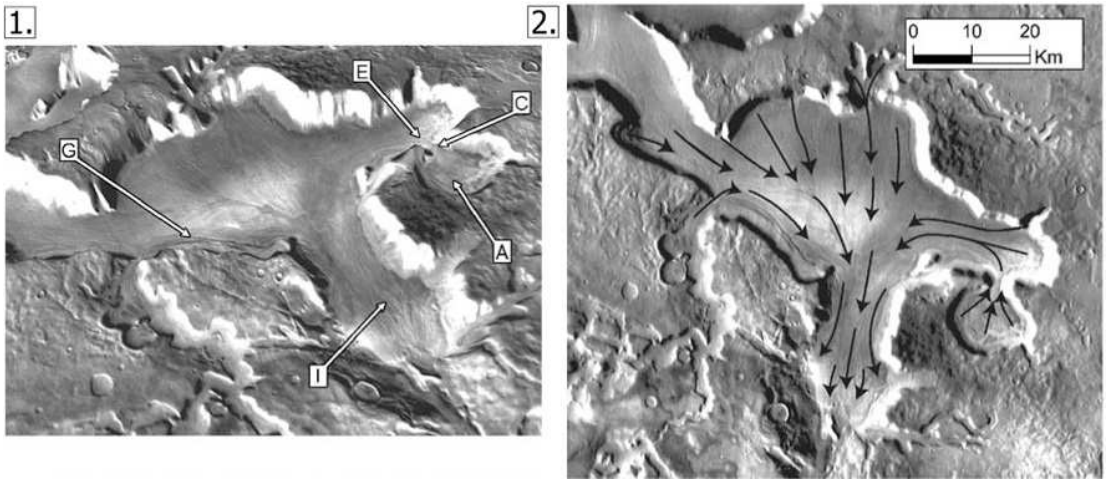

Figure 1.3: Example of integrated glacial system in the southern Deuteronilus Mensae region. From [Head et al., 2006a].

The sublimation of a thick layer of the North polar cap during periods of high polar insolation has a significant impact on the martian water cycle. It has been shown through GCM modeling that the formation of tropical mountain glaciers on the western flanks of Olympus Mons [Milkovich et al., 2006], Arsia Mons [Shean et al., 2005] and other Tharsis volcanoes, is a direct consequence of the sublimation of the North polar cap during periods of high obliquity (see section 3.1.2 and [Forget et al., 2006]). The latitude-dependent mantling deposits have also been reproduced by the LMD GCM by replacing the north polar cap by an equatorial source of water (see chapter 3 and [Levrard et al., 2004]).

However, the geological evidence for a wide mid-latitude glaciation and significant ice accumulation along the dichotomy boundary has not been explained by the General Circulation Model.

The purpose of this study is to understand the climatic origin of this large mid-latitude glaciation by using the LMD General Circulation Model, and to test our hypothesis by comparing the simulated ice accumulations with the glacial observations.

After introducing the fundamental aspects of the martian atmosphere and the GCM dynamics, we thus propose a meteorological mechanism accounting for a broad scale mid-latitude glaciation, and test the robustness of the results by a detailed comparison with geological observations. In the light of the geological and climatic conclusions, we also propose an updated scenario for the Martian Ice Ages.

CHAPTER 2

The General Circulation Model

Rewriting parts of Amazonian history

Throughout Martian history, three main forces have been acting to shape the surface we observe today : impact cratering, volcanism, and the water cycle. As opposed to the Earth, the Martian atmosphere has been evolving for millions of years over a relatively unchanged topography, without the huge inertia and response imposed by oceans. Consequently, with the present knowledge of geophysical laws, the paleoclimate of Mars can be predicted over the last several millions of years, and give major insights into Amazonian history.

To predict the Amazonian climate of Mars, we use the LMD General Circulation Model (GCM) which is able to reproduce a water cycle in excellent agreement with observations. Here we describe the main equations and mechanisms of the GCM, before exploring its response to past orbital conditions in chapter 3.

2.1 A desert Earth

During November 2004, around martian aphelion ($L_s \simeq 74^o$), the Mars Exploration Rover Opportunity took this image of majestic cirrus (see D.1), over the wall of Endurance Crater. The purpose of this section is simply to understand how these clouds formed and how we can predict their formation with the GCM, before studying in chapter 3 the key role they played during the Amazonian.

2.1.1 Martian environment

Mars is located at approximately 230.10^6 km from the Sun, and thus receives roughly two times less insolation than the Earth (see table A.1). The equilibrium between the incoming solar flux caught by the planet $\pi r^2(1-A)F_o$ and its total black body emission $4\pi r^2\sigma T_{eq}^4$ results in an equilibrium temperature $T_{eq} = (\frac{F_o}{4\sigma}(1-A))^{\frac{1}{4}}$ equal to 210 K (with a mean

albedo of 0.25 and a solar constant of $594\ W.m^{-2}$). The atmosphere is mainly composed of CO_2 (95%), with a total column of water around $10\mu m$, and a mean surface pressure of only $6.1hPa$. For comparison, the mean terrestrial surface pressure is $1013hPa$ and the order of magnitude of the water column is a centimeter. As opposed to the Earth where the dense and humid atmosphere modifies the temperature profile by latent heat release, the thin and dry martian atmosphere has a very low atmospheric heat capacity, resulting in large diurnal temperature variations.

If we look at the phase diagram of CO_2 and H_2O with these orders of magnitude in mind, we realize two major phenomena of interest in the martian atmosphere. First, given the large surface temperature range (140-300 K) and this low surface pressure, CO_2 can condense at both poles (see figure 2.1), pumping this main atmospheric constituent and creating large surface pressure variations (around $1hPa$). Secondly, the atmosphere is dry, but always close to saturation, as indicated by the $10\mu m$ and $100\mu m$ water vapor pressure lines on figure 2.1. The atmospheric water vapor can condense and form solid ice crystals, which can sedimentate and build up on the surface, supplying both polar caps.

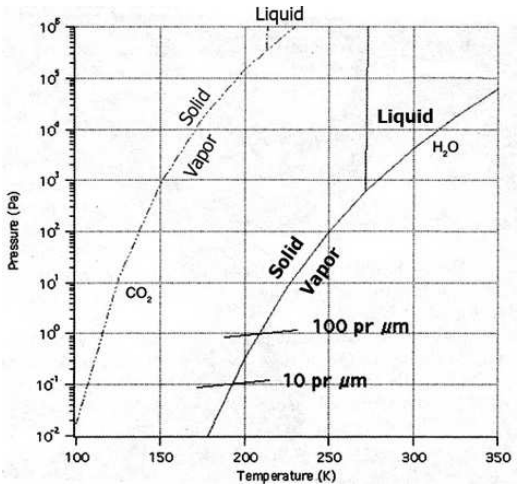

Figure 2.1: CO_2 and H_2O phase diagrams

From [Read and Lewis, 2004]

This atmosphere is stably stratified by a gravity of $3.72m.s^{-2}$ via the hydrostatic equilibrium $\partial_z p = -\rho g$, and supposing that it obeys the equation of state for a perfect gas $p = \rho RT$, we end up with the vertical pressure $p(z) = p_o \exp -\frac{z}{H_p}$ and a scale height $H_p = \frac{RT_e}{g} \simeq 10.8km$. The differential equator-pole heating create a Hadley circulation modified by a planetary rotation rate Ω that is almost equal to the Earth, establishing a well-known axisymetric circulation with a Rossby number of 0.2.

The martian obliquity ϵ (angle between the spin axis and the ecliptic plane) 25.19^o is close to the terrestrial value (23.93^o) and the high eccentricity of 0.093 (deviation from a circular orbit) favors the insolation of the southern hemisphere, the perihelion occuring at a solar longitude[1] of $\sim 250^o$ (later called the argument of perihelion L_p).

2.1.2 Modelling a dry Earth

Given the significant similarity between the terrestrial and martian atmospheric dynamics, the terrestrial GCM has been adapted to Mars in 1989 by changing the radiative transfer and adding the CO_2 cycle. It was the first model to reproduce a self-working Mars, and pressure variations consistent with the Viking Landers observations of transient weather systems [Hourdin et al., 1993]. Since then, two teams from the Laboratoire de Météorologie Dynamique (LMD), Paris, and the department of Atmospheric, Oceanic and Planetary

[1] $L_s = 0 - 90^o$ northern spring, $L_s = 90 - 180^o$ summer, $L_s = 180 - 270^o$ fall, $L_s = 270 - 360^o$ winter

Physics (AOPP), Oxford, have been developping a full description of the planetary boundary layer, the propagation of gravity waves [Forget et al., 1999a], and more recently a description of the dust cycle [Newman et al., 2002], the water cycle [Montmessin et al., 2004] and its interaction with the regolith [Böttger et al., 2005].

In this study, we focus on the activity of the martian water cycle throughout the Amazonian, without taking into account the dust lifted by the simulated winds or the diffusion into the regolith. But before exploring the past water cycle in chapter 3, we describe from the beginning how clouds are forming in the numerical GCM sky.

2.2 Atmospheric dynamics of a simplified planet

2.2.1 Radiative model

First we consider a simple column of atmosphere which remains, as mentioned above, in hydrostatic equilibrium. The main source of heating of this column is the solar radiation, which is mainly absorbed by the surface and the atmospheric dust. Its cooling mainly results from the IR emissions of the CO_2 15 μm band, the surface, and again the atmospheric dust. For example, figure 2.2 gives the typical IR emission spectra over two portions of the south polar cap, which is approximately the emission of a black body around 200 K (ie the surface), with broad peaks near the CO_2 15 μm band ($\sim 650 cm^{-1}$) and the silicate dust 9 μm band ($\sim 1100 cm^{-1}$), both being warmer than the underlying surface. The effects of water vapor and water ice clouds are relatively small and neglected in the GCM, although the water cycle could have been more active in the past, and the radiative feedback much more intense.

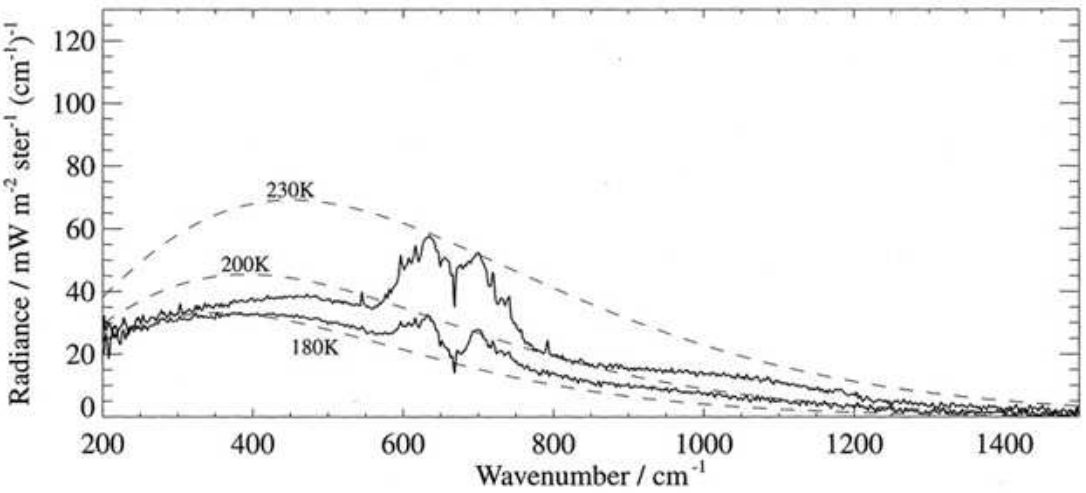

Figure 2.2: Typical IR emission spectra of a cold polar region
Measured by IRIS (IR Interferometer Spectrometer) on board Mariner 9
Figure from [Read and Lewis, 2004]

1) CO_2 15 μm **band :** The CO_2 15 μm band radiative model has been progressively developed with a first spectral Line-By-Line model (LBL), a second Narrow-Band model (NBM) and a final Wide-Band model (WBM) currently used in the GCM [Hourdin, 1992]. The basic idea of a radiative model is to compute the heating or cooling of a given atmospheric layer by the flux divergence. The IR flux is divided into the upward flux $F^{\uparrow}$ and the downward flux $F^{\downarrow}$ which can be written as :

$$F_\nu^{\uparrow}(z) = F_\nu^{\uparrow}(s)\tau_\nu(0,z) + \pi \int_0^z B_\nu(T_{z'}) \frac{\partial \tau_\nu(z',z)}{\partial z'} dz' \tag{2.1}$$

$$F_\nu^{\downarrow}(z) = \pi \int_z^\infty B_\nu(T_{z'}) \frac{\partial \tau_\nu(z,z')}{\partial z'} dz' \tag{2.2}$$

The upward flux at a given altitude z depends on 1) the emission of the surface $F_\nu^{\uparrow}(s)$ modified by the transmissivity of the underlying layers $\tau_\nu(0,z)$ (left-hand side of equation 2.1), and 2) on the emission of the underlying layers themselves, given by the integration of the Planck function $B_\nu(T_{z'})$ balanced by the transmissivity variations $\partial_{z'}\tau_\nu$ (right-hand side of equation). Similarly, the downward flux represents the emission of the overlying layers. Consequently the radiative transfer depends on the layer temperature $T_{z'}$ and the transmissivity. These transmissivities, in the GCM Wide-Band model, are not theoretically calculated but fitted to previous results of the Narrow-Band model.

	Day			**Night**	
	T_s	$F_{SW}^{\downarrow}(s)$	$F_{LW}^{\downarrow}(s)$	T_s	$F_{LW}^{\downarrow}(s)$
1.	272	107	19	187	12
2.	270	100	32	189	18
3.	252	50	120	203	59
4.	166	19	2	148	2
5.	155	12	4	148	4
6.	169	12	5	165	5

Table 2.1: 1D experiments

The upward and downward fluxes are then calculated in two different bands ($14.2\mu m$-$15.7\mu m$ and wings) of the CO_2 15 μm band ($11.5\mu m$-$20\mu m$). When compared to 61 bands for the NBM, this allows a major saving of time for the GCM.

Different experiments are proposed in appendix C.1 to follow the evolution of the radiative model, and the different results are reported in table 2.1. All the simulations begin with an isothermal atmosphere at $T_e = 210K$ and reach these final temperature profiles. The first panel on the upper-left corner is a simulation without atmospheric dust during the equinox and located at the equator, and below is the same simulation at $80^o N$. In this clear atmosphere, these profiles only result from the absorption by CO_2 and the surface thermal IR emissions.

2) Radiative effect of dust : Another major component of the radiative transfer is the atmospheric dust, absorbing at both visible and IR wavelengths. The dust distribution can be predicted by the simulated winds, but in our simulation of the water cycle, we simply assign a dust visible optical depth $\tau_{vis} = k \int \rho dz$ for the whole atmosphere, with k the visible opacity of dust[2]. From this optical depth, a dust mixing ratio[3] q_0 is deduced

[2]Dust optical depth τ is typically equal to $0.2 - 0.4$ under common conditions, $1 - 2.5$ during local dust storms and 5 during global dust storms

[3]Ratio between the mass of a dusty parcel and the mass of a clear parcel

at a reference pressure level of $p_0 = 700$ Pa, the vertical profile being then set to constant under this pressure level, and exponentially decreasing above :

$$q(z) = q_0 \exp\{\nu[1 - p_0/p(z)]\}^{70km/z_{max}} \tag{2.3}$$

The correction factor ν is known to be highly variable with space and time, and is set to 0.007 to fit at best the observations, with a dust top level of 70 km. The top of the dust layer is refined by the coefficient $70km/z_{max}$ to make it thinner at both poles, with a distribution of z_{max} given in figure 2.3.

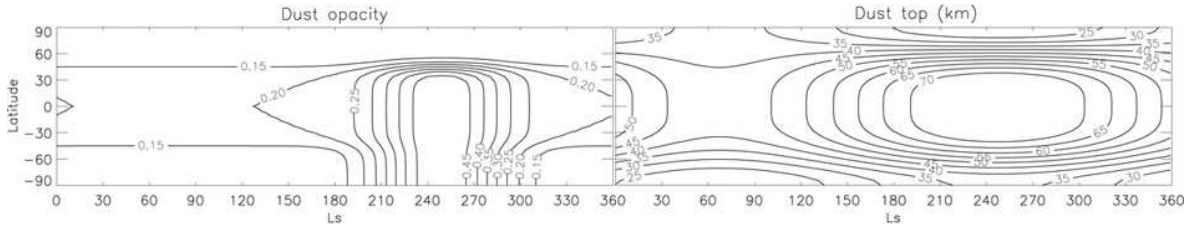

Figure 2.3: Left : Variations of the dust optical depth during the MGS scenario. Right : Top of the dust layer z_{max} in km.

To produce a description of the dust cycle, it is possible to use a varying dust optical depth during the year which is consistent with TES observations (see appendix A.2 for instrument details), as shown in figure 2.3. Having this dust distribution, we can then compute the radiative effect of dust for solar and IR radiations.

For the solar radiations, the difference between upward and downward fluxes at a given level depend on the single-scattering properties of the dust layer governed by the Henyey-Greenstein parameters :

1. The single-scattering albedo $\omega_0 = \frac{Scattering}{Absorption}$,
2. The asymmetry parameter g (mean scattering direction),
3. The extinction efficiency parameter Q_{ext}.

The variations of these parameters with solar wavelengths are given in figure 2.4. The single-scattering albedo ω_0 is minimum around $0.4\mu m$, accounting for the strong absorption of the visible blue wavelengths and the pink color of the sky. However, the asymmetry parameter is maximum and thus the blue wavelengths are scattered mainly forward, giving to the sunset this particular blue halo.

To take into account an abrupt change of these parameters around $0.5\mu m$, they are calculated in two different bands : 0.1-0.5 μm and 0.5-5 μm. Then the transmittances and reflectances of each layers can be deduced, and the radiative transfer computed.

The thermal IR absorption and emission of dust is also computed in the silicate band (5-11.5 μm) and the rest of the IR band (20-200 μm), with a method described in [Forget, 1998]. The ratio between the $9\mu m$ opacity and the visible opacity is essential to predict the energy distribution between the atmosphere and the surface. A value of 2 is assigned in the GCM.

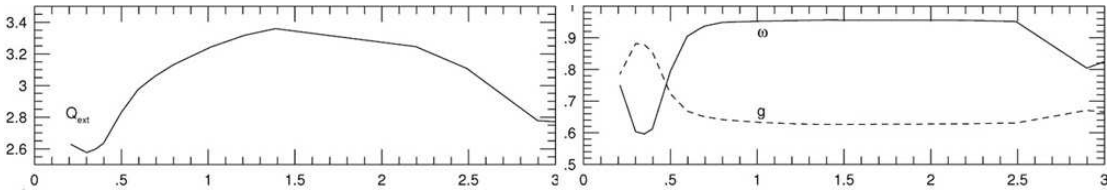

Figure 2.4: Variations of the single-scattering parameters for solar wavelengths
The maximum radiance of the sun is centered around $0.5\mu m$ (from [Forget et al., 1999b])

The solar absorption of dust and the resulting temperature variations are clearly observed in the 1D experiments (see figure C.1). During the day, the progressively increasing dust optical depth of the simulations 2. (0.2) and 3. (2.5) leads to an increase of respectively 30 K and 80 K of the mean altitude atmosphere (15 km) compared to clear conditions. The solar radiation is partly absorbed before reaching the surface, and the resulting heating of the mid-altitudes is obvious in the polar temperature profile of simulation 5., with a 5 km-high heating of $\sim$ 15 K. This strong inversion stabilizes the low atmosphere, reducing the vertical transport processes.

The heating of the high altitudes by the solar radiation during day results in a cooling of the surface (negative greenhouse effect), whereas during the night, the IR emission of dust can preserve a warm surface. These two effects account for the general trends observed in the results of table 2.1. The increase of dust optical depth at the equator (simulations 1. to 3.) and at 80^oN (4. to 5.) creates a decrease of surface temperature and SW surface fluxes during the day, and a reversed trend during the night, i.e. an increase of surface temperature and LW surface fluxes. A final significant effect is the strong IR cooling of the dusty atmosphere during the night, which results in diurnal temperature variations of 40 K at 15 km (simulation 3.), whereas the clear atmosphere remains always at the same temperature (simulation 1.).

Now that the main atmospheric constituents have been considered, our column must be closed by describing the interactions with the surface, in what we call the planetary boundary layer (PBL). Figure 2.5 shows the two main parts of the PBL. **A.** The unstable surface layer which is a few hundred meters thick and where the strong inversion during the night occurs (B. arrow on figure 2.5), and **C.** the convection region where potential temperature is constant and where turbulent mixing occurs. The soil and surface temperatures depend on the balance between incoming fluxes and thermal conduction in the soil [Hourdin et al., 1993]. The temperature of soil is written as a conduction equation $\partial_t T = -C^{-1}\partial_z F_c$ where the conductive flux F_c is given by the thermal gradient $F_c = -\lambda\partial_z T$. The specific heat per unit volume C and the soil conductivity λ are given by the thermal inertia $I = \sqrt{\lambda C}$ deduced from IRTM and TES observations (see map B.3). The turbulent mixing of a field s in the layers **A.** and **C.** can be written

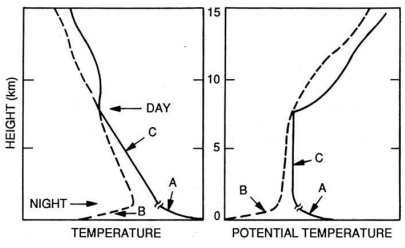

Figure 2.5: Planetary boundary layer
From [Kieffer et al., 1992]

as a diffusion equation $\partial_t s = \rho^{-1}\partial_z(\rho K_z \partial_z s)$, the turbulent mixing coefficient depending on the mixed variable. At the surface, the turbulent flux is calculed via the equation $F_s = \rho C_d U_{5m}(s_{5m} - s_s)$, with s the mixed variable, U_{5m} the wind speed in the first layer and C_d the drag coefficient. This drag coefficient is taken as $C_d = (k/\log(z/z_0))^2$, k being the von Kárman constant $k = 0.4$ and z_0 the roughness length, approximately equal to 1 cm on Mars.

Finally, to prevent subadiabatic vertical temperature gradients [Hourdin et al., 1993], an adiabatic profile is maintened as soon as $\partial_z T < -g/C_p$ (or $\partial_z \theta < 0$) by an energy conserving scheme. The dry adiabatic lapse rate $\Gamma_a = g/C_p$ is equal to $4.5K.km^{-1}$ on Mars (table A.1), and is represented in the temperature profiles of plate C.1. It's worth mentioning the intense convection of simulation 1. compared to simulation 2. (appendix C.1), the turbulent mixing being much more intense in a clear atmosphere, and reaching ~ 8 km for the first simulation.

2.2.2 Setting in motion

1) Equations of motion : Our atmospheric columns, via the radiative transfer described above, are now responding to the solar radiation and the thermal emissions of the surface. Now, we cover an imaginary flat planet of constant albedo and thermal inertia with these columns. The radiative transfer implies a net heating around the equator[4] and a net cooling at the poles, which results in a latitudinal temperature gradient, and thus a horizontally unstable planet. If we simply calculate the scale height $H_p = \frac{RT}{g}$ at the equator and at 80^oN with the first layer temperatures given by the radiative transfer (see figures 2. and 5. of appendix C.1), we obtain respectively $H_{eq} \simeq 12.5$ km and $H_{80N} \simeq 8$ km, ie an expansion of the warm equatorial atmosphere compared to the poles. For a given altitude z, this results in a latitudinal gradient of the hydrostatic pressure $p(z) = p_o \exp -\frac{z}{H_p}$ and a poleward flow, this gradient being more and more intense as we go up in the atmosphere. This mechanism accounts for the upper branch of the Hadley cell. This high-altitude poleward flow increases the surface pressure at both poles, and a reverse pressure gradient and associated equatorward flow are observed at the surface, giving rise to the return branch of the cell. Starting from this qualitative framework, we can now introduce the equations of motion to fully describe the circulation.

The atmospheric motion is described by the Navier-Stokes equation in a rotating frame, which is the origin of the whole GCM dynamics. We can briefly introduce this equation by considering the application of Newton's second law of motion to a single atmospheric particle. First, this particle on which the forces are applied is moving, and its acceleration must be written as the Lagrangian acceleration $d_t \underline{v} = \partial_t \underline{v} + (\underline{v}.\underline{\nabla})\underline{v}$, which can be seen as the intrinsic acceleration of the particle plus the advection of velocity due to its motion. Secondly, three main forces must be considered : 1) the pressure gradient $-\underline{\nabla} p$, 2) the true

[4] ie the difference between the incoming solar radiation and the thermal emission

gravity $\rho\underline{g}^*$, and 3) the viscosity $\eta_d\triangle\underline{v}$. By applying the Newton's law, we end up with a first equation[5] :

$$\rho\frac{d\underline{v}}{dt} = -\underline{\nabla}p + \rho\underline{g}^* + \eta_d\triangle\underline{v} \tag{2.4}$$

Given the fact that we are working in the rotating frame of the planet, the absolute acceleration $d_t\underline{v}$ must be written as the sum of the relative acceleration, the Coriolis force $2\underline{\Omega}\times\underline{v}$ and the centrifugal force $\underline{\Omega}\times(\underline{\Omega}\times\underline{r})$. This last force being a potential force, like gravity, it can be included in a new gravity called the effective gravity $\underline{g}$, and the well-known Navier-Stokes equation is finally :

$$\frac{d\underline{v}}{dt} + 2\underline{\Omega}\times\underline{v} = -\frac{\underline{\nabla}p}{\rho} + \underline{g} + \frac{\eta_d}{\rho}\triangle\underline{v} \tag{2.5}$$

The Navier-Stokes equation 2.5, the continuity equation[6] $\partial_t\rho = -\underline{\nabla}(\rho\underline{v})$ and the equation of state for a perfect gas $p = \rho RT$ form the core of the general circulation model.

2) Discretization of the Navier-Stokes equation : To integrate in space and time the Navier-Stokes equation, we use in this study a three-dimensional grid of $64\times48\times18$ points, the time integration being based on a Matsuno-Leapfrog scheme [Forget et al., 2005]. The horizontal grid is superposed on MOLA topography on figure C.2, and is equivalent to a $5.625^o\times3.75^o$ spatial resolution ($\sim 300\times200$ km). Vertically, the model uses the terrain-following σ coordinate system $\sigma = p/p_s$ with 18 levels :

	1	2	3	4	5	6	7	8	9	10	11	12	13	14	15	16	17	18
km	0.005	0.02	0.04	0.11	0.25	0.5	1	1.8	3.3	5.6	8.9	13.1	18.3	24.2	30.6	37.3	44.2	51.2

Parameterization are added to this dynamical core to describe different phenomema : the radiative transfer and PBL processes described above, the CO_2 condensation and sublimation and the water cycle. The integration of the non-linear Navier-Stokes equation (using around sixty thousands grid points) and its connexion with the sub-grid parameterizations raise many complicated numerical unstabilities of the whole physical system, far beyond what we can describe here. A simplified view of the GCM working is given on figure 2.6.

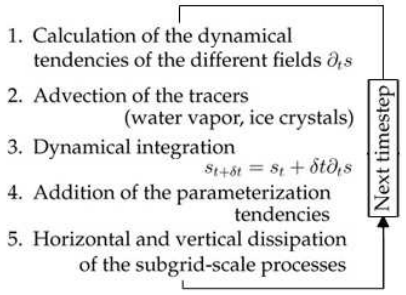

Figure 2.6: One GCM timestep

To study the Navier-Stokes equation and understand what it tells us about the martian circulation, we can first simplify equation 2.5. If we consider that the atmosphere is thin compared to the radius of Mars (thin-layer approximation), the horizontal component of the rotation vector $\underline{\Omega} = \Omega(\cos\theta\underline{j} + \sin\theta\underline{k})$ (where θ is latitude) can be neglected. In the local frame $(\vec{i},\vec{j},\vec{k})$, the rotation vector becomes $2\underline{\Omega} = f\underline{k}$, with f the Coriolis parameter $f = 2\Omega\sin\theta$. The horizontal component of the Navier-Stokes equation can now be written as :

[5]It's worth mentioning that the viscosity $\eta_d\triangle\underline{v}$ and the acceleration form together a diffusion equation, what we call in real life viscosity being theoretically a diffusion of velocity.

[6]In other words, the variation of density is directly related to a convergence of the mass flux.

$$\frac{d\underline{v}_H}{dt} + f\underline{k} \times \underline{v}_H = -\frac{\underline{\nabla}_H p}{\rho} + \underline{F}_r \tag{2.6}$$

The vertical component, by neglecting the friction and the advection of vertical velocity, simply becomes the hydrostatic equilibrium $\partial_z p = -\rho g$. By scaling the advective term of equation 2.6 $d_t \underline{v}_H \equiv U^2/L$ and the Coriolis term $f\underline{k} \times \underline{v}_H \equiv fU$, we can define the Rossby number :

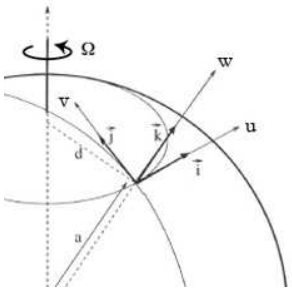

$$Ro \equiv \frac{Advection}{Coriolis} \equiv \frac{U}{fL} \tag{2.7}$$

On Mars, $Ro \sim 0.2$, and 80% of the circulation can be described by neglecting the advection term, in other words by the geostrophic equilibrium :

$$f\underline{k} \times \underline{v}_g = -\frac{\underline{\nabla}_H p}{\rho} \tag{2.8}$$

In pressure coordinates and by using the geopotential Φ defined by $\underline{g} = -\underline{\nabla}\Phi$, we can also write the geostrophic equilibrium as :

$$f\underline{k} \times \underline{v}_g = -\underline{\nabla}_p \Phi \tag{2.9}$$

Since $d\Phi = gdz = -RTd(\ln p)$ via the hydrostatic equilibrium, we can take the vertical derivative of equation 2.9 and reach the thermal wind equation (with its two horizontal components) :

$$f\underline{k} \times \frac{\partial \underline{v}_g}{\partial p} = \frac{R}{p}\underline{\nabla}_p T \;\Big|\; f\frac{\partial v_g}{\partial p} = \frac{R}{p}\frac{\partial T}{\partial x} \;\Big|\; f\frac{\partial u_g}{\partial p} = -\frac{R}{p}\frac{\partial T}{\partial y} \tag{2.10}$$

Coming back to our flat planet and its meridional circulation, we can now understand the zonal circulation and the effect of rotation via the zonal component u_g of the thermal wind equation 2.10. This component represents a balance between the latitudinal gradient of temperature and the vertical shear of the zonal wind u_g via a coefficient $f = 2\Omega \sin\theta$ which depends on the latitude. Thus, we can predict an intense zonal jet where the temperature gradient is significant, its intensity depending on the latitude.

Figure C.3 shows the results of two simulations. A first simulation (upper panel) is performed on a flat planet of constant thermal inertia (247), albedo (0.22), and dust opacity (0.2), and a second simulation (middle panel) represents the present-day Mars with surface properties and the observed dust cycle. The latitudinal temperature (contours) and zonal wind (shaded colors) variations are represented for two seasons : the northern fall ($L_s = 180 - 210$) and the northern winter ($L_s = 270 - 300$, around the perihelion). The lower panel gives a comparison with TES observations [Conrath et al., 2000] for approximately the same seasons.

Before taking into account the surface properties of the real Mars in section 2.3, we can start by analysing the two upper panels. The temperature distribution shows 1) the expansion of the summer air mass and the rising of the Hadley cell, 2) the adiabatic warming

$T/p^{\kappa} = cst$ of the return branch in the winter-hemisphere (elevation of the isotherms) and 3) two reversed latitudinal temperature gradients around 10 km and 40 km. These last temperature gradients are balanced by two vertically increasing jets (thermal wind equation 2.10), obvious during the northern winter with an eastward jet around 60^oN, and a westward jet around the equator. During the northern winter, we can also observe a slight eastward jet at the surface around 30^oS which is described in details in section 2.3.

2.2.3 CO_2 condensation flow

A really particular aspect of the Martian atmosphere is the condensation of its main constituent. As mentioned above, the atmospheric temperature in the high latitudes can be as low as 140 K during the winter, resulting in the seasonal condensation of CO_2 on the surface (see diagram 2.1). The rate of deposition is limited by the release of latent heat which is mostly removed by IR emission to space, following the equilibrium $L\partial_t M = \epsilon\sigma T^4$, where M is the condensation mass of CO_2 per unit area, L the latent heat of sublimation $L \simeq 597kJ.kg^{-1}$ and ϵ the emissivity of CO_2 ice [Read and Lewis, 2004]. These deposits can extend to latitudes as low as 55^oN and 40^oS, and around a third of the atmospheric mass can be deposited on the surface, leading to a major change in surface pressure. At the end of the polar night, this seasonal CO_2-ice deposits sublimate and reload the atmosphere, while the deposition starts to occur on the other pole. The huge deposition of CO_2 on the surface creates a convergent flow during the extension and a divergent flow during the sublimation, adding a vertically-averaged meridional wind component of around $20 - 30cm.s^{-1}$ [Forget et al., 1995]. At the edge of the retreating seasonal CO_2 deposits, the outward flow is deviated by the Coriolis force and forms anticyclonic spirals which can accelerate the zonal wind and favor the creation of local dust storms.

In the GCM, a condensation temperature of CO_2 given by $T_{CO_2} = 149.2 + 6.48 \ln p$ allows the precipitation of CO_2 on the surface [Hourdin et al., 1993], and the corresponding atmospheric pressure variations are calculated, changing the circulation above the CO_2 seasonal deposits.

2.3 Effect of martian topography and surface properties

2.3.1 Modification of the general circulation

The dynamics of our imaginary flat planet being well understood, the next step is to take into account the topography, thermal inertia, albedo and friction of the surface, in other words, the whole martian local meteorology. The topography of Mars (see B.1 and B.2) has a first significant effect on the circulation, due to the assymetry between the northern lowlands and the southern uplands. If we compare the two right-hand slices of figure C.3, without and with topography, this assymetry increases the activity of the Hadley cell

during the northern summer, a difference revealed by the larger adiabatic warming of the return branch (elevation and compaction of the isotherms). Many other topographic variations of the order of an atmospheric height H_p occur on Mars and have tremendous other effects which are described in the following sections.

Thermal inertia and albedo are also driving the PBL temperature, leading to the formation of thermal continents (see figure B.3 and B.4) and associated changes in circulation. Finally, the roughness of the surface, known by MOLA measurements, slows down the surface flow and can also propagate vertical gravity waves, as we will see in the following sections.

In the following sections, we focus on the northern winter season and analyse the flow from the surface to the high levels[7] (~ 20 km) to fully understand the different aspects of martian meteorology. The different figures accompanying this analyse are given in appendix C.4.

2.3.2 Shaping of the surface winds

The main effect of the martian surface is the forcing of the cross equatorial currents by the east-facing slopes of Tharsis ($\sim 45^o$W), Syrtis ($\sim 80^o$E) and Elysium Planitia ($\sim 150^o$E). If we look at the surface and 2 km high winds during the northern winter (figures 1. and 3. of appendix C.4), we can see three main west boundary currents (WBCs), similar to the East African Jet on Earth, which create these hook-like patterns of the winds in the 30^oN-30^oS latitude band. The rising branch of the Hadley cell results in a cross-equatorial flow from winter to summer hemispheres, and this flow is accelerated toward the east as it leaves the equator to conserve its total (fluid and planetary) angular momentum [Joshi et al., 1997]. This deviation was already observed on our flat planet (see the near surface eastward jet around 30^oS on the right-hand panel of figure C.3), but in that case the resulting currents are forming an ideal parabola, the circulation being perfectly axisymmetric. If an east-facing slope prevents the zonal component of flow from developing, most of the angular momentum conservation is applied to the meridional component, resulting in a stronger jet at the equator. It is worth mentioning that the relatively flat uplands of southern Elysium maintain a wide eastward jet all along the dichotomy boundary (from 100^oE-120^oW), whereas the Tharsis and Syrtis WBCs are merging into an intense slope wind in Hellas, the circulation, again, being driven by topography.

2.3.3 Diurnal effects

Figure 2. of appendix C.4 shows the winter circulation and surface temperature at 8h, and major differences can be observed compared to the mean circulation of panels 1. and 3. The diurnal temperature variations on Mars, given the low heat capacity of the

[7]Many of these observations can apply to the southern winter where the general circulation is reversed, but with some major differences due to the latitudinal assymetry of surface properties

atmosphere, the low thermal inertia of the surface and the strong absorption of atmospheric dust, give rise to many atmospheric phenomena, such as the thermal tides or the propagation of diurnal and semi-diurnal Kelvin resonant waves, but also create, on the surface, major slope winds. These winds, created by "progressive density currents" [Forget et al., 1995], are oriented up the slopes if these are warmed (anabatic flow), or down the slopes during night-time cooling (katabatic flow). The interaction of these slope winds with the WBCs described above is evident on panel 2. of figure C.4, where the jets are clearly enhanced in Syrtis and western Hellas, with an intense anabatic flow coming out of eastern Hellas as well.

2.3.4 Stationary planetary waves

The Hadley cell circulation described above provides a good sense of the general circulation, but this broad circulation is unstable and gives rise to ubiquitous stationary[8] planetary waves which considerably change the flow. These waves disturb the temperature, pressure and velocity fields all around the planet, and results from mechanical uplift imposed by the topography, or local heating. The resulting vertical propagation of the waves depends on the Charney-Drazin condition, obtained by perturbation of the streamfunction ψ in the linearized quasigeostrophic potential vorticity equation. Using a sinusoidal topography $h = h_0 \exp[i(k_0 x + l_0 y)]$ as a boundary condition and looking for wave-like solutions of the form $\psi' = A \exp^{i(\underline{k}.\underline{x} - \omega t)}$, we end up with the dispersion relation (see [Read and Lewis, 2004] p:77-78) :

$$m^2 = \frac{N^2}{f^2}[\frac{\beta}{U} - (k_0^2 + l_0^2)] \tag{2.11}$$

N is the buoyancy (or Brunt-Väisäla) frequency, β is the planetary vorticity gradient[9], and U is the mean zonal wind. The vertical propagation $m^2 > 0$ can only occur (Charney-Drazin condition) if $U < \beta/(k_0^2 + l_0^2)$ with $U > 0$. Consequently, propagating planetary waves can only be created by an eastward flow over topographic or thermal gradients, and the propagation would collapse if $U > \beta/(k_0^2 + l_0^2)$. The eastward jet of the northern hemisphere created by the thermal wind equilibrium 2.10 during winter satisfies these conditions and vertical waves can propagate and change the basic-state of the flow. In this simple model, we can notice that the vertical wavelength m of the waves depends on the horizontal wavelengths k_0 and l_0 of the topography, with a dominant effect of the zonal component k_0 due to the mainly zonal flow. Thus, we can predict the main wavenumbers of these planetary waves by looking at the

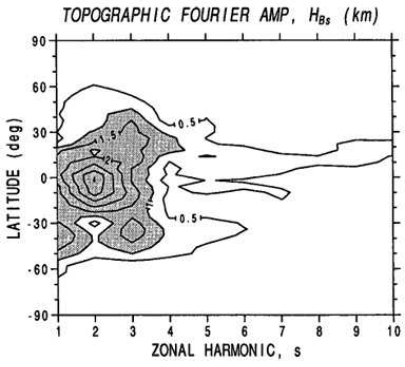

Figure 2.7: Zonal harmonics
From
[Hollingsworth and Barnes, 1996]

[8] Stationary meaning that the waves are fixed in the rotating frame ($v_\phi = 0$).
[9] $f = f_0 + \beta y$ in the β-plane approximation

zonal harmonics of the topography, which are given in figure 2.7. The largest amplitude is observed for the wavenumber 2, which corresponds to the high altitudes of Tharsis and Terra Sabaea, and this signal is clearly observed in the perturbations of the zonal flow by the planetary waves (see the meridional winds on figure 4. of appendix C.4).

A detailed study of the forcing and propagation of these stationary waves is given in [Nayvelt et al., 1997], who developped a linear σ-coordinate model and studied the impact of topography and local heating on the zonally and time averaged circulation of the NASA Ames GCM. The forcing of the stationary waves by the topography is introduced by a vertical perturbation of the wind $w' = \overline{u}.\underline{\nabla}h' + v'\partial_y\overline{h}$, where $\overline{u}$ is the zonal mean horizontal wind vector and $\overline{h}$ and h' are the zonal mean and perturbation components of topography. Consequently the vertical velocity perturbation arises from the local slope $\underline{\nabla}h'$ and the meridional gradient of the zonal mean topography $\partial_y\overline{h}$. The local heating is also given by the thermal forcing term $Q = -\tau_N^{-1}h'\partial_z\overline{T}$, where τ_N is the radiative timescale and $\overline{T}$ the zonal mean temperature. If we consider that most of the time there is a strong temperature inversion near the surface $\partial_z\overline{T} > 0$, then this equation means that a topographic low $h' < 0$ acts as a "heat source", whereas a topographic high $h' > 0$ acts as a "heat sink".

The results of this model are shown on the right-hand panel of figure 2.8, and the effects of an ideal mountain located at 45^oN on an eastward flow are also represented on the left-hand panels. The mechanical forcing is clearly seen around 60^oN (grey boxes), for instance in the topographic lows of Acidalia Planitia and Utopia Planitia, whereas around 30^oN (black boxes), the radiative effect is dominant, with a major signature over Alba Patera. These stationary waves are superimposed on the basic-state flow described in the previous sections (zonal jets, WBCs, diurnal slope winds), and account for many structures observed in the northern mid-latitudes (see figure 3. of appendix C.4), such as the acceleration over Alba Patera and the deflection of the winter jet.

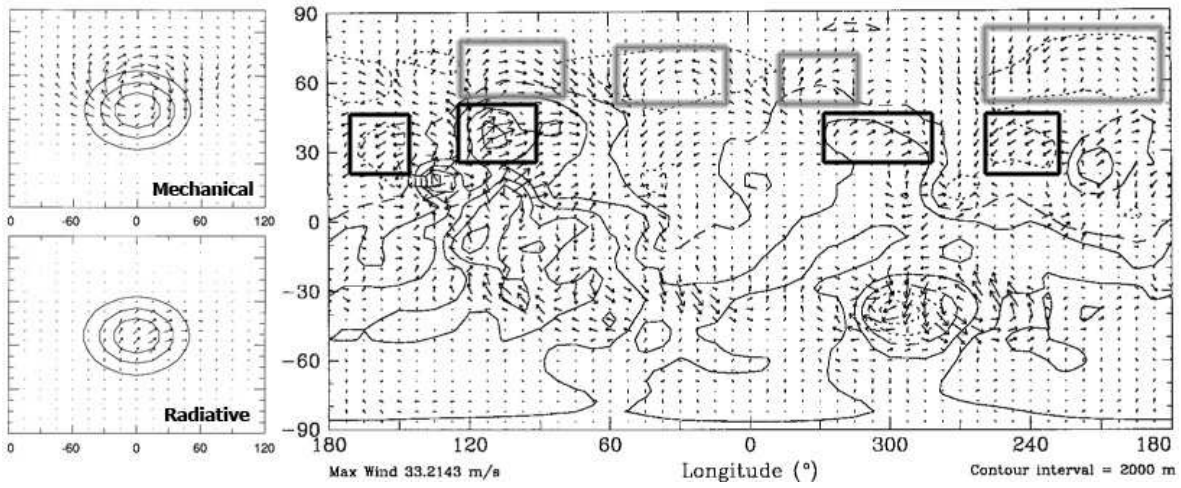

Figure 2.8: Near-surface stationary wave winds created by martian topography
Grey boxes = mechanical forcing, black boxes = radiative forcing. From [Nayvelt et al., 1997]

2.3.5 Creation of baroclinic waves

A last major aspect of the martian circulation is the propagation of eastward baroclinic waves, and the creation of weather systems in the northern mid-latitudes comparable to the cyclonic disturbances found on Earth. The main formation process of these baroclinic waves is the sloping convection, or baroclinic instability, a theory exposed in [Hide and Mason, 1975]. We can summarize this theory by considering the Navier-Stokes equation introduced in section 2.2.2 (equation 2.5), and neglecting the inertial and viscous forces compared to the Coriolis forces, a logical approximation for a rapidly rotating planet. If we take the curl of the resulting equation, given the fact that $\underline{g}$ is irrotational[10], we can write the equilibrium :

$$\underline{\nabla} \times (2\rho\underline{\Omega} \times \underline{v}) \simeq -\underline{g} \times \underline{\nabla}\rho \tag{2.12}$$

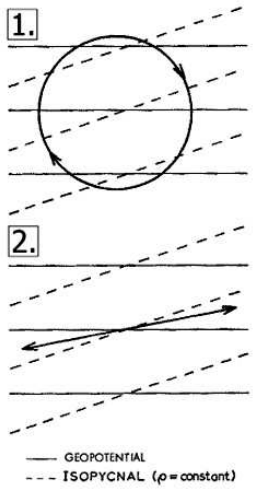

Figure 2.9: Overturning and sloping convection
From [Hide and Mason, 1975]

If the fluid is not rotating $\Omega = 0$, the horizontal vorticity implied by the meridional temperature (and density) gradient (right-hand term of equation 2.12) simply results in a meridional overturning (case 1. on figure 2.9). But if the planet is rotating, the vertical vorticity implied by the Coriolis forces inhibits the meridional overturning, and the other way to convert the excess of potential energy into kinetic energy is to move the parcels along sloping isopycnes (case 2. on figure 2.9). This motion, maintained by the buoyancy forces, can constantly release potential energy, and the resulting poleward-equatorward oscillations can form anticyclonic and cyclonic systems in the vicinity of the eastward jet. These baroclinic waves can be observed during laboratory experiments by imposing a temperature gradient to a rotating fluid, giving rise to the patterns observed on figure 2.10.

Figure 2.10: Rotating fluid with imposed temperature gradient
The rotation rate is increasing toward the right. From [Hide and Mason, 1975]

The travelling weather systems created by these baroclinic instabilities are essential in the terrestrial troposphere to maintain the water vapour budget, and they will also play a key role in the past water cycle of Mars described in chapter 3.

[10]Here we simply apply the formula $\underline{\nabla} \times \underline{\nabla} f = 0$ and $\underline{\nabla} \times (f\underline{A}) = \underline{\nabla} f \times \underline{A} + f\underline{\nabla} \times \underline{A}$.

On Mars, as demonstrated by [Hollingsworth et al., 1996], these baroclinic waves are stabilized and triggered by the topographic storm zones of Acidalia, Arcadia and Utopia planitiae, but also modulated by the stationary waves which are dependent on topography and local heating (see section 2.3.4). Consequently, the paths of eastward travelling weather systems are drawn by the geography of Mars, resulting in a complex and fascinating synoptic meteorology.

To summarize the whole circulation described above, a three-dimensional view of the 2 km winds, provided by the Center for Computation and Visualization (CCV) of Brown University (see [Head et al., 2005]) and the LMD General Circulation Model, is presented on figure C.5. The two eddies of Acidalia and Arcadia Planitia clearly appear in the foreground and near Elysium Mons, and the intense West Boundary Currents of Chryse and Amazonis Planitia are also splendidly represented. Now that the whole dynamics is working, we can take into account its interaction with the water cycle.

2.4 The martian water cycle

As mentioned in section 2.1.1, water vapor in the martian atmosphere is able to condense to form ice crystals (see the cirrus clouds of image D.1), and these crystals can sedimentate and build up on the surface, forming ice deposits. The martian clouds can be clearly observed from the Earth [James et al., 1996] and present particular patterns due to the general circulation which are reproduced by the model with an excellent agreement.

2.4.1 Parameterization of the water cycle in the GCM

The water vapour and ice crystals are considered in the model by adding two tracers transported by the simulated winds, the crystals sizes being predicted by the water-ice cloud microphysics [Montmessin et al., 2004]. When a parcel of the atmosphere is supersaturated, the increasing mass of water-ice M_c is predicted by the equation :

$$\frac{dM_c}{dt} = 4\pi N r_c \frac{S - S_{eq}}{R_c + R_d} \tag{2.13}$$

N is the number of nuclei, which depends on the dust content of the atmosphere via the equation $N(z) = N_0(\tau/\tau_{ref})\exp(-z/H_p)$, r_c is the mean mass radius depending on the growing quantity of ice, S is the saturation ratio (S_{eq} being its equilibrium value, function of crystal microphysical properties [Montmessin et al., 2002]), and $R_c + R_d$ are the respective effects of heat and diffusive resistances. Given the predicted size distribution of ice crystals, the sedimentation process follows the Stokes-Cunningham equation :

$$\omega = \frac{2}{9}\frac{r_c^2 \rho_i g}{\eta_a}(1 + \alpha K_n) \tag{2.14}$$

η_a is the dynamic viscosity of the air, K_n is the Knudsen number and α is a correction coefficient. The crystal fall velocity thus depends on their size distribution, this size

being in part a function of the dust content of the atmosphere. Consequently this model accounts for ice-crystal microphysics and interaction with dust nuclei, and gives excellent results compared to the observations. However, we don't take into account the radiative impact of water vapor and ice clouds, a parameterization which is being developed at the moment.

2.4.2 Precipitation and surface ice deposition

Once the ice is deposited on the surface, the accumulation-sublimation balance depends on a turbulent flux equation :

$$F_w = \rho C_d U_{5m}(q_{vg} - q_{va}) \tag{2.15}$$

U_{5m} is the wind speed in the first layer and C_d the drag coefficient (see paragraph 3 of section 2.2.1). q_{vg} is the saturation mass mixing ratio of water vapor at the ground temperature [Montmessin et al., 2004], and q_{va} is the actual mass mixing ratio of water vapor 5 meters above the surface. In other words, the surface ice sublimates if the first layer of the model is not saturated $q_{va} < q_{vg}$, the process being enhanced by the advection U_{5m} of dry air. On the contrary, the ice can build up if the first layer is constantly satured $q_{va} > q_{vg}$.

2.4.3 Water vapor and cloud distribution

The simulated water cycle is given in figure C.6, and compared to the TES observations. A first high water vapor content, resulting from the sublimation of the north polar cap, is observed during the northern summer, with a total column of water vapor reaching $75\mu m$, a result in perfect agreement with TES [Smith, 2002]. After the summer, the water vapor is transported by the solsticial Hadley cell towards the equator. At the end of northern winter, as the mid-latitude water vapor column is decreasing, seasonal deposits appear around the north polar cap (see figure 2.11), and most of the water vapor lost during the summer comes back to the high latitudes and precipitates on the surface. Baroclinic waves have been proposed to explain this northward "horizontal mixing" of water vapor during the northern winter [Montmessin et al., 2004] and the redeposition of ice in the high-latitudes[11]. Finally, these northern seasonal water-ice deposits

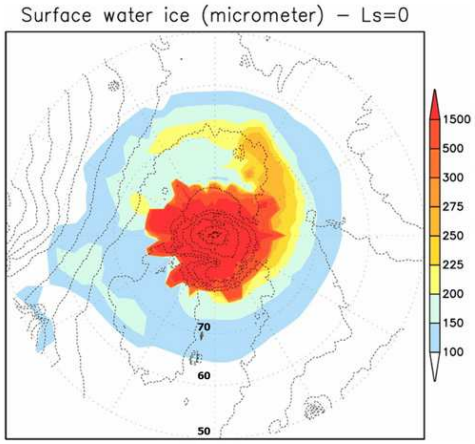

Figure 2.11: Seasonal north polar deposits at the end of winter.

[11] A part of the global water vapor is trapped by the south residual CO_2 cap, resulting in a small net transport towards the south pole.

return to the pole as the north polar cap retreats, and the water cycle is closed.

Regarding the cloud distribution, the two main phenomena are the north polar hoods and the equatorial cloud belt. The north polar hood starts forming at $L_s \simeq 185^o$ south of 60^oN and retreats north of 60^oN after $L_s \simeq 10^o$ [Wang and Ingersoll, 2002]. During all that period, both transient and stationary waves provide a source of water vapor for the northern high latitudes [Montmessin et al., 2004], and the clouds can grow given the low temperatures of these seasons. The impact of stationary waves is clearly seen in the north polar hoods, which show a wavenumber 2 pattern. Depending on the atmospheric circulation, all kinds of clouds can be observed in the MOC images [Wang and Ingersoll, 2002] : condensate and dust hazes in the stable high latitudes, streak clouds related to the jet activity, dust storms and frontal systems resulting from baroclinic wave activity. At the end of the polar hood activity during spring, the streaks disappear and we can only observe smaller hazes and cap edge dust storms [Wang and Ingersoll, 2002].

The equatorial cloud belt results from a totally different mechanism, and appears between 10^oS and 30^oN during aphelion ($L_s \simeq 60 - 100^o$, see [Clancy et al., 1996]). On MOC images, [Wang and Ingersoll, 2002] noticed that these clouds are often observed around the volcanoes, in Valles Marineris and also around Syrtis Major. The equatorial cloud belt is formed during the aphelion season under clear conditions, and is due to the upward advection of humidity in the summer Hadley cell and resulting adiabatic cooling [Montmessin et al., 2004].

Two kinds of clouds are mainly observed by [Wang and Ingersoll, 2002] : fibrous cirrus clouds for $L_s \simeq 44 - 111^o$, and convective cumulus clouds after $L_s \simeq 134^o$. The transition from fibrous to convective clouds results from a major change in wind strengh as the cross-equatorial Hadley circulation vanishes before equinox. The meridional circulation and a three-dimensional view of the cloud distribution for $L_s \simeq 60-90^o$ are shown on figure C.8. The low-level hazes over the north polar cap are clearly seen, and the upwelling branch of the Hadley cell around 30^oN and resulting equator belt are also evident, with preferential condensation over the volcanoes and Valles Marineris, confirmed by the observations. The whole ice column variations over a year, presented in figure C.7, show striking similarities with the TES observations.

Now we can understand the fantastic picture D.1 taken by Opportunity around the equator at $L_s \simeq 74^o$; it simply corresponds to the cirrus clouds of the aphelion cloud belt, observed by [Wang and Ingersoll, 2002] for $L_s \simeq 44 - 111^o$, and also predicted by the model.

CHAPTER 3

Exploring the past water cycle

The Northern Mid-Latitude Glaciation

Given the excellent agreement of the simulated water cycle with the observations, the GCM is considered as a strong basis to explore the past Martian climate. An increasing number of geological features on Mars, described in chapter 1, point to major ice ages on Mars, and broad deposition of ice deposits of different geomorphological nature.

Different climate-related processes have been proposed to account for the high-latitude water-ice-rich mantling deposits [Head et al., 2003b, Mischna et al., 2003, Levrard et al., 2004] and the formation of the tropical mountain glaciers [Forget et al., 2006], but at the moment the geological evidence for a major northern mid-latitude glaciation remains a major issue. In this chapter, we describe the methodology we applied to carry on this climatic exploration, and propose meteorological conditions under which the mid-latitude glaciation can occur. The sensitivity of this process to orbital variations is considered, and a precise comparison with geological observations tests the robustness of this prediction. We finally provide a possible scenario for the mid-latitude glaciation based on predicted orbital variations.

3.1 The climatic excursions

The climate changes on Mars are driven by large spin-axis variations, comparable to terrestrial Milankovitch cycles. To perform a meteorological prediction, we usually need an initial state of the circulation and an atmospheric scenario. On Earth, global warming can be assessed by the present-day state of the atmosphere, and by a CO_2 scenario, based on socio-economic considerations. The approach is the same on Mars, but on larger time scales because of the unchanged topography and absence of oceans. Instead of terrestrial global warming, we can thus predict the martian ice ages by an initial state based on orbital predictions, and a dust scenario, depending on non-anthropogenic, but still complicated considerations.

3.1.1 A climatic prediction on geological timescales

The spin-axis variations of Mars are strongly chaotic, but a precise solution has been calculated by [Laskar et al., 2004] for the last 10 Myr. The resulting obliquity is given on figure 3.1. Two main obliquity periods are observed [Laskar et al., 2004] : a first low mean obliquity regime of 25 ± 10^o, and a second high mean obliquity regime of 35 ± 10^o, both having a periodicity around 120 kyr. The eccentricity is also varying between approximately 0 and 0.12, with a dominant 2.4 Myr modulating period and smaller 95 kyr oscillations. Finally, the argument of perihelion precesses with a period of 50 kyr.

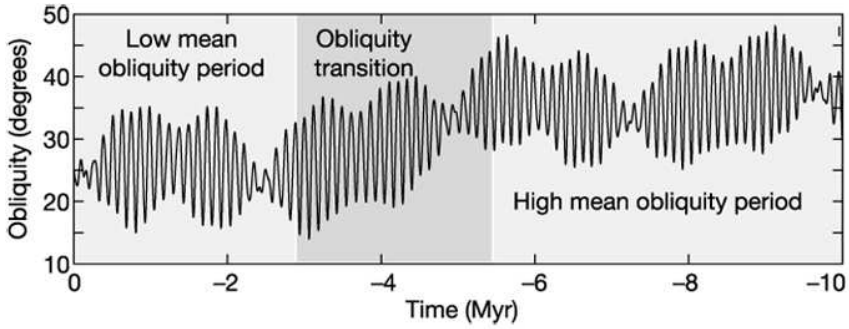

Figure 3.1: Obliquity variations over the last 10 Myr
From [Laskar et al., 2004]

Considering these orbital predictions, we have almost all the initial states required to predict 10 Myr of martian climate. But the dust cycle being poorly constrained, we still have this major unknown component in the system. However, a parameterization of the dust lifting and transport by the circulation has been developed by [Newman et al., 2002] and studied under different orbital conditions [Newman et al., 2005], and will help us to better constrain the system in the following sections.

3.1.2 The migration of water-ice reservoirs

A last parameter of the initial state is the location of the water source(s). The present-day water cycle is fed by the north polar cap, but the obliquity variations and resulting changes in latitudinal insolation distribution result in the migration of the water-ice reservoirs, confirmed by the geological observations (see chapter 1).

The sublimation of the north polar cap and resulting creation of different water-ice reservoirs has been studied by [Levrard et al., 2004], who came to the conclusion that the north polar cap becomes unstable for obliquities higher than $\sim 35^o$, resulting in a column water abundance of the atmosphere of $\sim 3000 \mu m$ during the northern summer [Forget et al., 2006], compared to a present-day observed column of $\sim 75 \mu m$ (see section 2.4). This north-polar water-ice can be redeposited on the western flanks of Tharsis Montes and Olympus Mons by adiabatic cooling of strong westerly winds with an accumulation rate up to $60\ mm\ yr^{-1}$ at 45^o obliquity [Forget et al., 2006]. If we consider the duration of high obliquity excursions [Laskar et al., 2004], such an accumulation could create $\sim 3km$ thick glaciers [Levrard et al., 2004] on the volcanoes, the locations

and thickness of these deposits being in excellent agreement with geological observations [Shean et al., 2005] (see figure 3.2).

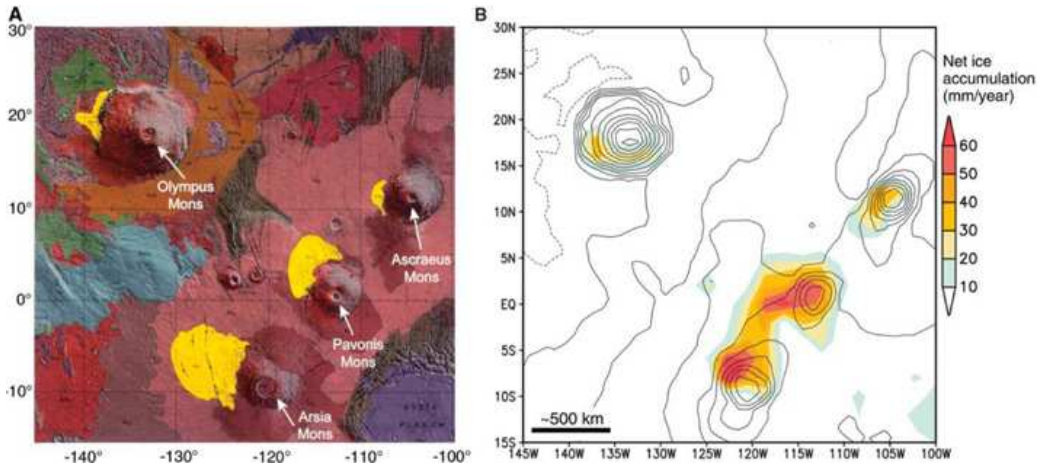

Figure 3.2: Geological map of the Tharsis region (the yellow units correspond to the fan-shaped deposits) and surface ice accumulation predicted by the GCM
The dust opacity is set to 0.2 and the eccentricity is null.
From [Head et al., 2003a] and [Forget et al., 2006].

The presence of these water-ice reservoirs at the equator under different orbital conditions has a significant impact on the water cycle. [Levrard et al., 2004] also studied the distribution of surface ice deposits resulting from a water source located on Tharsis Montes, and showed that an accumulation of ice of several millimeters per year could occur above 60^oN and under 60^oS under low obliquity ($15 - 25^o$, see figure 3.3). Given the orbital predictions, these deposits could build up during 60 kyr and form more than 10 meter thick deposits, consistent with the high latitude mantles observed by [Head et al., 2003b].

However, this equatorial source, formed under high obliquity, could not persist during the transition to the mean low obliquity period, and would be totally sublimated around 3 Myr ago [Levrard et al., 2004]. This assessment would suggest that the high-latitudes mantles are more than 3 Myr old. Thus, we still have to know whether these deposits could form under the mean high obliquity regime or not, and further discussions can be found in section 4.2.

For all these studies, the mid-latitude deposits are not observed. However, as mentioned by [Forget et al., 2006], a lot of other climatic configurations could be considered to account for the mid-latitude viscous flow features, and this is the main purpose of the present study.

3.1.3 A highly variable system

All the studies mentioned above show the multiple climates we can reach by changing the obliquity and the water sources. However, we underlined that five main parameters are controlling the martian climate : 1) the obliquity ϵ, 2) the eccentricity e, 3) the argument

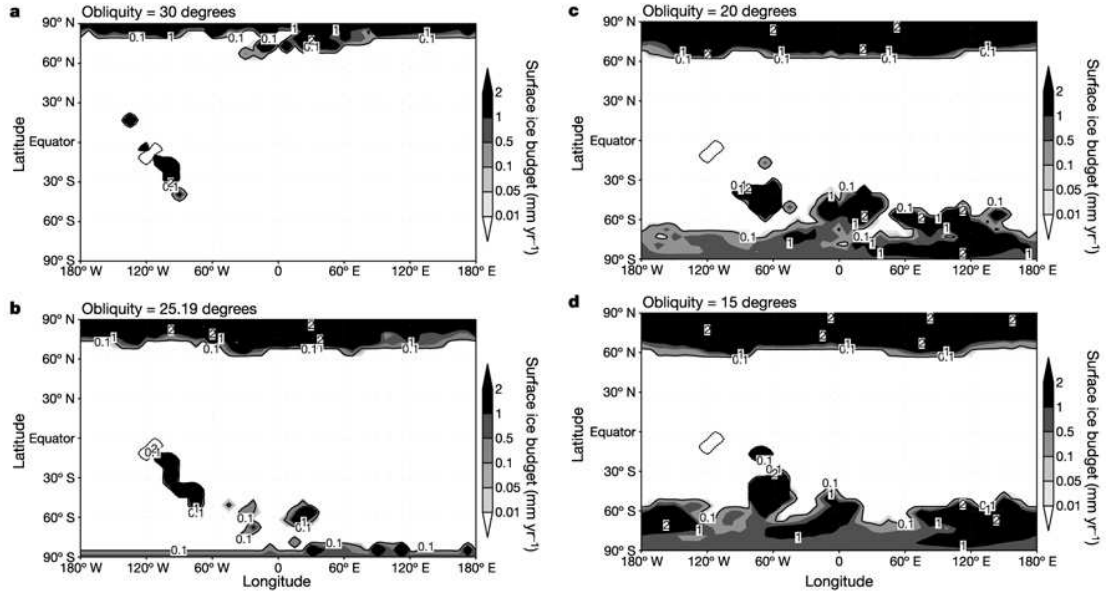

Figure 3.3: Surface ice accumulation predicted by the GCM with an equatorial source of water

The dust opacity is set to 0.2 and the eccentricity is null. From [Levrard et al., 2004]

of perihelion L_p, 4) the dust content, or in the GCM, the dust opacity τ, and 5) the location of ice reservoirs. Consequently, exploring the past climates consists of exploring this five parameter space, and the previous studies can be seen as the exploration of the two dimensional (obliquity-water source) plane. Here we carry on exploring the climate by varying the other parameters, and given the large number of possibilities, we define the following methodology.

3.1.4 Technical approach

The exploration of this five-parameter space requires a significant amount of simulations, which are made possible by the use of the LMD calculation facilities in Paris and the CCV cluster of Brown University. The usual methodology is to run a set of parallel simulations on the LMD and Brown computers, each simulation representing three years of a given paleoclimate. Most of the time after three martian years of simulation (around 5 days of calculation), the model is still in the process of reaching a different equilibrium. First we analyse this climatic tendency in terms of general circulation (surface pressure and atmospheric temperature deviations, seasonal and diurnal wind variations), water cycle (water vapor content, cloud distribution and precipitation) and glaciation (surface water-ice accumulation). Then, if the simulation is leaning towards a good agreement with geological observations, we extend the simulation to attain a physical steady state of the atmosphere. A detailed analysis of this stable climate is finally performed with a spatial resolution of $\sim 300 \times 200km$ (see figure C.2) and a temporal resolution of 2 hours.

Around 30 simulations have been thus performed by combinations of four obliquities

($\epsilon = 15 - 25 - 35 - 45^o$), two eccentricities ($e = 0 - 0.1$), two arguments of perihelion ($L_p = 90 - 270^o$), three optical depths $\tau = 0.2 - 1 - 2.5$ and three water sources (North polar cap, South polar cap or Tropical mountain glaciers), the choice of the parameters depending on a constant comparison with the geological observations in order to reach the best simulation. In the following section, we describe the first simulation which was able to reproduce the mid-latitude glaciation, before studying its sensitivity to the different parameters.

3.2 A proposed meteorological mechanism for mid-latitude glaciations

3.2.1 Distribution of water vapor

The simulation starts with an equatorial source of water located on the western flanks of the great volcanoes, where the tropical mountains glaciers are observed. The first simulation which shows a significant accumulation of ice in the northern mid-latitudes is a low obliquity simulation $\epsilon = 15^o$, with an eccentricity $e = 0.1$, an argument of perihelion of $L_p = 270^o$ and a dusty atmosphere $\tau = 2.5$. This simulation allowed us to understand the conditions under which a mid-latitude glaciation can occur, but we will see during the sensitivity studies that we can find an even better configuration.

If we look at the new water cycle created by these conditions (see figure C.9), a striking pattern is the high sublimation of the source during the perihelion. The total column of water, i.e. the water vapor plus the ice crystals (upper panel), can reach $1400 \mu m$ during the northern winter, which is approximately two orders of magnitude higher than today, and two times less than the amount released by the sublimation of the northern polar cap under a 45^o obliquity [Forget et al., 2006]. Here, given the low obliquity, the insolation stays centered at the equator, imposing the same pattern to the atmospheric water content. During the northern winter, clouds (lower panel) are mainly located around 30^oS and in the northern mid-latitudes, between $30 - 60^o$N.

3.2.2 Topographic control

First we analyse the origin of these clouds and their spatial distribution. The first panel of figure C.10 represents the zonally averaged distribution of ice crystals (mass mixing ratio) and temperature for an obliquity of 15. The high insolation around 30^oS, underlined by the 230 K temperature contour, increases the sublimation of the water-ice reservoir and a large amount of water vapor is released. The clouds centered at the equator, around 25 km above the surface, result from the condensation of this water vapor by adiabatic cooling in the upwelling branch of the Hadley cell. These ice crystals are transported by the strong westerly flow in Solis Planum (see panel 1. of figure C.11), where we often observe ice deposition. Regarding the northern mid-latitudes, strong condensation of ice crystals are found in lower altitudes, as we cross the pole-equator temperature gradient. A poleward

flux of water vapor leaving the equator can be observed, and the cooling of this warm and humid equatorial air across the temperature gradient creates this large "mid-latitude belt".

The equator-pole mixing is mainly controlled by the stationary planetary waves. The activity of these planetary waves and the cloud cover are given in the first panel of figure C.11. The wavenumber 2 signature is clearly seen in the meridional component of the 13 km circulation, resulting in the broad scale distribution of the mid-latitude clouds. Interestingly, the polar hoods observed under the present-day climate are strongly related to the "horizontal mixing" of the planetary waves [Montmessin et al., 2004], and this signature of the wavenumber 2 is evident on the MOC images [Wang and Ingersoll, 2002]. The mechanism observed in our simulation is similar, but the water cycle is totally changed by the equatorial water source, and the high dust content of the atmosphere.

3.2.3 Impact of dust on precipitation

The necessary condition to observe the mid-latitude glaciation is a high dust content of the atmosphere. None of our simulations performed with a dust opacity lower than $\tau = 1$ were able to reproduce satisfactory ice deposits in the mid-latitudes, and we underline in this section the main effects of a dusty atmosphere.

Surprisingly, what we call the Martian ice ages clearly appear in this study to be the consequence of a global warming. If we compare the meridional temperature variations for the present-day dust opacity (dashed line in figure 3.4) and a high dust opacity simulation (solid line) during the northern winter, with the same orbital parameters, we observe a quasi-general cooling of 10K at the surface (upper panel), and a warming of the mid-latitude of around 30K (lower panel). This general trend has three major consequences. First the higher atmospheric temperature in the mid-latitudes and resulting high saturation vapor pressure[1] increases the water vapor content of these latitudes. Secondly, the intensified latitudinal temperature gradient between 30^oN and 60^oN increases the zonal wind (see thermal wind equation 2.10), and thus favors the propagation of stationary waves (section 2.3.4) and baroclinic instabilities (see equation 2.12), both playing a major role in the water cycle. Finally, the mean cooling of the surface is expected to stabilize the surface ice deposits by decreasing the surface saturation vapor pressure and increasing the downward turbulent flux (q_{vg} in equation 2.15).

The first panel of figure C.10 underlines both the increased Hadley circulation (see the strong adiabatic warming of the return branch) and the horizontal mixing in the mid-latitudes, both acting to enhance the northern mid-latitude cloud formation.

This global and seasonal trend hides another local and diurnal effect of major interest. To analyse the climate of the mid-latitudes, we use a meteorological "station" in Deuteronilus Mensae (DM, 40^oN-30^oE, see map B.2), which is one of the most important examples of glacial activity along the dichotomy boundary. The left-hand panel of figure C.12 show the temperature profiles over Deuteronilus Mensae for two simulations : the classical simulation[2] studied in this section, and the same simulation for a dust opacity

[1] Given by $p_{sat} = 6.11 \exp[22.5(1 - \frac{273.16}{T})]$ [Richardson and Wilson, 2002]

[2] $\epsilon = 15$, $e = 0.1$, $L_p = 270^o$, $\tau = 2.5$, water source : equatorial

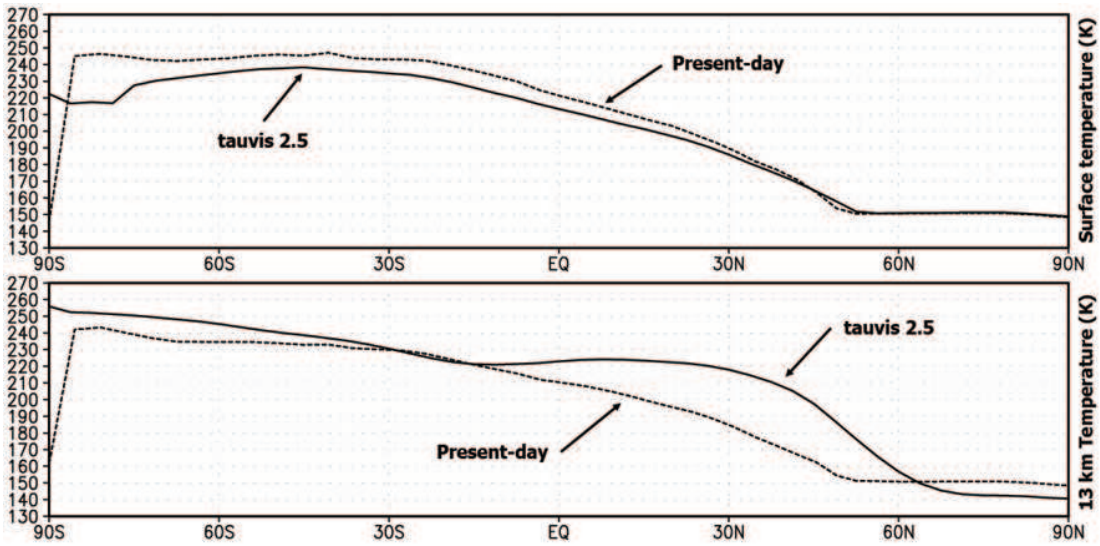

Figure 3.4: Surface and 13 km temperatures for the present-day climate (dashed) and a warm scenario - $L_s = 270 - 300^o$

The orbital parameters are the same for both simulations (present-day).
Present-day : $\tau = 0.2 - 0.8$ (MGS scenario) - Warm scenario : $\tau = 2.5$.

$\tau = 1$. The dashed line shows the temperature during the day, and the solid line during the night. Two major effects are clearly visible : the atmospheric warming during the day, and the dust cooling during the night (see grey zone in figure C.12), respectively increasing the water vapor content of the atmosphere during the day (arrow of the middle panel), and precipitation during the night (right-hand panel).

Therefore, the strong response of this opaque atmosphere to the insolation tends to favor the broad-scale formation of a mid-latitude belt, the local precipitation of ice, and the preservation of the surface deposits, all resulting in an relatively warm, but glacial climate.

3.2.4 Baroclinic wave propagation

To continue our analysis, we now focus on the variation of the surface ice deposits in our station of Deuteronilus Mensae, presented on figure C.13. The left-hand panel shows the thickness of ice deposits during the sixth year of simulation. At the beginning of the year, around 4 cm of ice have already been accumulated on the surface. The evolution of the surface-ice thickness shows two main regimes of accumulation : the diurnal precipitation of the northern summer (sols 1-430)[3], and a strong accumulation during the northern winter (sols 430-650)[4].

The summer accumulation appears to be highly variable, because it results from a delicate equilibrium between the nocturnal precipitation and the daily sublimation. Thus,

[3]A sol is a martian solar day. One martian year is 669 sol-day long.
[4]The last 19 days are not represented.

the derivative function of the surface-ice thickness during the summer (see right-hand panel 1.) shows strong oscillations between negative values (sublimation) and positive values (precipitation). This highly variable accumulation disappears in very clearly glacial areas, such as Nilosyrtis Mensae (35^oN-65^oE, see map B.2), and can be totally reversed and show evident sublimation where major deposits are observed. We can thus rule out this mechanism to explain the major mid-latitude glaciation.

On the contrary, the northern winter shows a 5 mm accumulation resulting from strong and constant accumulation during all the season, with a constantly positive derivative function. If we closely look at the recorded accumulations during 25 days of simulation (right-hand panel 2.), two conclusions can be drawn. First, there is a constant "baseline" accumulation of $2\mu m$, which reveals constant precipitation during the northern winter due to the falling of ice crystals from the mid-latitude belt. Therefore, we are observing a paleoclimate under which it is constantly snowing in the northern mid-latitudes. Then, we observe an obvious periodicity of the signal, of around 5 days, and a smaller one of around 3 days, with peak accumulations of around $15\mu m$, and a particularly marked accumulation around sol 534. The martian meteorological station Viking Lander 2 (50^oN-135^oE), observed this kind of bimodal oscillations of around 2-4 days and 5-7 days [Collins et al., 1996], which are clearly related to transient weather systems and baroclinic waves.

Consequently, we should be able to see on meteorological maps the propagation of weather systems and the observed precipitation around sol 534. We show in figure C.14 four main components of the mechanism : 1) the high and low pressure systems (blue contours, the three dashed contours around 45^oN-0^oE are -40, -50 and -60 Pa perturbations[5] of the 20 days averaged surface pressure around sol 534), 2) the meriodional component of the 2 km winds (shaded colors, $m.s^{-1}$), 3) the water vapor mass mixing ratio at 2 km (the black solid contour shows regions where the water vapor mixing ratio is greater than 0.006), and 4) the sum of the water vapor and ice mixing ratios at 2 km (the black dashed contour is drawn for the same mixing ratio of 0.006). Consequently, a large difference between the solid and dashed lines can be considered as a high precipitation event, the merging of both lines meaning an absence of condensation.

The black arrows indicate the locations of Deuteronilus Mensae (DM) and Phlegra Montes (PM), two regions where typical glacial landforms are observed. The large accumulation of sol 534 occurs on the first panel, where the low pressure system around 45^oN-0^oE is clearly seen. The passing of this low pressure system over DM creates a $10m.s{-}1$ acceleration of the meridional flow, resulting in the advection of warm and humid equatorial air over this region. The corresponding warm front and condensation of ice crystals are underlined by the poleward motion of the black dashed line. The fascinating aspect of this eastward baroclinic wave is its stabilization by the topographic high of the dichotomy boundary, accounting for the particularly large accumulation observed in Deuteronilus (DM) or Nilosyrtis Mensae. In panel 2., the low pressure system and associated λ-shaped warm front are evident, and the precipitation extends to the Utopia Planitia lowlands where the wave activity is progressively decreased (panel 3.) by the mechanical stationary waves of northern Elysium (see panel 1. in figure C.11, and figure 2.8). Finally, this

[5]Surface pressure is given by a running average with a 1 day window

weather system is reactivated in Phlegra Montes, and reaches the bulge of Alba Patera. Its activity is still intense over the North flanks of Alba Patera and Mareotis Fossae (50^oN-75^oW), before the low pressure system vanishes in Acidalia Planitia. It is worth noting that all along this eastward propagation, precipitation is modulated by the diurnal cycle (see the longitudinal variations of the black solid line), and is even more intense when the low pressure system is passing during the night (as illustrated in panel 4. of figure C.14).

The mechanism is summarized by two Hovmoller plots and the daily averaged surface pressure in Deuteronilus Mensae (see figure C.15). The upper panel represents the variations of both water and ice mixing ratios over time, and the middle panel the variations of temperature. The lower panel shows the surface pressure variations, and indicates four low pressures systems, consistent with the bimodal oscillations observed by Viking Lander 2. Two main warm fronts occur around sols 529 and 534, and temperature increases by around 10K (middle panel). The incoming equatorial humid air condensates and the precipitation occurs (upper panel), and the precipitation trail is clearly seen during sol 534. The atmosphere is strongly controlled by the diurnal cycle, with an evident signature in both temperature and water content fields.

It is interesting to note that the baroclinic wave activity is already observed in the present-day water cycle [Montmessin et al., 2004], and is also emphasized in MOC images by fronts and spiral clouds [Wang and Ingersoll, 2002]. Consequently, what we observe in this 15^o obliquity simulation, and also in the following $25-35^o$ simulations, is a mechanism which occurs today on Mars, but with much more water vapor and significant modifications of the general circulation due to the high dust opacity and the different water source. We may wonder whether this mid-latitude glaciation occurs with the same opacity and a North or South polar source of water. Other simulations suggest that it is not the case, because both polar caps are too stable under the favorable obliquities to release a sufficient amount of water vapor. Therefore, the equatorial source of water is maintained in the following sensivity studies, but obliquity, eccentricity and dust opacities are all changed to better constrain the mechanism, and find possible geological periods of activity.

3.3 Sensitivity to orbital variations

A first set of four simulation is analyzed and the resulting surface ice accumulations are given in figure C.16. The surface ice accumulation for the simulation described in the previous section is shown on panel 1. The obliquity is increased from panel 1. to panel 4. with the following values of obliquity : 15, 25, 35 and 45^o. All the other parameters are kept constant : $e = 0.1$, $L_p = 270^o$, $\tau = 2.5$ and a water source is created on the great volcanoes. The same orbital parameters are employed for the plates C.11 and C.10.

Two others simulations are performed to study the impact of dust opacity and eccentricity. The first one is the same simulation as the one described in the previous section ($\epsilon = 15$, $e = 0.1$, $L_p = 270^o$, water source : equatorial) but with a dust opacity $\tau = 1$, and the second one is a 35^o obliquity simulation with $\tau = 2.5$, and an eccentricity $e = 0$.

Table 3.1 summarizes the main results of these simulations, but the high obliquity simulation is not represented. The surface ice accumulation rates (SIAR) for the main glacial

regions of the dichotomy boundary are given in $mm.yr^{-1}$, with the sublimation rate of the tropical mountain glaciers (SSR), the water and ice maximum column over the source (ES) in μm, and the maximum value of the ice column found in the mid-latitude belt (MLB), in μm.

Configuration	SSR	SIAR $mm.yr^{-1}$				ES	MLB
	$cm.yr^{-1}$	DM	NS	PM	MF	μm	μm
$\epsilon_{15}\tau_1$	39	1	10.1	0	7.3	1800	100
1) $\epsilon_{15}\tau_{2.5}$	92	9.3	15	7	15.1	2100	400
2) $\epsilon_{25}\tau_{2.5}$	52	15.3	17.3	13	12.1	2000	800
3) $\epsilon_{35}\tau_{2.5}$	38	9.6	18.2	8.1	7.5	1800	800
$\epsilon_{35e0}\tau_{2.5}$	29	1.2	1.5	0.6	0.9	700	330

Table 3.1: Results of the sensitivity tests
Obliquity and dust opacity are given in the first column. The eccentricity is $e = 0.1$ and the argument of perihelion is $L_p = 270^o$, except for the last simulation ($e = 0$).
SSR : Source Sublimation Rate (tropical mountain glaciers) - $cm.yr^{-1}$
SIAR : Surface Ice Accumulation Rate - $mm.yr^{-1}$
ES : Equatorial Source - Maximum water + ice column over the sources - μm
MLB : Mid-Latitude Belt - Maximum ice column over Utopia Planitia - μm
DM : Deuteronilus Mensae 40^oN-30^oE - NS : NiloSyrtis Mensae 35^oN-65^oE
PM : Phlegra Montes 40^oN-165^oE - MF : Mareotis Fossae 50^oN-75^oW

We use these simulations to define the range of obliquity, eccentricity and dust opacity under which the mid-latitude glaciation is likely to occur.

3.3.1 Obliquity range : Effect on baroclinic wave activity

The mid-latitude glaciation occurs for an obliquity between 15^o and 35^o. We can see in figure C.16 that the mid-latitude glaciation totally disappears when we reach 45^o of obliquity. Many reasons account for this sudden change. First, the wavenumber 2 planetary waves favor the formation of the mid-latitude cloud belt for an obliquity smaller than 45^o (see panel 1., 2. and 3. in figure C.11). When we reach this last obliquity, the planetary waves undergo major changes. For example, the strong bimodal structure over Deuteronilus Mensae and Utopia Patera is moved equatorward, and does not enhance the cloud belt formation any more. Another major effect is the sublimation of the source, which is weaker with a high obliquity, the insolation being more distributed in latitude (see the relatively low ice content of the high obliquity simulation in panel 4. of figures C.11 and C.10, and also the decreasing source sublimation and water column in Table 3.1 as we increase the obliquity). Finally, the low-level jets are dominating the baroclinic waves propagation for a high obliquity and the equator-pole temperature gradient is decreased by the Hadley circulation, a phenomena also observed by [Haberle et al., 2003] and [Newman et al., 2005]. Consequently, these last main factors of the mid-latitude glaciation are also suppressed.

The 15^o obliquity simulation is questionable, because the atmospheric dust opacity during period of low obliquity is not expected to be so high ($\tau = 2.5$), even though dust

lifting is favored by the baroclinic activity [Haberle et al., 2003]. However, a dust opacity of 2.5 is consistent with the present-day dust storms observed in Amazonis Planitia and Chryse Planitia [Cantor et al., 1999], and we can conceive a strong interaction between these dust storms and the mid-latitude precipitation we observe in our paleoclimatic simulations. Consequently a dust opacity of 2.5 with the present-day orbital parameters and an equatorial source (simulation 2., see table 3.1 and figure C.16) is a reasonable scenario. Finally, for an even higher obliquity of 35^o, our simulations show major activity of the baroclinic waves which could result in higher dust lifting, and large dust opacities under these conditions have already been simulated by [Haberle et al., 2003] and [Newman et al., 2005]. Thus simulation 3. is also likely to occur in the past.

Therefore, among the three obliquities under which the mid-latitude glaciation occurs (see figure C.16), we rule out the low obliquity simulation and define a probable obliquity range of glacial activity $\epsilon = 25 - 35^o$.

3.3.2 Changing the perihelion : An interglacial period

The mid-latitude glaciation is also very sensitive to a change of eccentricity, and a decreasing eccentricity results in a retreat, or suppression of the deposits. The argument of perihelion is also essential, and a reversed argument $L_p = 90^o$ also results in a retreat of the mid-latitude deposits. The last simulation of Table 3.1 shows the effect of a null eccentricity on the 35^o obliquity simulation. The sublimation of the source is strongly subdued, the maximum ice column of the mid-latitude belt is divided by two, and the accumulation rates simply collapse. These results are not surprising, given the fact that a high eccentricity $e = 0.1$ and a perihelion during the southern summer was in fact the best way to increase the meridional circulation [Haberle et al., 2003], the northern jet and the propagation of the baroclinic waves. Thus we consider that a high eccentricity $e = 0.06 - 0.1$ is necessary for a large extension of the mid-latitude glaciation, and that the periods of low eccentricity can be seen as interglacial periods, where a retreat of the deposits is likely to occur.

3.3.3 The dust cycle : Main actor of the glaciation

As mentioned above, a dust opacity of $\tau = 1 - 2.5$ is necessary to develop the mid-latitude glaciation, and the sensitivity of the system to the dust content is significant. For example, if we perform the 15^o obliquity simulation with a dust opacity $\tau = 1$ instead of $\tau = 2.5$ (see the two first lines of Table 3.1), the sublimation rate of the source is divided by two and the accumulation in Deuteronilus Mensae and Phlegra Montes vanishes. However, it is worth mentioning that the accumulation in Nilosyrtis is still relatively high, this accumulation being strongly controlled by the wavenumber 2 stationary planetary wave in Utopia Planitia (see panel 1. and 2. of figure C.11).

This necessary high dust content of the atmosphere is a fascinating aspect of the mid-latitude glaciation. The dust lifting under $25 - 35^o$ obliquities is strongly controlled by the baroclinic waves [Newman et al., 2005], and for example, an interaction between our simulated water cycle and a dust storm in Chryse Planitia, as simulated by [Newman et al., 2002],

would probably result in the same kind of precipitation we observe in our simulations, with major improvements, compared to the constant dust opacity used in this study. The coupling of the dust lifting and the water cycle, and also the radiative feedback of the clouds, which could be significant with such cloud opacities, are both expected to greatly improve these results in the future.

The meteorological mechanism being well constrained, we now compare these results with the geological observations and propose a possible scenario for the northern mid-latitude glaciation.

CHAPTER 4

Comparison with the mid-latitude geomorphology

Toward a climatic scenario of the Martian ice ages

4.1 The geological observations

Thirty years ago, Steven Squyres mapped with the Viking images the ice-assisted lobate debris aprons and impact craters with concentric fill in the northern mid-latitudes, and noticed an "absence of deposits in the regions outside the two latitudinal bands, (which) can readily be attributed to a climatic influence" [Squyres, 1979]. This map is superposed on the predictions by the General Circulation Model in figure B.5, and shows an excellent agreement with the predicted ice accumulation regions. In the light of the new data and studies undertaken by the Brown planetary group, we analyze in the following sections the geomorphology of selected regions, indicated on the map.

4.1.1 Phlegra Montes (1)

North-west of Arcadia Planitia, debris-covered glacial deposits can be found along the scarp of Phlegra Montes and around individual massifs. In the same region, a crater shows viscous flow features with arcuate ridges (see figure D.2). Cyclones are particularly intense in Phlegra Montes, as observed in panel 4. figure C.14.

4.1.2 Alba Patera region (2,3,4)

Region 2 : Down the northern flank of Alba Patera, [Ivanov and Head, 2006] studied young ice-like deposits, probably Amazonian in age, and also documented valley networks, probably formed by geothermal heating and melting of snowpacks.

Region 3 : This region is interesting because under high obliquity (see panel 3. of figure C.16), a large accumulation occurs over Ceraunius Tholus, where [Fassett and Head, 2006] observe radial channels running off a 25 km diameter caldera. Figure D.3 is a perspective view of the largest channel (~ 2 km wide), which flows down the flank of the volcano into an oblique crater (Rahe Crater) and forms a delta-like deposit. This flow probably results from melting of summit snowpack by volcanic intrusive geothermal heating, after accumulation and preservation in the caldera [Fassett and Head, 2006].

Region 4 : Lobate debris aprons (LDA) and lineated valley fill (LVF) occur in many places in the graben and mountains of Tempe Terra [Head and Marchant, 2006].

4.1.3 Deuteronilus-Protonilus-Nilosyrtis Mensae (5)

This region is probably the best example of glaciation, and is briefly described in chapter 1 [Head et al., 2006b, Head et al., 2006a]. Figure D.4 shows an example of large debris aprons at the base of the dichotomy boundary, with many individual lobes emerging from different alcoves and merging together. Figure D.5 also shows many individual lobes merging together to form lineated valley fill, and flowing down valley to the upper-right corner.

The hypothesis of a regional ice sheet appears clearly in the simulation, and it is also striking to see the north-east extension of the observed deposits in Utopia Planitia (figure B.5), where the model predicts a passing of the low pressure systems (see figure C.14).

4.1.4 Schiaparelli Crater (6)

This region shows a stripped terrain which could have been more volatile-rich, and an unusual abundance of pedestal craters [Schultz and Lutz, 1988]. Condensation on dust cores and precipitation could easily form ice deposits which, after sublimation, leave this dust deposit. The same process could occur over Valles Marineris, and explain part of the thick friable layered deposits observed by [Hynek et al., 2003].

4.2 An updated climatic scenario for the Martian Ice Ages

The good agreement of our simulations with the geological observations and the orbital constraints given by the sensitivity studies of section 3.3 allow us to propose an updated scenario for the Martian Ice Ages.

Supposing that we start from a past Martian climate similar to the one observed today, an increase of obliquity would result in the sublimation of the north polar cap, and formation of tropical mountain glaciers with an accumulation rate up to $\sim 60mm.yr^{-1}$ with 45^o of obliquity [Levrard et al., 2004, Forget et al., 2006]. Given the typical periodicity of an obliquity cycle, we can generally say that the obliquity stays higher than 35^o for approximately 50 ky, and the resulting thickness of the tropical mountain glaciers would be ~ 3km, within an order of magnitude of the observations [Shean et al., 2005] (we neglect

the effect of the sublimation dust lag [Mischna and Richardson, 2005], and suppose that the sublimation is sufficient to create a major equatorial source of water). After this excursion, obliquity falls again around 35^o, and given the high dust content of the atmosphere under these conditions [Newman et al., 2005], an increased water cycle results in large mid-latitude precipitation controlled by strong stationary planetary waves. The propagation of baroclinic waves, stabilized by the topographic high of the dichotomy boundary (see figure C.14), favors the accumulation of snow in Deuteronilus, Protonilus, and Nilosyrtis Mensae, and results in the formation of a regional ice sheet. If we consider a high mean obliquity cycle, the system can sustain mid-latitude glaciation by staying in the $25 - 35^o$ obliquity range given in section 3.3, until a new high obliquity excursion occurs. The resulting period of time of approximately 50 ky could create, if we suppose accumulation rates around $10 - 20mm.yr^{-1}$ (see Table 3.1), an ice sheet of $500 - 1000$m thickness. Furthermore, during this period, if we consider that a lower dust opacity is likely to occur when the obliquity is only 25^o, our simulations show that the baroclinic waves and precipitation associated with transient weather systems are still active, but with decreased accumulation of $\sim 1 - 2mm.yr^{-1}$ and increased sublimation during the summer. Could this lower regime of glaciation explain the formation of smaller lobate debris aprons emerging from north facing alcoves, where the snow is preserved during the summer ?

A question we need to adress is the stability of the mid-latitude ice sheet as we start a new high obliquity excursion ($\sim 45^o$). The ice sheet, without precipitation, and under this high obliquity, is likely to retreat, resulting in the observed remnant integrated glacial systems in the fretted terrains. Of course, a perfect scenario would be a retreat of the ice sheet, but also a return of the sublimated ice to the tropical mountain glaciers. In that case, the obliquity cycle would be closed, and a high mean obliquity period would result in the oscillations of the ice reservoirs between the tropical mountain glaciers and the mid-latitudes, producing consistent stratigraphy in both deposits.

Consequently these results suggest that ice ages on Mars are dusty and generally high mean obliquity, as opposed to interglacial low mean obliquity periods, where the ice is stable at both poles. The deposits of the mid-latitudes are estimated to be Late Amazonian (~ 300Ma) [Head et al., 2006a]. To sustain glaciation during all that period of time, high mean obliquity regimes $\epsilon = 35 \pm 10^o$ probably occured many times during the last 300Ma, and allow us to better constrain the orbital predictions. Another essential observation is the formation of thinner mantling ice deposits in high latitudes during these high mean obliquity periods (see panels 2. and 3. in figure C.16), which may account for the layered mantling deposits observed by [Head et al., 2003b]. If we consider that the equatorial water source disappeared during the last transition period [Levrard et al., 2004], this last observation would suggest that the water-ice-rich mantling deposits formed during the last high mean obliquity period, and could be consequently older than 5 Myr.

CHAPTER 5

Conclusion

A new challenge

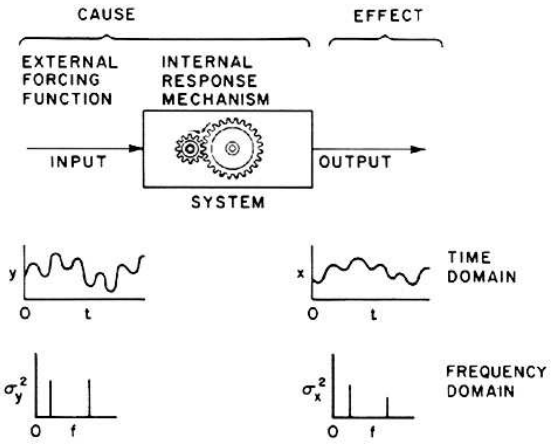

This study is a first step in the climatic understanding of the northern mid-latitude glaciation. It reveals a fascinating meteorology of the mid-latitudes during periods of high mean obliquity, created by an equatorial source of water and a relatively high dust content of the atmosphere. The major role played by the baroclinic waves in the mid-latitude glaciation is particularly interesting, because it suggests a strong interaction with dust storms, partly resulting from the same process. Major improvements by coupling the water cycle and the dust cycle and taking into account the radiative feedbacks of water vapour and ice crystals should greatly improve our understanding of the martian paleoclimate in the next couple of years.

The detailed analysis of the mid-latitude geomorphology, in the light of terrestrial analogs, such as the Dry Valleys of Antarctica, should also provide major insights into the microclimate and water budget of the martian glacial systems. A comparison of these detailed observations with GCM predictions, and possible meso-scale models, would greatly improve our knowledge of the mid-latitude glaciation.

The simple scheme above, made by John Imbrie in 1982, is maybe the best way to conclude our study. During this project, we simply found a new mechanism of the climatic "system" which accounts for a large signal of the "output", the mid-latitude glaciation, by varying the "input", the orbital parameters. Now, we have to understand the higher harmonics of the Martian geology and continue the exploration of the martian climatic "system", which could also help us, by its great similarities, to better understand the atmospheric dynamics of the Earth.

Acknowledgements

I would like to thank Jim Head for supervising this great project, for being always encouraging and captivated, for all these fascinating discussions we had and for "making this a reality".

I am also grateful to Misha Kreslavsky for very useful discussions, and to François Forget, Benjamin Levrard, and Franck Montmessin who constantly helped me to explore the Martian ice ages.

I would need a whole chapter to thank everybody, but I'm especially grateful to Anne Cote and Nancy Christy, the team of the Center for Computation and Visualization (Prabhat, Andrew Forsberg, Matthew Cannizzaro, George Loriot, and Melih Bitim), the bureautics team of LFDJ in France for providing the laptop I used for all this work, Ehouarn Millour, Robert Franchisseur, Aline Gendrin, Jay Dickson (merci beaucoup Monsieur), Caleb Fassett, Peter Neivert, Dave Shean, Joe Levy, Gareth Morgan, Peter Isaacson, Wes Patterson, Noah Petro, John Coutu and all the people from Brown University and Providence for bearing my French accent and teaching me "what America is all about" ! Finally, a huge "merci" to all my family and friends across the ocean.

And thanks to you, if you are not mentioned above, for reaching the end of this (fascinating) report !

LIST OF FIGURES

LIST OF TABLES

BIBLIOGRAPHY

[Böttger et al., 2005] Böttger, H. M., Lewis, S. R., Read, P. L., and Forget, F. (2005). The effects of the martian regolith on GCM water cycle simulations. *Icarus*, 177:174–189.

[Boynton et al., 2004] Boynton, W. V., Feldman, W. C., Mitrofanov, I. G., Evans, L. G., Reedy, R. C., Squyres, S. W., Starr, R., Trombka, J. I., D'Uston, C., Arnold, J. R., Englert, P. A. J., Metzger, A. E., Wänke, H., Brückner, J., Drake, D. M., Shinohara, C., Fellows, C., Hamara, D. K., Harshman, K., Kerry, K., Turner, C., Ward, M., Barthe, H., Fuller, K. R., Storms, S. A., Thornton, G. W., Longmire, J. L., Litvak, M. L., and Ton'chev, A. K. (2004). The Mars Odyssey Gamma-Ray Spectrometer Instrument Suite. *Space Science Reviews*, 110:37–83.

[Cantor et al., 1999] Cantor, B. A., James, P. B., Wolff, M. J., Malin, M. C., Jensen, E., and Edgett, K. S. (1999). Local Dust Storms in the Martian Northern Hemisphere: 1998 MGS/MOC Observations. In *The Fifth International Conference on Mars, July 19-24, 1999, Pasadena, California, abstract no. 6140*, pages 6140–+.

[Christensen et al., 2001] Christensen, P. R., Bandfield, J. L., Hamilton, V. E., Ruff, S. W., Kieffer, H. H., Titus, T. N., Malin, M. C., Morris, R. V., Lane, M. D., Clark, R. L., Jakosky, B. M., Mellon, M. T., Pearl, J. C., Conrath, B. J., Smith, M. D., Clancy, R. T., Kuzmin, R. O., Roush, T., Mehall, G. L., Gorelick, N., Bender, K., Murray, K., Dason, S., Greene, E., Silverman, S., and Greenfield, M. (2001). Mars Global Surveyor Thermal Emission Spectrometer experiment: Investigation description and surface science results. *Journal of Geophysical Research*, 106:23823–23872.

[Christensen et al., 2004] Christensen, P. R., Jakosky, B. M., Kieffer, H. H., Malin, M. C., McSween, Jr., H. Y., Nealson, K., Mehall, G. L., Silverman, S. H., Ferry, S., Caplinger, M., and Ravine, M. (2004). The Thermal Emission Imaging System (THEMIS) for the Mars 2001 Odyssey Mission. *Space Science Reviews*, 110:85–130.

[Clancy et al., 1996] Clancy, R. T., Grossman, A. W., Wolff, M. J., James, P. B., Rudy, D. J., Billawala, Y. N., Sandor, B. J., Lee, S. W., and Muhleman, D. O. (1996). Water vapor

saturation at low altitudes around Mars aphelion: A key to Mars climate? *Icarus*, 122:36–62.

[Collins et al., 1996] Collins, M., Lewis, S. R., Read, P. L., and Hourdin, F. (1996). Baroclinic Wave Transitions in the Martian Atmosphere. *Icarus*, 120:344–357.

[Conrath et al., 2000] Conrath, B. J., Pearl, J. C., Smith, M. D., Maguire, W. C., Christensen, P. R., Dason, S., and Kaelberer, M. S. (2000). Mars Global Surveyor Thermal Emission Spectrometer (TES) observations: Atmospheric temperatures during aerobraking and science phasing. *Journal of Geophysical Research*, 105:9509–9520.

[Fassett and Head, 2006] Fassett, C. I. and Head, III, J. W. (2006). Valleys on Hecates Tholus, Mars: origin by basal melting of summit snowpack. *Planetary and Space Science*, 54:370–378.

[Forget, 1998] Forget, F. (1998). Improved optical properties of the Martian atmospheric dust for radiative transfer calculations in the infrared. *Geophysical Research Letters*, 25:1105–1108.

[Forget et al., 2006] Forget, F., Haberle, R. M., Montmessin, F., Levrard, B., and Head, J. W. (2006). Formation of Glaciers on Mars by Atmospheric Precipitation at High Obliquity. *Science*, 311:368–371.

[Forget et al., 2005] Forget, F., Hourdin, F., Dassas, K., Hourdin, C., and Wanherdrick, Y. (2005). User Manual for the LMD Martian Atmospheric General Circulation Model.

[Forget et al., 1999a] Forget, F., Hourdin, F., Fournier, R., Hourdin, C., Talagrand, O., Collins, M., Lewis, S. R., Read, P. L., and Huot, J.-P. (1999a). Improved general circulation models of the Martian atmosphere from the surface to above 80 km. *Journal of Geophysical Research*, 104:24155–24176.

[Forget et al., 1999b] Forget, F., Hourdin, R., Hourdin, C., Collins, M., Lewis, S. R., and Fournier, R. (1999b). Updated Detailed Design Document for the Martian GCM. *ESA Work Package 6*.

[Forget et al., 1995] Forget, F., Hourdin, R., Hourdin, C., Talagrand, O., Collins, M., Lewis, S. R., and Read, P. L. (1995). The Martian Environment. *ESA Work Package 1*.

[Haberle et al., 2003] Haberle, R. M., Murphy, J. R., and Schaeffer, J. (2003). Orbital change experiments with a Mars general circulation model. *Icarus*, 161:66–89.

[Head et al., 2001] Head, J. W., Greeley, R., Golombek, M. P., Hartmann, W. K., Hauber, E., Jaumann, R., Masson, P., Neukum, G., Nyquist, L. E., and Carr, M. H. (2001). Geological Processes and Evolution. *Space Science Reviews*, 96:263–292.

[Head et al., 2006a] Head, J. W., Marchant, D. R., Agnew, M. C., Fassett, C. I., and Kreslavsky, M. A. (2006a). Extensive valley glacier deposits in the northern mid-latitudes of Mars: Evidence for Late Amazonian obliquity-driven climate change. *Earth and Planetary Science Letters*, 241:663–671.

[Head et al., 2003a] Head, J. W., Marchant, D. R., Shean, D. E., and Milkovich, S. M. (2003a). Tropical Cold-Based Mountain Glaciers on Mars: Evidence for Significant Amazonian Climate Change. *AGU Fall Meeting Abstracts*, pages C7+.

[Head et al., 2003b] Head, J. W., Mustard, J. F., Kreslavsky, M. A., Milliken, R. E., and Marchant, D. R. (2003b). Recent ice ages on Mars. *Nature*, 426:797–802.

[Head et al., 2006b] Head, J. W., Nahm, A. L., Marchant, D. R., and Neukum, G. (2006b). Modification of the dichotomy boundary on Mars by Amazonian mid-latitude regional glaciation. *Geophysical Research Letters*, 33:8–+.

[Head et al., 2005] Head, J. W., van Dam, A., Fulcomer, S., Forsberg, A., Rosser, G., and Milkovich, S. M. (2005). ADVISER: Immersive Scientific Visualization Applied to Mars Research and Exploration. *Photogrammetric Engineering and Remote Sensing*, 71(10):1219.

[Head and Marchant, 2006] Head, III, J. W. and Marchant, D. R. (2006). Evidence for Global-Scale Northern Mid-Latitude Glaciation in the Amazonian Period of Mars: Debris-covered Glacier and Valley Glacier Deposits in the 30-50N Latitude Band. In Mackwell, S. and Stansbery, E., editors, *37th Annual Lunar and Planetary Science Conference*, pages 1127–+.

[Hide and Mason, 1975] Hide, R. and Mason, P. J. (1975). Sloping convection in a rotating fluid. *Advances in Physics*, 24(1):47–100.

[Hollingsworth and Barnes, 1996] Hollingsworth, J. L. and Barnes, J. R. (1996). Forced stationary waves in Mars winter atmosphere. *Journal of the Atmospheric Sciences*, 53(3):428–447.

[Hollingsworth et al., 1996] Hollingsworth, J. L., Haberle, R. M., Bridger, A. F. C., Pollack, J. B., Lee, H., and Schaeffer, J. (1996). Orographic control of storm zones on Mars. *Nature*, 380:413–416.

[Hourdin, 1992] Hourdin, F. (1992). A new representation of the absorption by the CO2 15-microns band for a Martian general circulation model. *Journal of Geophysical Research*, 97:18319–+.

[Hourdin et al., 1993] Hourdin, F., Le van, P., Forget, F., and Talagrand, O. (1993). Meteorological variability and the annual surface pressure cycle on Mars. *Journal of Atmospheric Sciences*, 50:3625–3640.

[Hynek et al., 2003] Hynek, B. M., Phillips, R. J., and Arvidson, R. E. (2003). Explosive volcanism in the Tharsis region: Global evidence in the Martian geologic record. *Journal of Geophysical Research (Planets)*, 108:15–1.

[Ivanov and Head, 2006] Ivanov, M. A. and Head, J. W. (2006). Alba Patera, Mars: Topography, Structure, and Evolution of a Unique Late Hesperian-Early Amazonian Shield Volcano. *Journal of Geophysical Research (Planets)*.

[James et al., 1996] James, P. B., Bell, J. F., Clancy, R. T., Lee, S. W., Martin, L. J., and Wolff, M. J. (1996). Global imaging of Mars by Hubble space telescope during the 1995 opposition. *Journal of Geophysical Research*, 101:18883–18890.

[Joshi et al., 1997] Joshi, M. M., Haberle, R. M., Barnes, J. R., Murphy, J. R., and Schaeffer, J. (1997). Low-level jets in the NASA Ames Mars general circulation model. *Journal of Geophysical Research*, 102:6511–6524.

[Kieffer et al., 1992] Kieffer, H. H., Jakosky, B. M., Snyder, C. W., and Matthews, M. S. (1992). *Mars*. The University of Arizona Press.

[Kreslavsky and Head, 2000] Kreslavsky, M. A. and Head, J. W. (2000). Kilometer-scale roughness of Mars: Results from MOLA data analysis. *Journal of Geophysical Research*, 105:26695–26712.

[Laskar et al., 2004] Laskar, J., Correia, A. C. M., Gastineau, M., Joutel, F., Levrard, B., and Robutel, P. (2004). Long term evolution and chaotic diffusion of the insolation quantities of Mars. *Icarus*, 170:343–364.

[Laskar et al., 2002] Laskar, J., Levrard, B., and Mustard, J. F. (2002). Orbital forcing of the martian polar layered deposits. *Nature*, 419:375–377.

[Leovy, 2001] Leovy, C. (2001). Weather and Climate on Mars. *Nature*, 412:245–249.

[Levrard et al., 2004] Levrard, B., Forget, F., Montmessin, F., and Laskar, J. (2004). Recent ice-rich deposits formed at high latitudes on Mars by sublimation of unstable equatorial ice during low obliquity. *Nature*, 431:1072–1075.

[Masson et al., 2001] Masson, P., Carr, M. H., Costard, F., Greeley, R., Hauber, E., and Jaumann, R. (2001). Geomorphologic evidence for liquid water. *Space Science Reviews*, 96:333–364.

[Milkovich and Head, 2005] Milkovich, S. M. and Head, J. W. (2005). North polar cap of Mars: Polar layered deposit characterization and identification of a fundamental climate signal. *Journal of Geophysical Research (Planets)*, 110:1005–+.

[Milkovich et al., 2006] Milkovich, S. M., Head, J. W., and Marchant, D. R. (2006). Debris-covered piedmont glaciers along the northwest flank of the Olympus Mons scarp: Evidence for low-latitude ice accumulation during the Late Amazonian of Mars. *Icarus*, 181:388–407.

[Mischna and Richardson, 2005] Mischna, M. A. and Richardson, M. I. (2005). A reanalysis of water abundances in the Martian atmosphere at high obliquity. *Geophysical Research Letters*, 32:3201–+.

[Mischna et al., 2003] Mischna, M. A., Richardson, M. I., Wilson, R. J., and McCleese, D. J. (2003). On the orbital forcing of Martian water and CO_2 cycles: A general circulation model study with simplified volatile schemes. *Journal of Geophysical Research (Planets)*, 108:16–1.

[Montmessin et al., 2004] Montmessin, F., Forget, F., Rannou, P., Cabane, M., and Haberle, R. M. (2004). Origin and role of water ice clouds in the Martian water cycle as inferred from a general circulation model. *Journal of Geophysical Research (Planets)*, 109:10004–+.

[Montmessin et al., 2002] Montmessin, F., Rannou, P., and Cabane, M. (2002). New insights into Martian dust distribution and water-ice cloud microphysics. *Journal of Geophysical Research (Planets)*, 107:4–1.

[Nayvelt et al., 1997] Nayvelt, L., Gierasch, P. J., and Cook, K. H. (1997). Modeling and Observations of Martian Stationary Waves. *Journal of the Atmospheric Sciences*, 54(8):986Ű1013.

[Newman et al., 2005] Newman, C. E., Lewis, S. R., and Read, P. L. (2005). The atmospheric circulation and dust activity in different orbital epochs on Mars. *Icarus*, 174:135–160.

[Newman et al., 2002] Newman, C. E., Lewis, S. R., Read, P. L., and Forget, F. (2002). Modeling the Martian dust cycle 2. Multiannual radiatively active dust transport simulations. *Journal of Geophysical Research (Planets)*, 107:7–1.

[Read and Lewis, 2004] Read, P. L. and Lewis, S. R. (2004). *The Martian Climate Revisited*. Springer.

[Richardson and Wilson, 2002] Richardson, M. I. and Wilson, R. J. (2002). Investigation of the nature and stability of the Martian seasonal water cycle with a general circulation model. *Journal of Geophysical Research (Planets)*, 107:7–1.

[Schultz and Lutz, 1988] Schultz, P. and Lutz, A. B. (1988). Polar wandering of Mars. *Icarus*, 73:91–141.

[Shean et al., 2005] Shean, D. E., Head, J. W., and Marchant, D. R. (2005). Origin and evolution of a cold-based tropical mountain glacier on Mars: The Pavonis Mons fan-shaped deposit. *Journal of Geophysical Research (Planets)*, 110:5001–+.

[Smith, 2002] Smith, M. D. (2002). The annual cycle of water vapor on Mars as observed by the Thermal Emission Spectrometer. *Journal of Geophysical Research (Planets)*, 107:25–1.

[Smith, 2004] Smith, M. D. (2004). Interannual variability in TES atmospheric observations of Mars during 1999-2003. *Icarus*, 167:148–165.

[Squyres, 1979] Squyres, S. W. (1979). The distribution of lobate debris aprons and similar flows on Mars. *Journal of Geophysical Research*, 84:8087–8096.

[Squyres and Knoll, 2005] Squyres, S. W. and Knoll, A. H. (2005). Sedimentary rocks at Meridiani Planum: Origin, diagenesis, and implications for life on Mars. *Earth and Planetary Science Letters*, 240:1–10.

[Wang and Ingersoll, 2002] Wang, H. and Ingersoll, A. P. (2002). Martian clouds observed by Mars Global Surveyor Mars Orbiter Camera. *Journal of Geophysical Research (Planets)*, 107:8–1.

APPENDIX A

Tables

Key parameters	Earth	Mars
Mean distance from Sun ($10^6 km$)	149.6 (1 UA)	227.9 (1.52 UA)
Obliquity ϵ	23.93^o	25.19^o
Eccentricity e	0.017	0.093
L_s of perihelion (L_p)	281^o	251^o
Solar constant ($W.m^{-2}$)	1380	594
Mean albedo	0.306	0.25
Rotation rate Ω ($10^{-5} s^{-1}$)	7.29	7.09
Year length (solar day sol)	365.24	668.6
Equatorial radius ($10^6 km$)	6378	3396
Surface gravity g ($m.s^{-2}$)	9.81	3.72
Mean surface pressure (hPa)	1013	6.1
Equilibrium temperature T_e (K)	256	210
Surface temperature range (K)	230-315	140-300
Typical zonal wind at jet level U ($m.s^{-1}$)	30	80
Atmospheric composition	N_2 77% - O_2 21% $H_2O < 3\%$ Ar 0.1% CO_2 0.037%	CO_2 95% - N_2 2.7% Ar 1.6% O_2 0.13% $H_2O < 0.05\%$
Cloud (or dust) fractional coverage	40%	5% (clouds) ; 0-100% (dust)
Main production process	Condensation	Dust lifting
Gas constant R ($m^2.s^{-2}.K^{-1}$)	287	192
Specific heat at constant pressure C_p ($m^2.s^{-2}.K^{-1}$)	1000	860
Scale height H_p (km)	7.5	10.8
Dry adiabatic lapse rate Γ_a ($K.km^{-1}$)	9.8	4.5
Buoyancy (Brunt-Väisäla) frequency N ($10^{-2} s^{-1}$)	1.1	0.6
Deformation radius L (km)	1100	920
Rossby number Ro	0.05	0.2

Table A.1: Orbital and atmospheric parameters of Earth and Mars
From [Read and Lewis, 2004], [Leovy, 2001] and [Forget et al., 1995]

Mission	Instrument	Description
Mars Global Surveyor March 1999 - Today	MOC	**Mars Orbital Camera** - Two different kinds of camera : - narrow-angle (NA) camera (highest resolution at the present time : $1.5m$ per pixel) - wide angle (WA) camera ($230m$ per pixel at nadir and $1.5km$ per pixel at limb)
	MOLA	**Mars Orbital Laser Altimeter :** - Topographic maps (spatial resolution of $\sim 4km$) [a] - Altitude profiles (spacing along track of $\sim 0.3km$) - Roughness and slope maps with different point-to-point distances (see [Kreslavsky and Head, 2000])
	TES	**Thermal Emission Spectrometer** [Christensen et al., 2001] - 3 spectral ranges covered by : 1) An Interferometric spectrometer (IR, 5.8 to $50\mu m$) 2) A thermal IR Radiometer (5.1 to $150\mu m$) 3) A visible-near IR Radiometer (0.3 to $2.9\mu m$) In these spectral ranges, TES can detect variations due to : CO_2 (absorption at $15\mu m$), water vapor ($25-50\mu m$ and $5.5-7.1\mu m$), dust (broad absorption with a peak at $9.3\mu m$), water-ice aerosols (broad peak near $12.1\mu m$ and sharper peak at $44.7\mu m$), and surface properties (window near $7.7\mu m$, mapping of the surface mineralogy at a spatial resolution of $3km$) [b]
Mars Odyssey February 2002 - Today	THEMIS	**THermal EMission Imaging System** [Christensen et al., 2004] : Visible ($0.42-0.86\mu m$) and thermal IR ($6.8-14.9\mu m$) camera Resolutions : $18m$ per pixel (visible) and $100m$ per pixel (thermal IR)
	GRS	**Gamma Ray Spectrometer** [Boynton et al., 2004] : Distribution of light elements (hydrogen)
Mars Express June 2003 - Today	HRSC	**High Resolution Stereo Camera** : Resolution of $12.5m$ per pixel and large spatial coverage (hundreds of km in width and thousands of km in length)

Table A.2: Spacecraft instruments used in this study

[a] GCM Topography
[b] GCM Thermal Inertia and Albedo maps

APPENDIX B

Maps

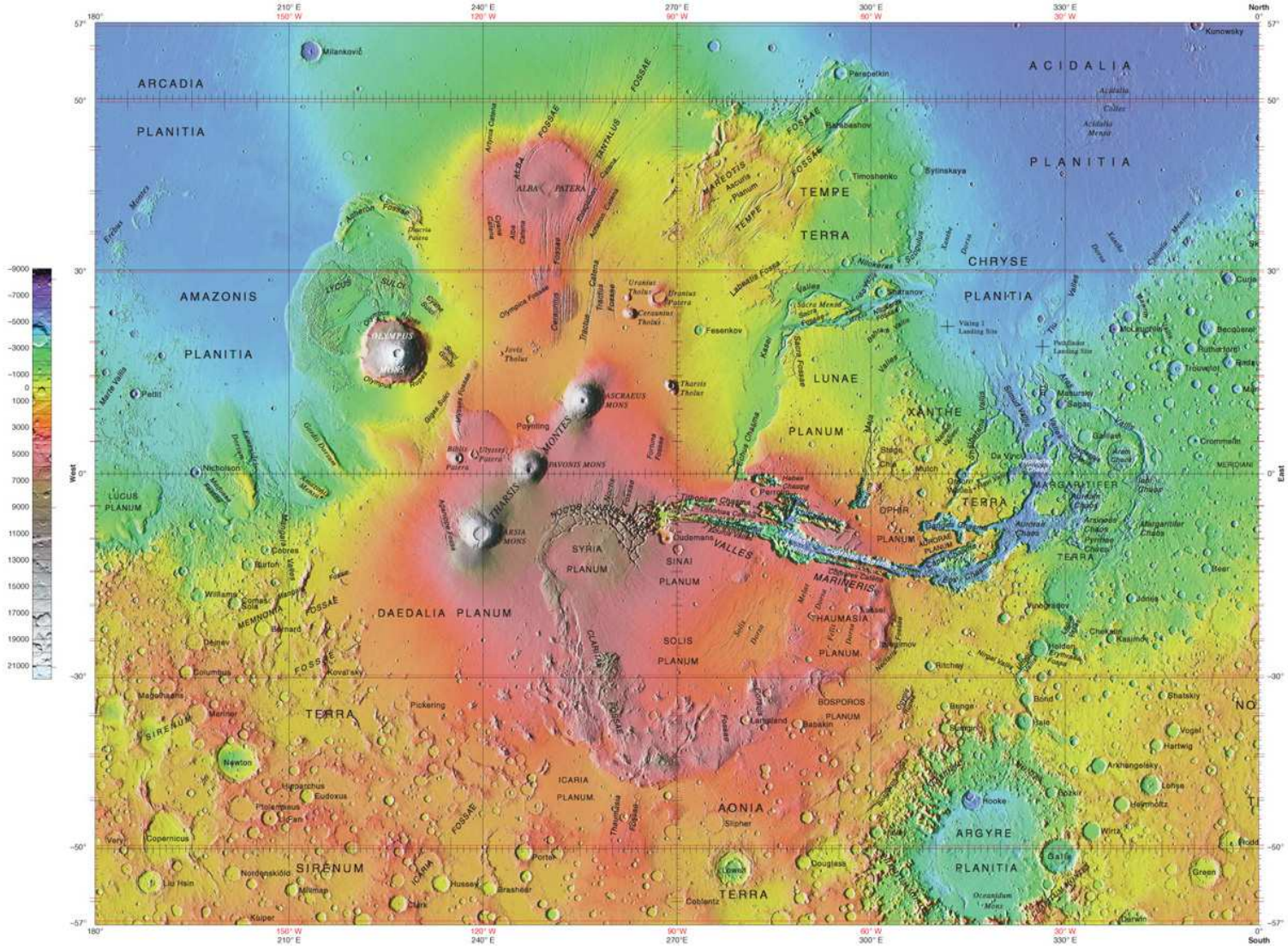

Figure B.1: Topographic map of Western Mars by USGS (MOLA measurements, cf appendix A.2)

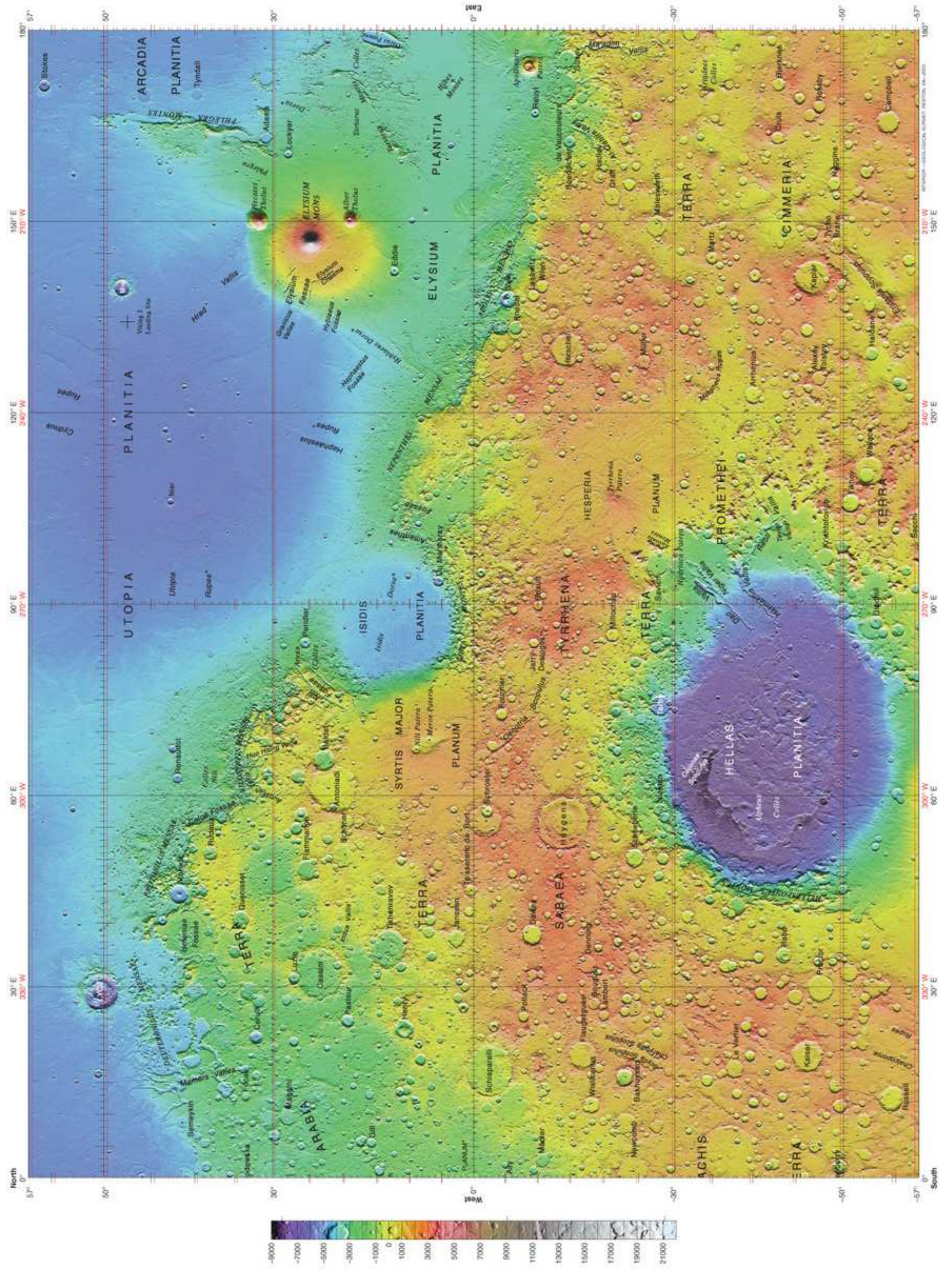

Figure B.2: Topographic map of Eastern Mars by USGS (MOLA measurements, cf appendix A.2)

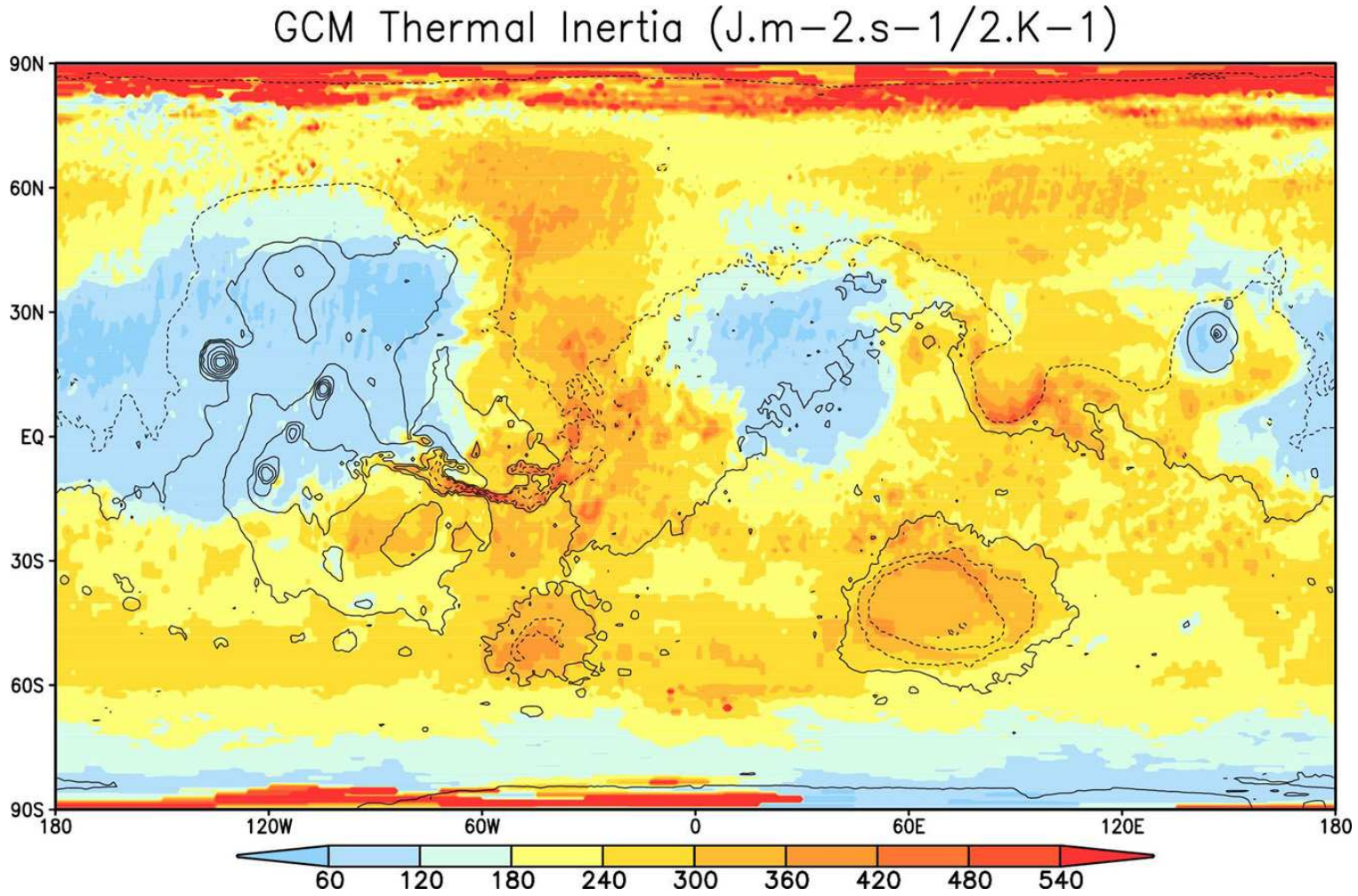

Figure B.3: GCM Thermal Inertia from Viking IRTM and Mars Global Surveyor TES observations

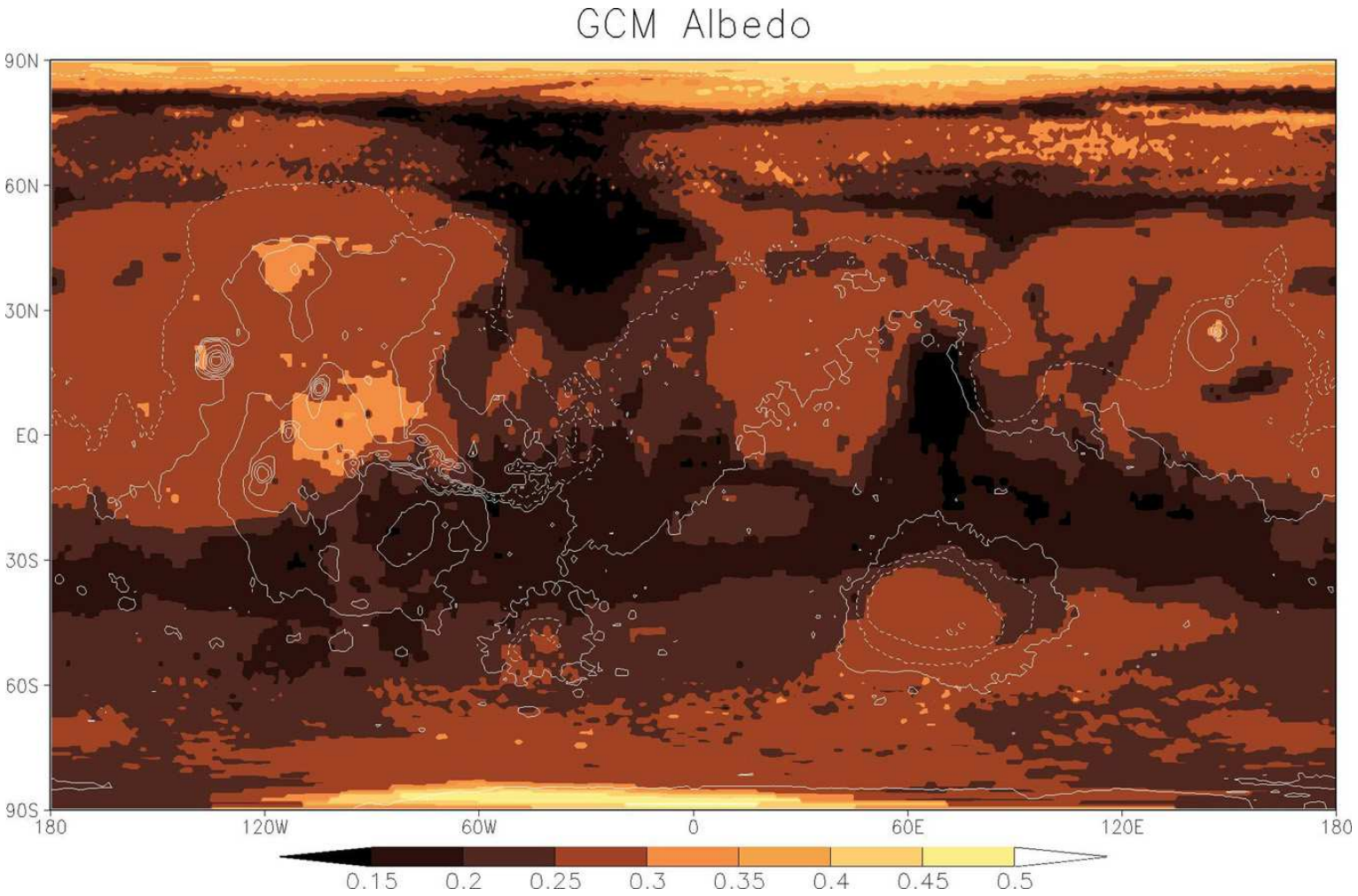

Figure B.4: GCM Albedo from Viking IRTM observations

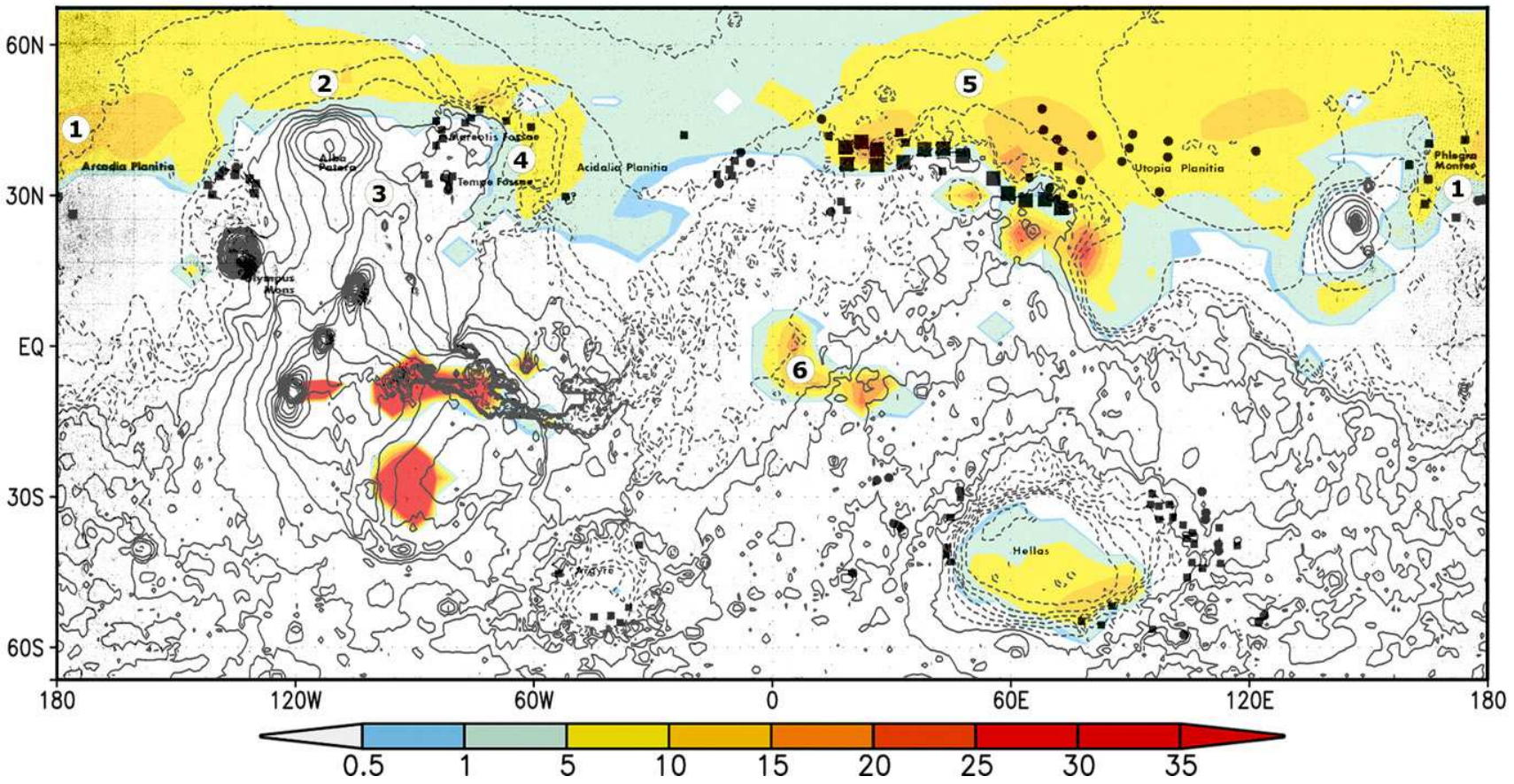

Figure B.5: GCM ice accumulation ($mm.yr^{-1}$) superposed on the map by [Squyres, 1979].
Present-day orbital parameters ($\epsilon = 25.19^o$, $e = 0.0934$, $L_p = 251^o$, $\tau = 2.5$), water source : equatorial.
Squares = lobate debris aprons (the large squares indicate regions of high concentration).
Circles = small impact craters with concentric fill.

APPENDIX C

Simulations

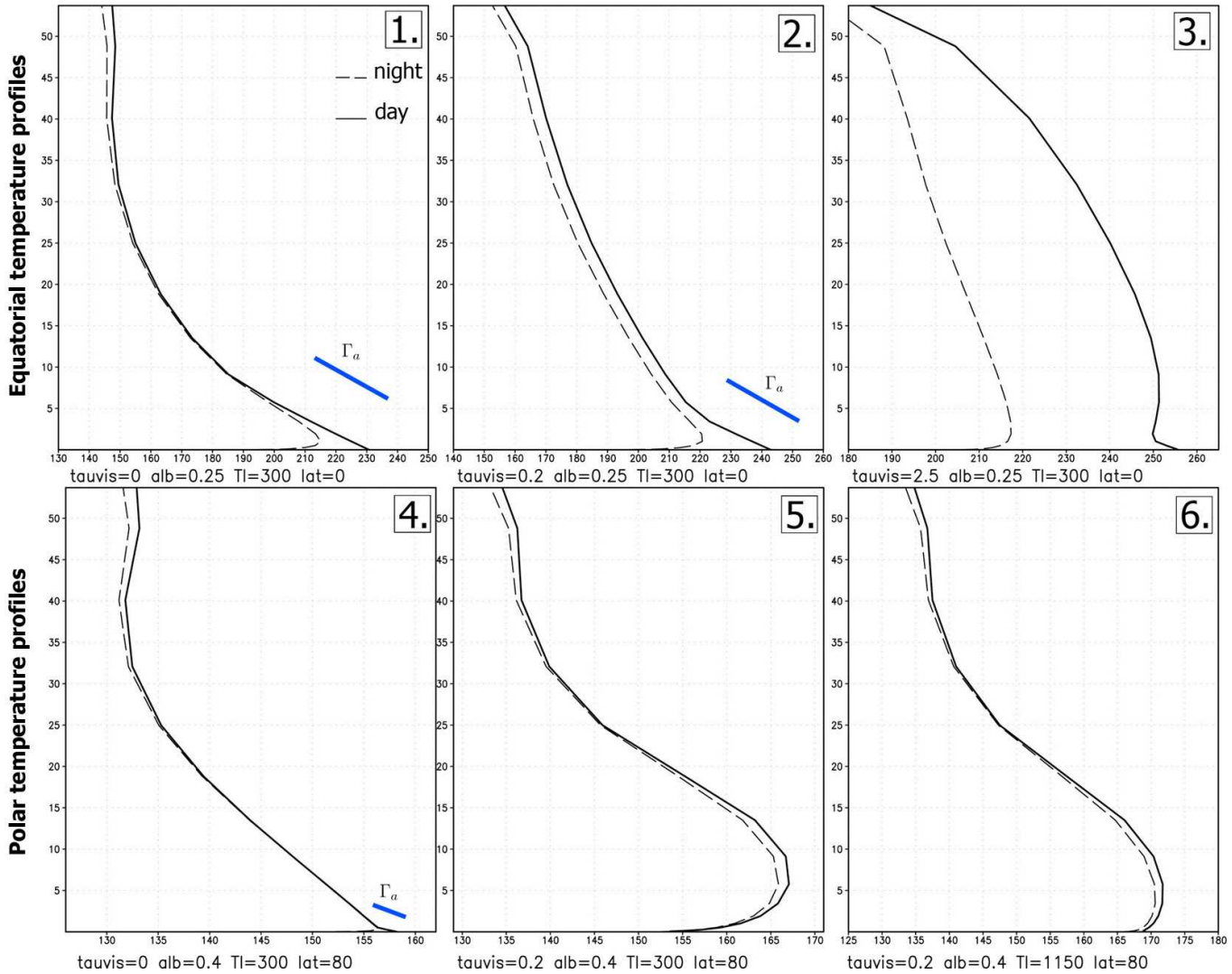

Figure C.1: Uni-dimensional simulations of different temperature profiles (K) at $L_s = 180^o$.
Two different latitudes (equator on top and 80^{o}N below) are represented, with different surface properties and dust contents. The vertical axis is altitude in kilometers.

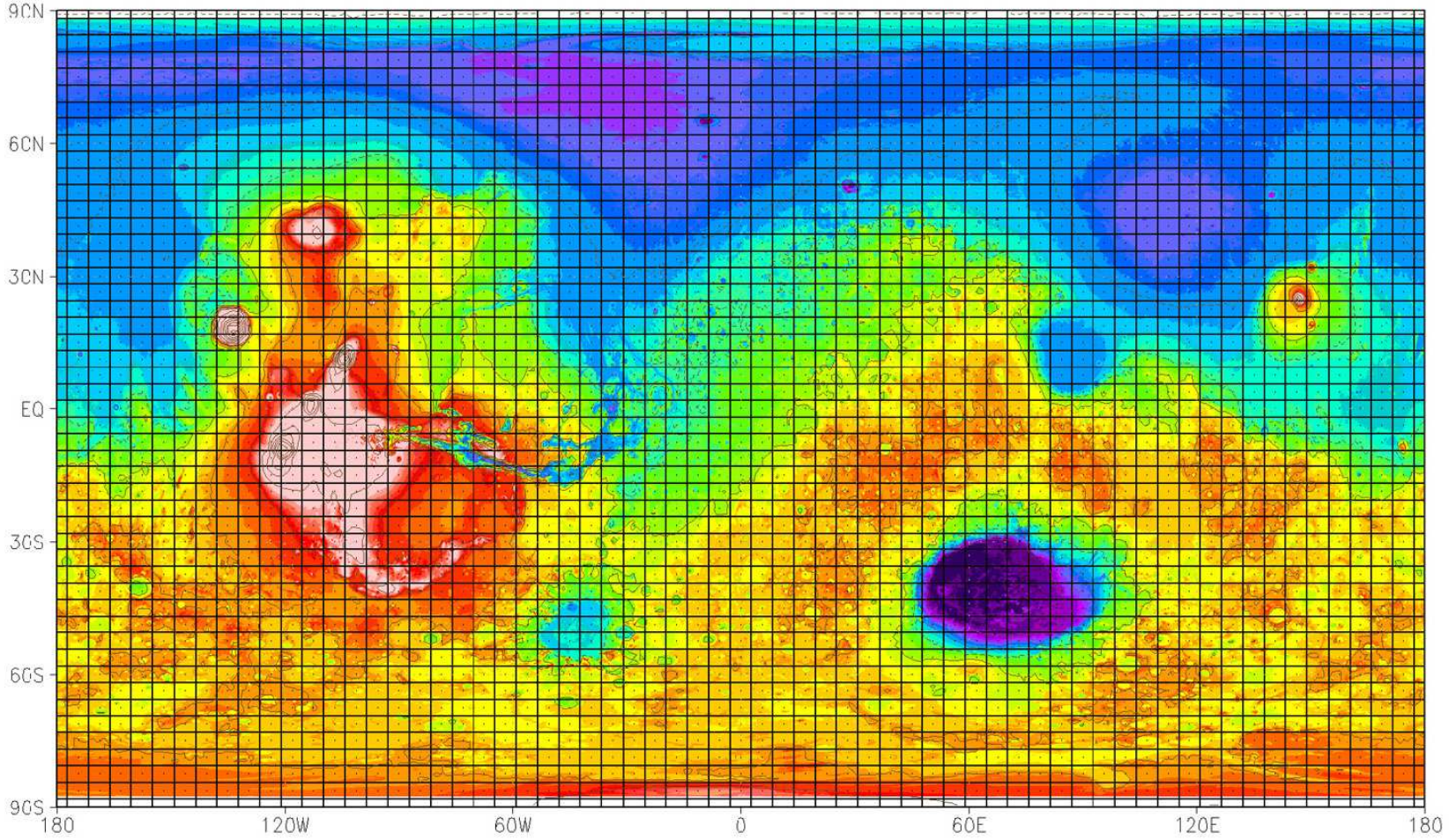

Figure C.2: GCM grid used in this study superposed on MOLA topography.
Longitude-latitude resolution is 64x48 points, ie $5.625^o \times 3.75^o$, or $\sim 300 \times 200$ km.

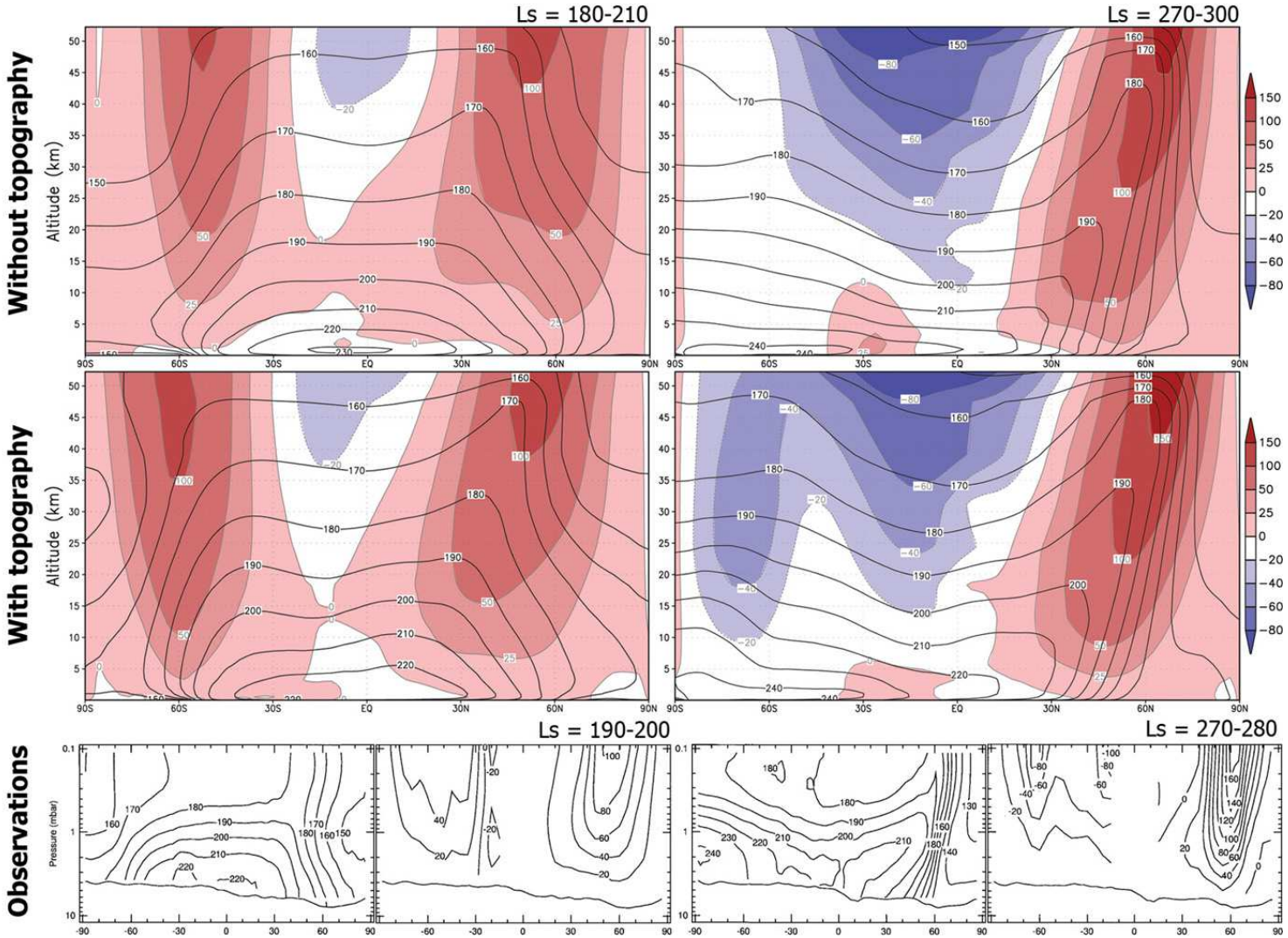

Figure C.3: Latitudinal slice of the Zonal winds ($m.s^{-1}$) and Temperature contours (K).
Upper panel : Aquaplanet under present-day orbital conditions, with $A = 0.22$ (albedo), $I = 247 J.m^{-2}.s^{-1/2}.K^{-1}$ (thermal inertia) and $\tau_{vis} = 0.2$.
Middle panel : Present-day Mars with the observed dust cycle (MGS scenario) - Lower panel : TES observations from [Conrath et al., 2000].

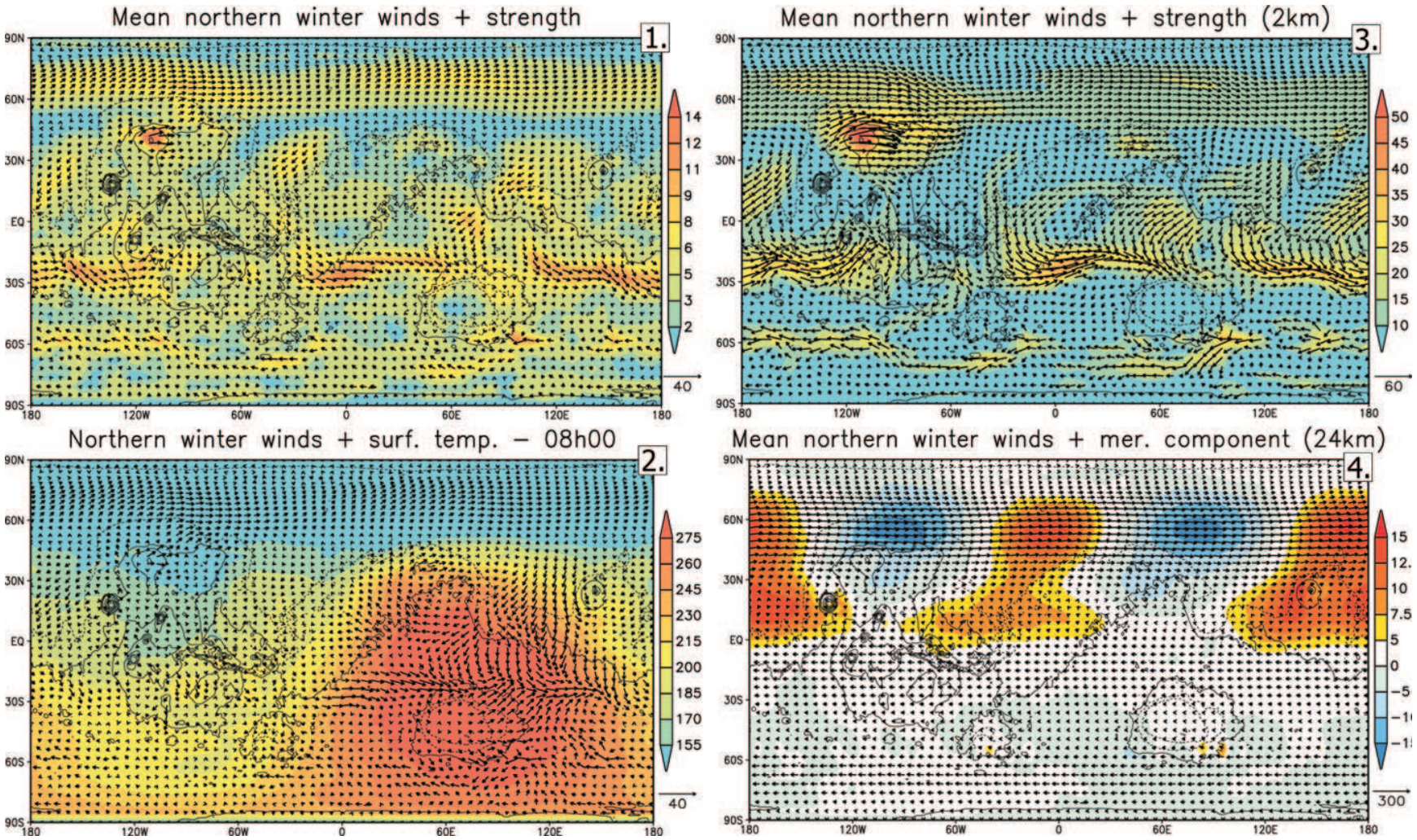

Figure C.4: GCM simulation of the northern winter circulation ($L_s = 270 - 300$).
1) Mean surface wind (5m) vectors and strength ($m.s^{-1}$), 2) Typical surface wind and temperature at 8h (universal time at 0^o longitude) 3) 2 km high general circulation (wind vectors and strength) 4) 24 km high circulation superposed on meridional winds.

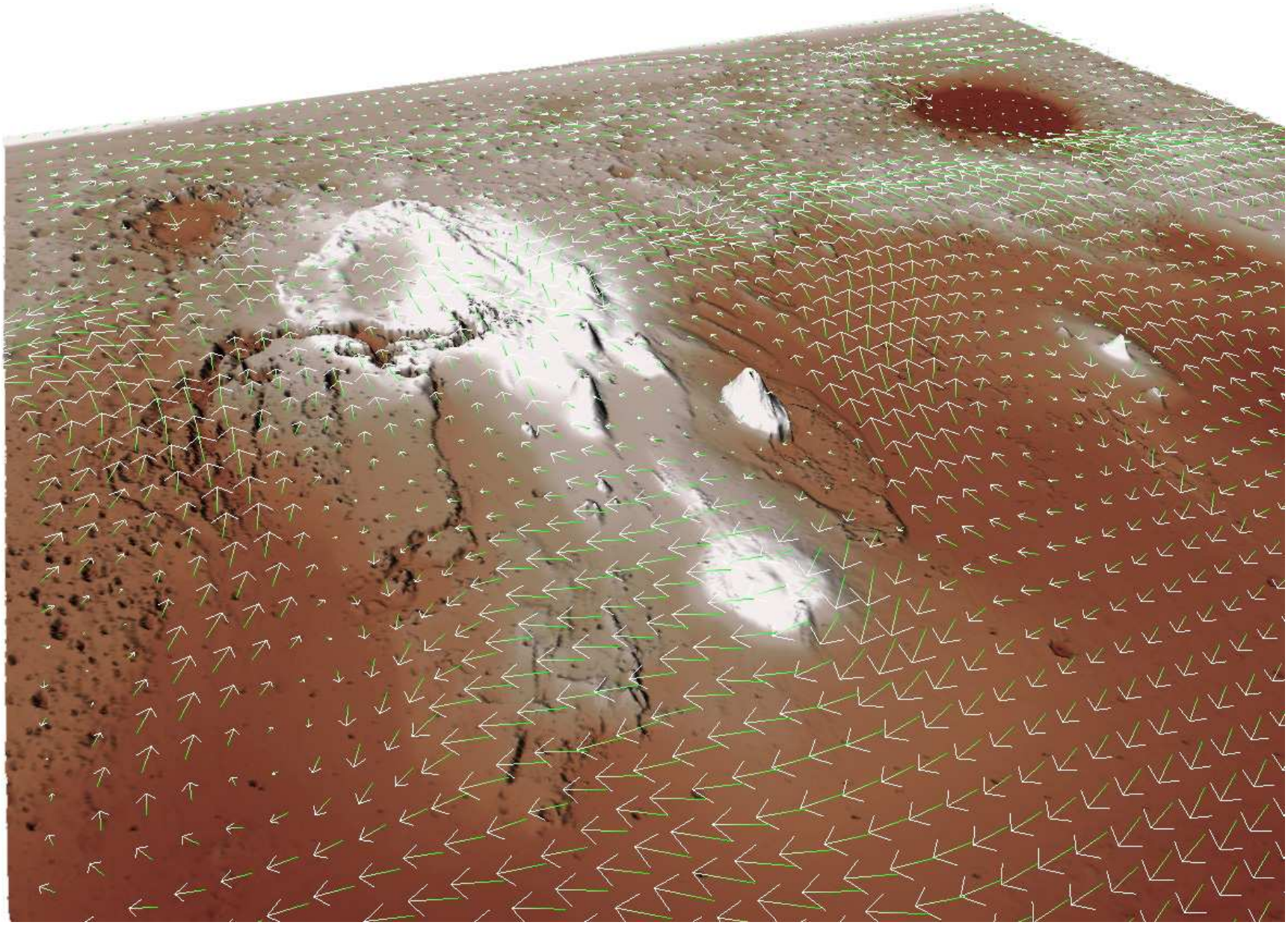

Figure C.5: Three dimensional view of the northern winter circulation (looking South).
These 2 km high winds are the same as on map 3. of figure C.4, but loaded on the CAVE Automatic Virtual Environment, a software developped by the team of the Center for Computation and Visualization (see [Head et al., 2005]). The topography is 30 times exaggerated.

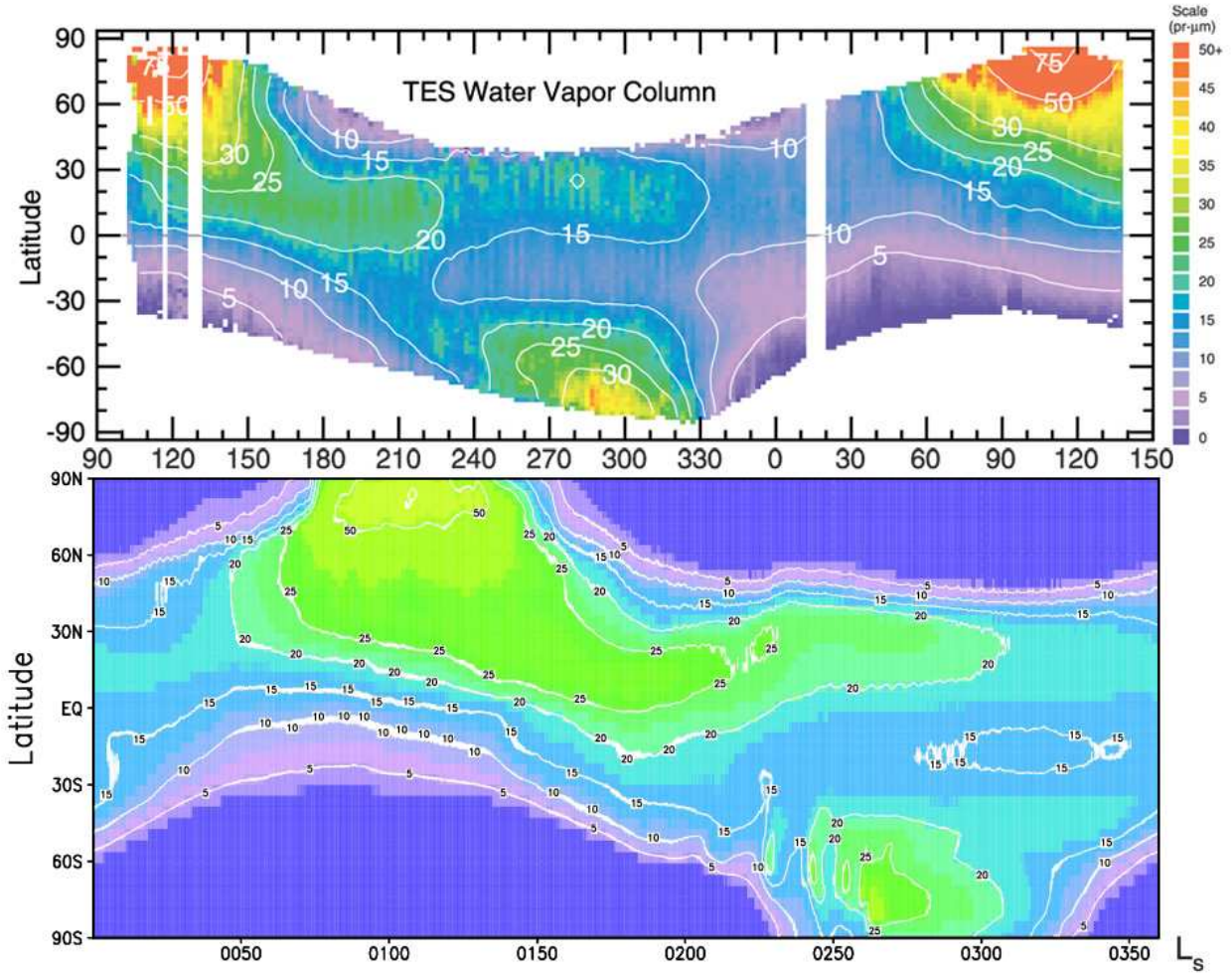

Figure C.6: Observed water column (μm) by TES and during the 6th year of simulation.
TES Data from [Smith, 2002]

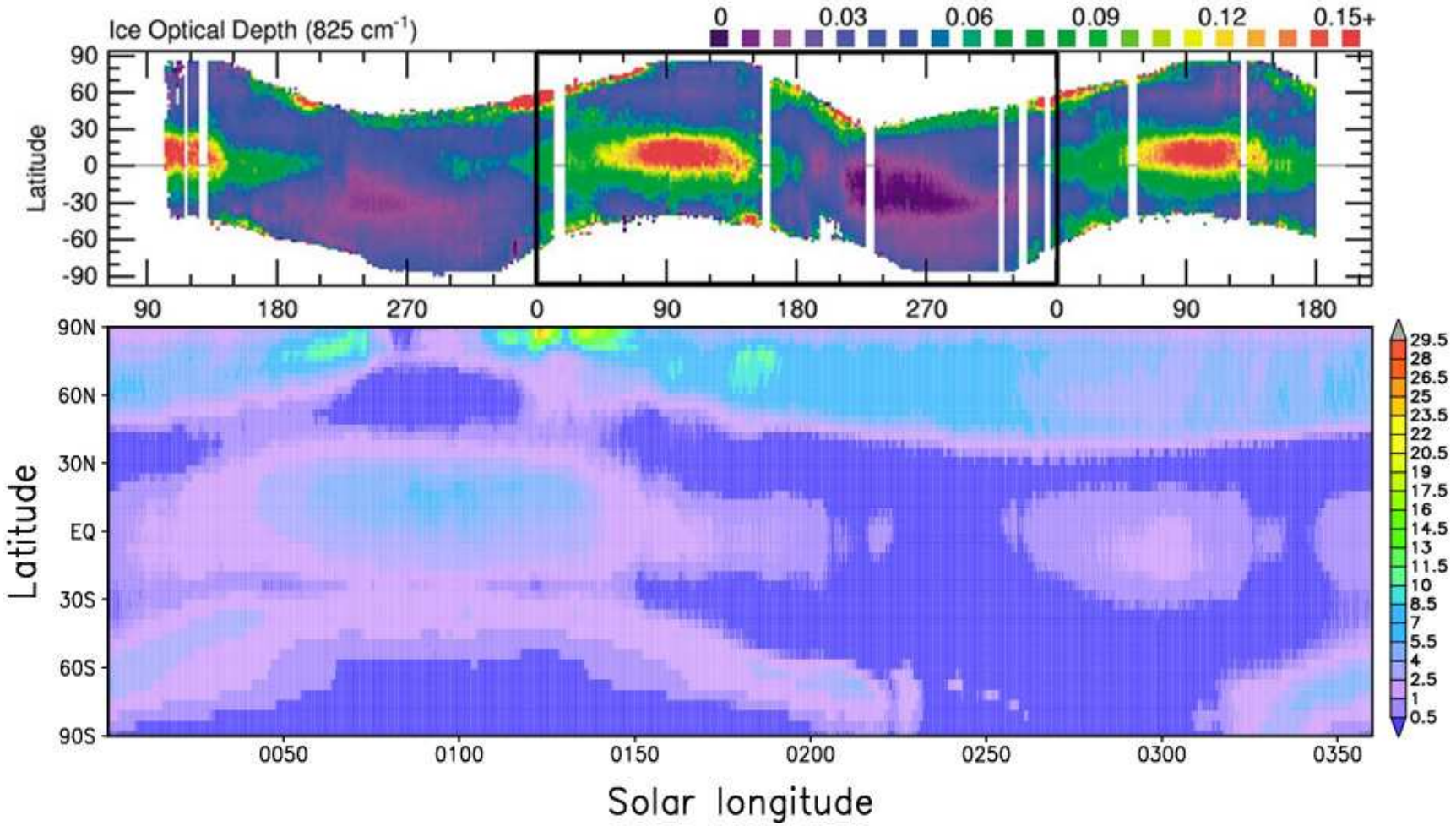

Figure C.7: Observed ice optical depth ($825cm^{-1}$) by TES and ice column (μm) during the 6th year of simulation.
TES Data from [Smith, 2004]

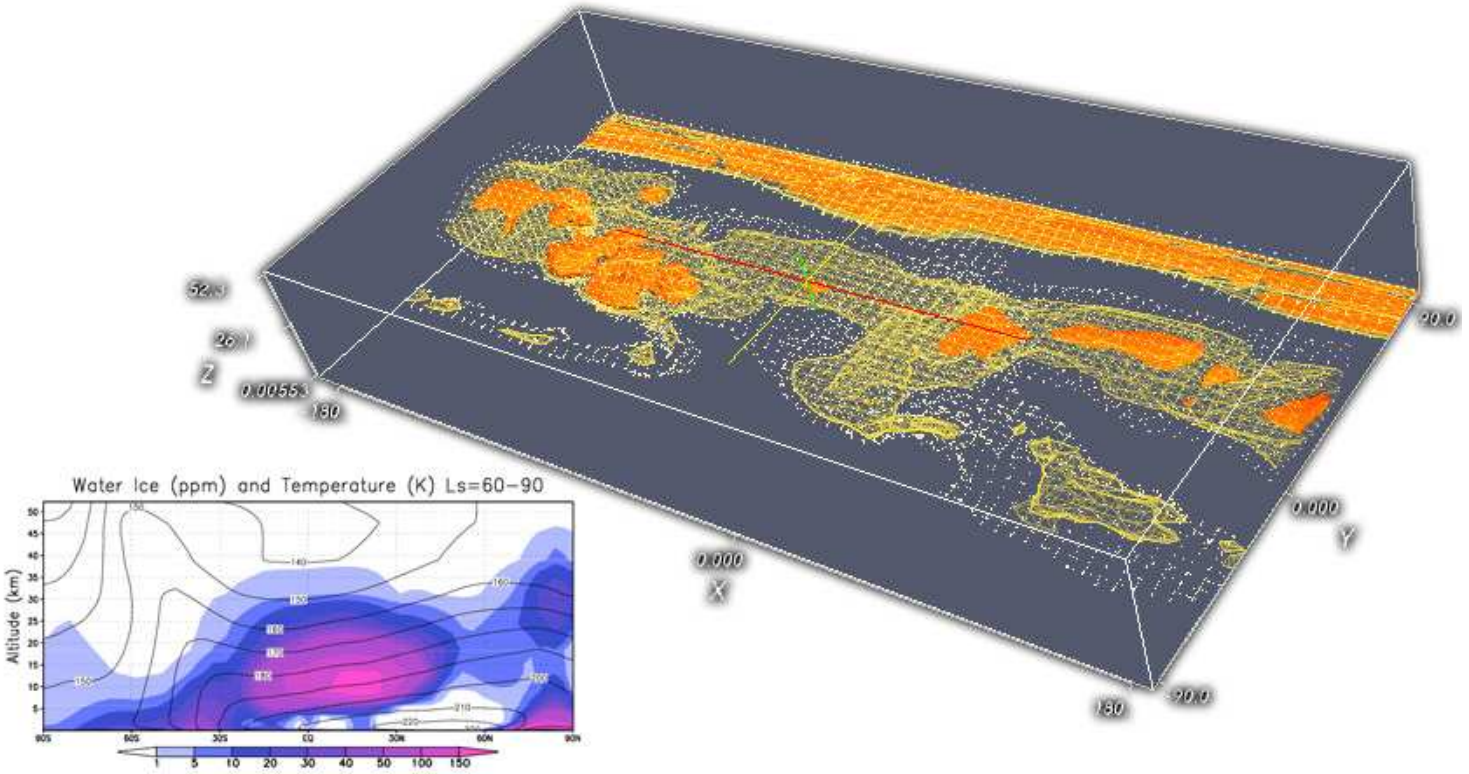

Figure C.8: Mean ice crystals spatial distribution at $L_s = 60 - 90^o$.
Data compiled by the team of the CCV and loaded in Paraview.

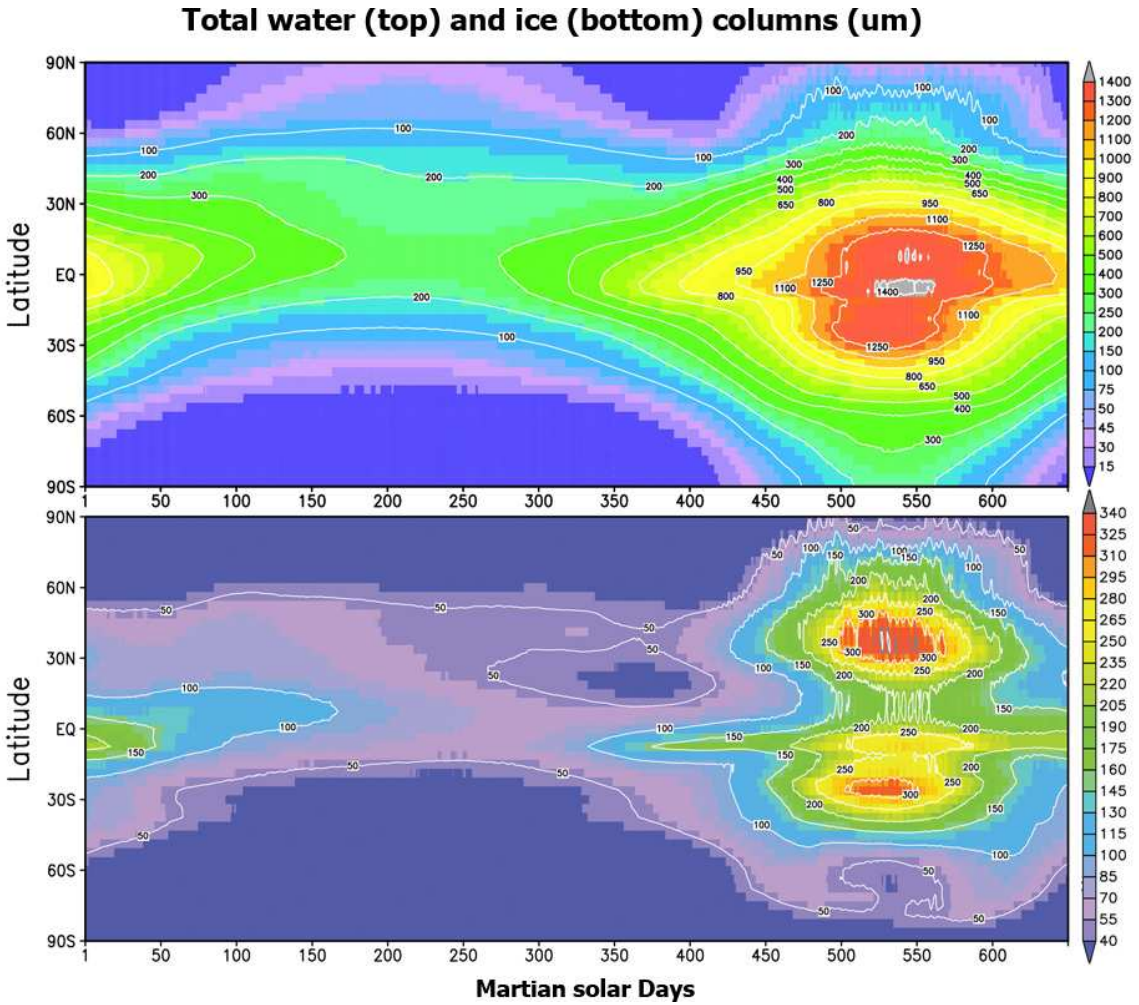

Figure C.9: Water and ice columns during the 6th year of simulation (μm).
$\epsilon = 15$, $e = 0.1$, $L_p = 270^o$, $\tau = 2.5$, water source : equatorial.

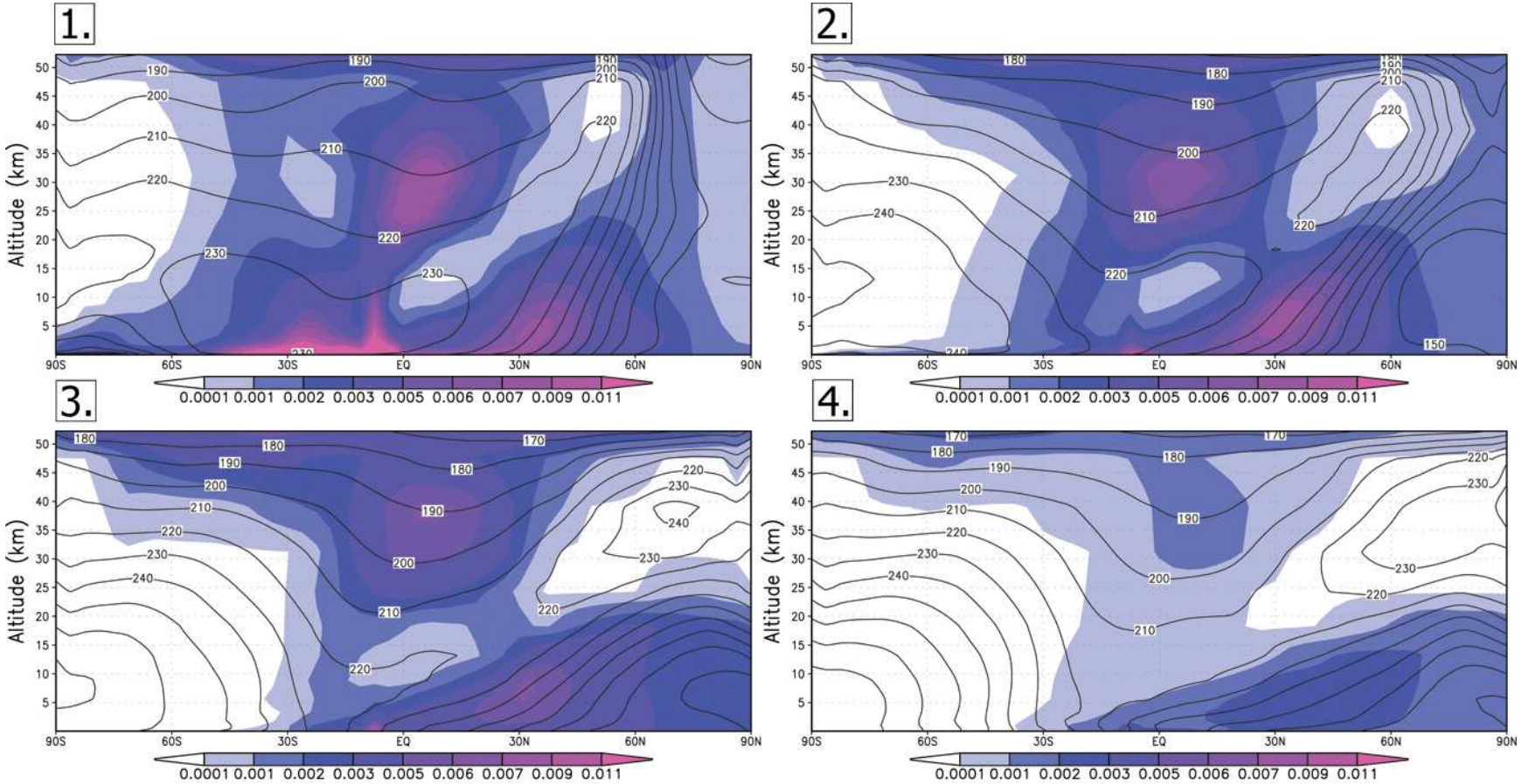

Figure C.10: Ice mixing ratio (shaded colors) and Temperature (K) for $\epsilon = 15 - 25 - 35 - 45^o$.
$e = 0.1$, $L_p = 270^o$, $\tau = 2.5$, water source : equatorial.

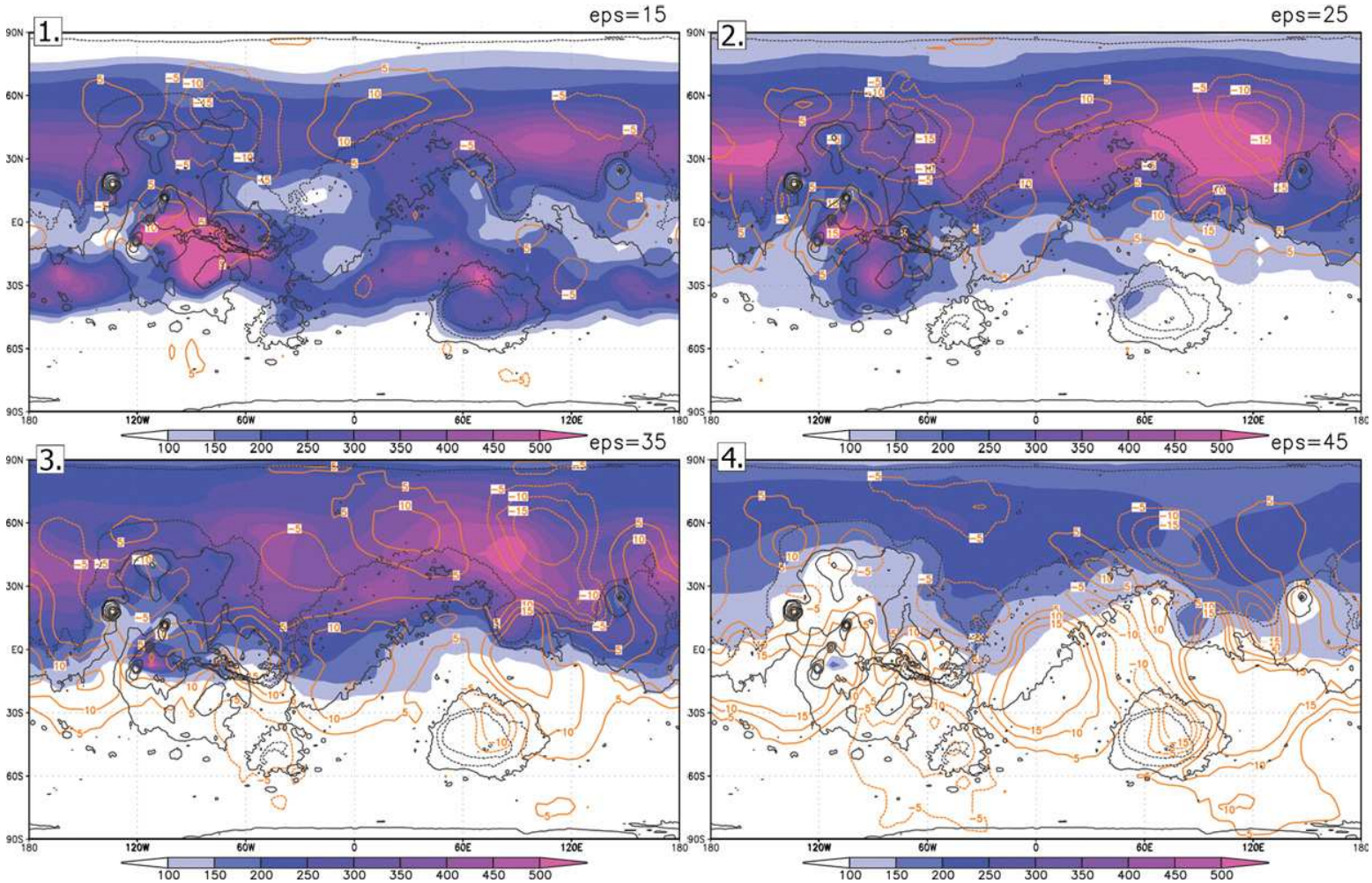

Figure C.11: Ice column (μm) and meridional winds at 13 km ($m.s^{-1}$) for $\epsilon = 15 - 25 - 35 - 45^o$.
$e = 0.1$, $L_p = 270^o$, $\tau = 2.5$, water source : equatorial.

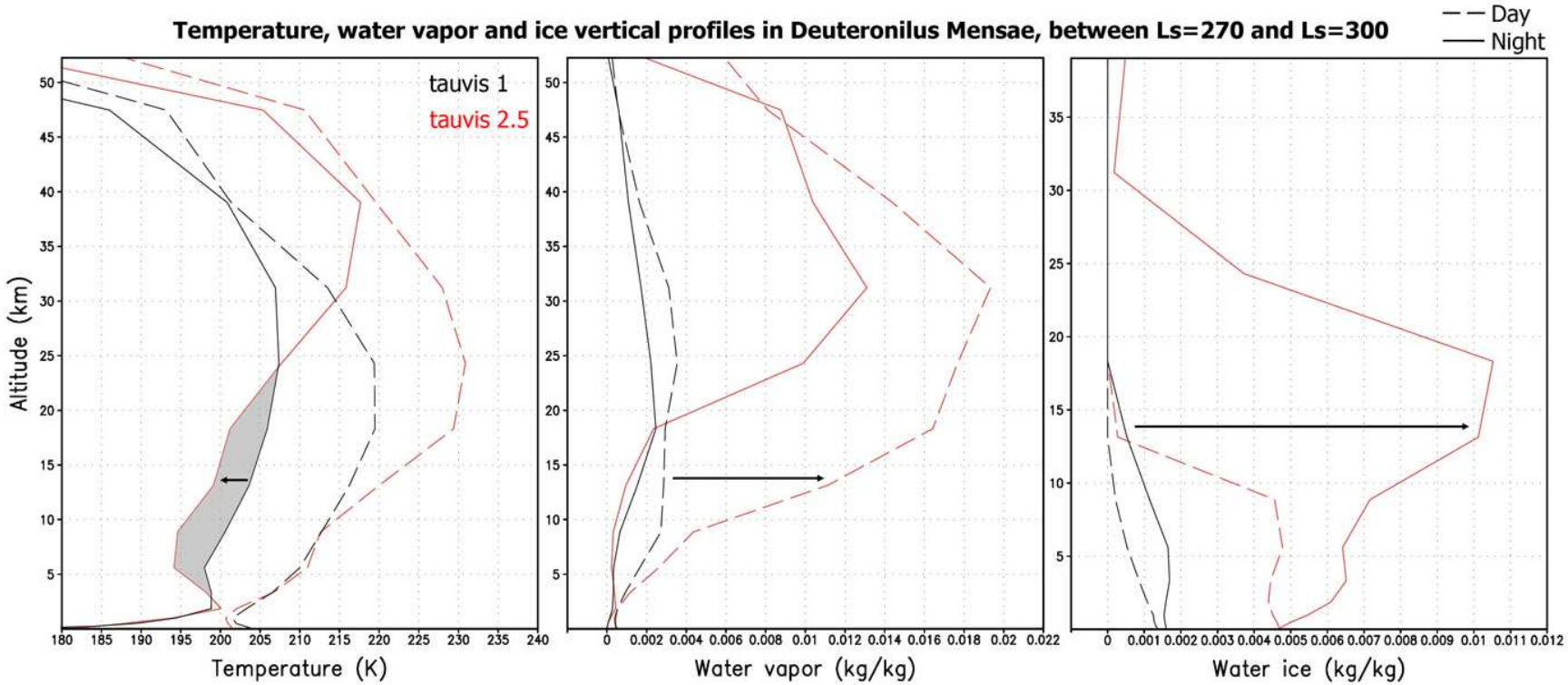

Figure C.12: Temperature (K) and water/ice mixing ratios over Deuteronilus Mensae during the northern winter. $\epsilon = 15$, $e = 0.1$, $L_p = 270^o$, $\tau = 1 - 2.5$ (black and red), water source : equatorial. Dash line = day - Solid line = night.

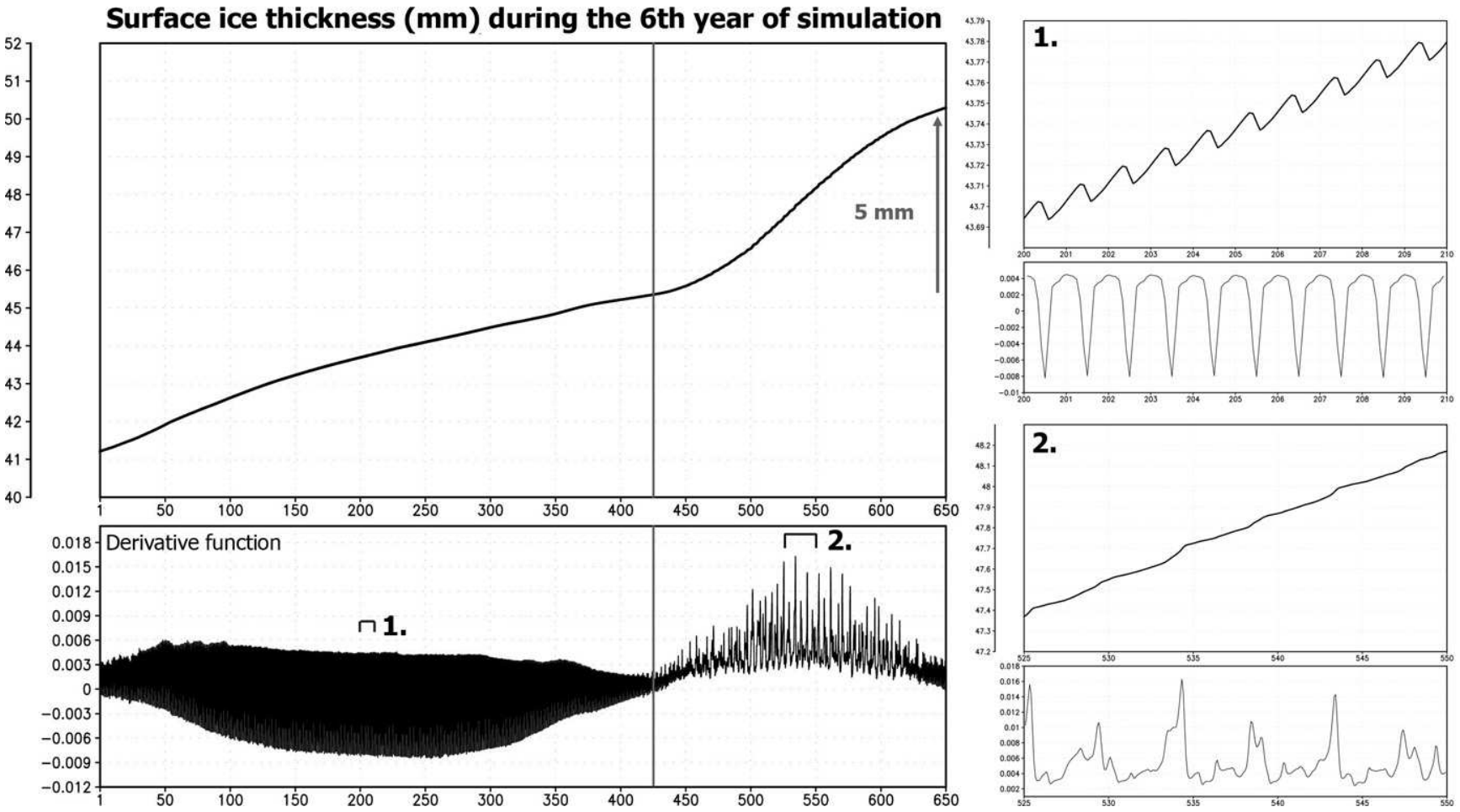

Figure C.13: Ice deposits thickness and derivative function (mm), with zoom on typical summer (1) and winter (2) variations.
$\epsilon = 15$, $e = 0.1$, $L_p = 270^o$, $\tau = 2.5$, water source : equatorial.

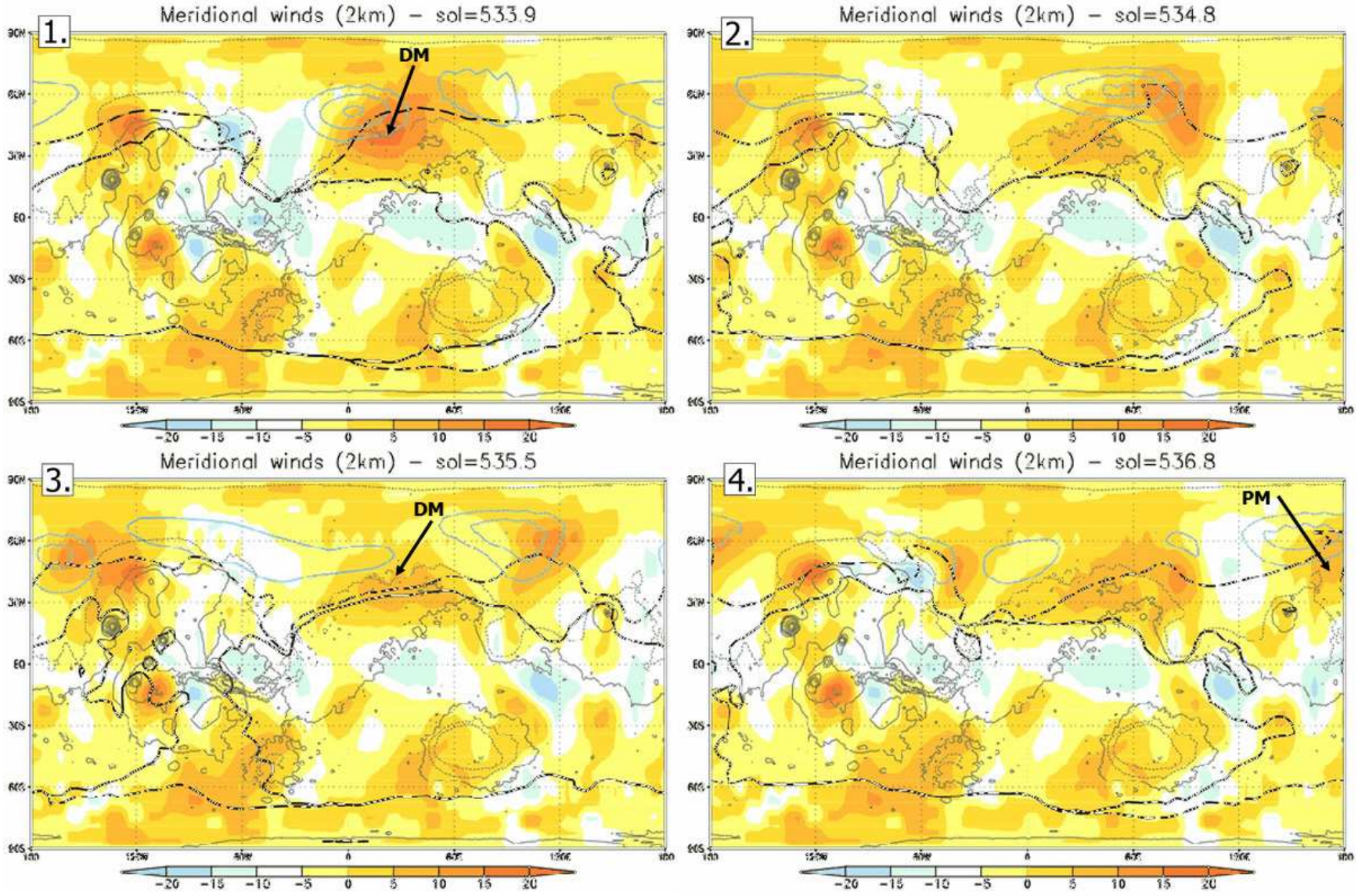

Figure C.14: Surface pressure perturbations (blue lines) and meridional winds (shaded colors), water vapor (black line), ice crystals (dotted line) at 2 km.

$\epsilon = 15$, $e = 0.1$, $L_p = 270^o$, $\tau = 2.5$, water source : equatorial.

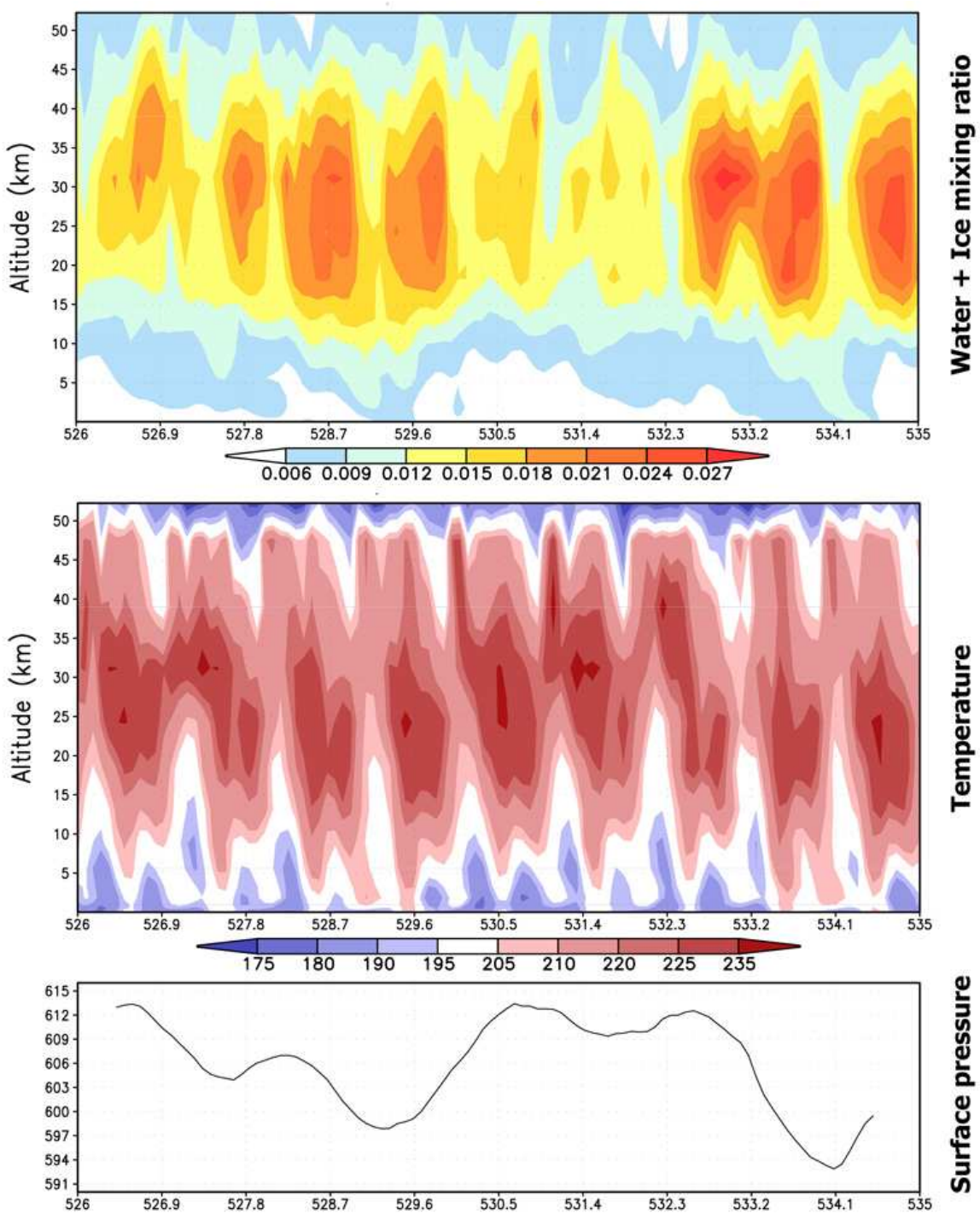

Figure C.15: Hovmoller plots of the water content, the temperature and the surface pressure during the passing of two low pressure systems over Deuteronilus Mensae.
$\epsilon = 15$, $e = 0.1$, $L_p = 270^o$, $\tau = 2.5$, water source : equatorial.
Surface pressure is given by a running average with a 1 day window.

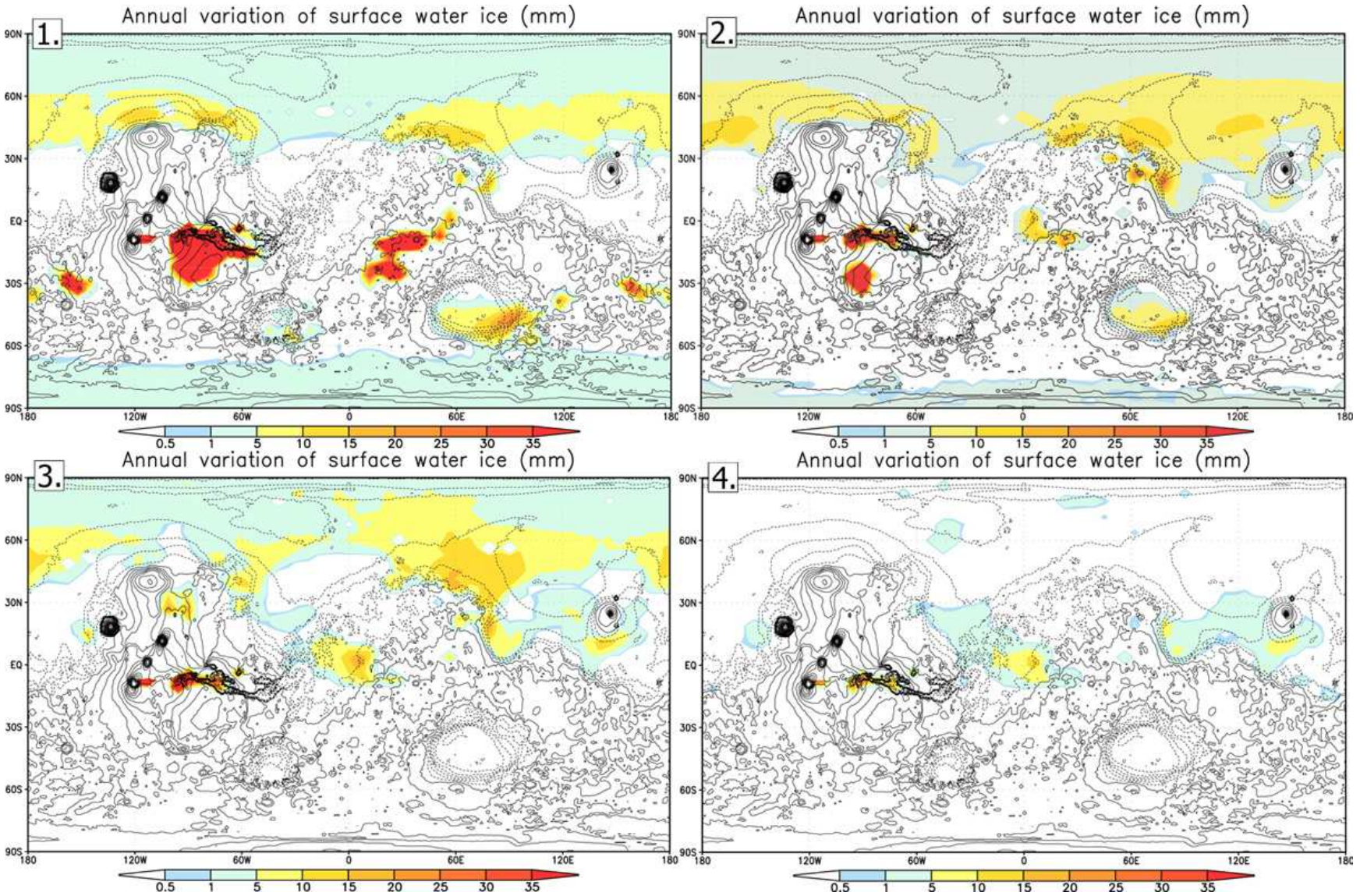

Figure C.16: Surface ice accumulation ($mm.yr^{-1}$) for the main set of simulations
$\epsilon = 15 - 25 - 35 - 45^o$, $e = 0.1$, $L_p = 270^o$, $\tau = 2.5$, water source : equatorial.

APPENDIX D

Images

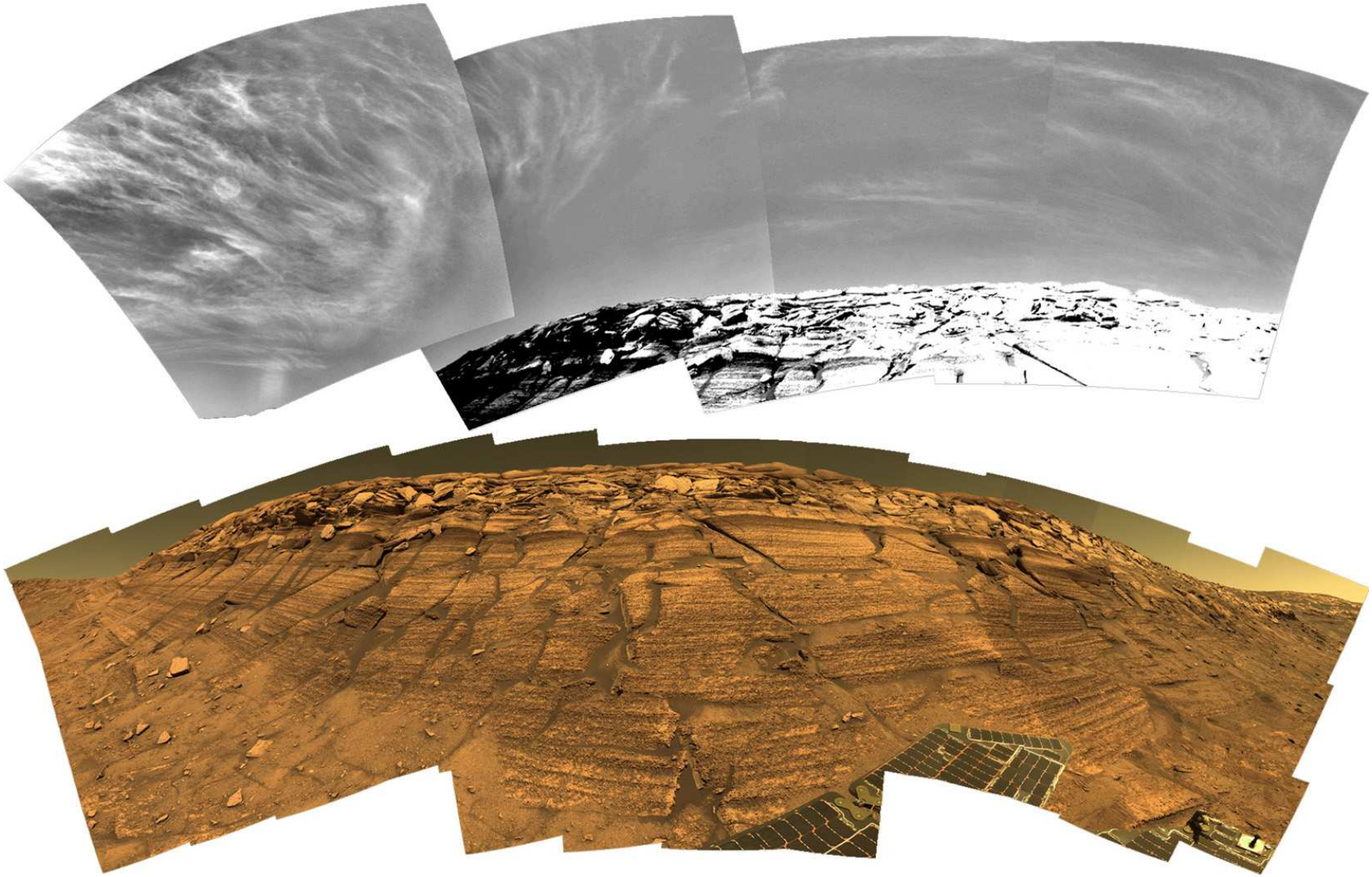

Figure D.1: Burns Cliff and cirrus clouds captured by the rover Opportunity, November 2004 ($L_s \simeq 74^o$)

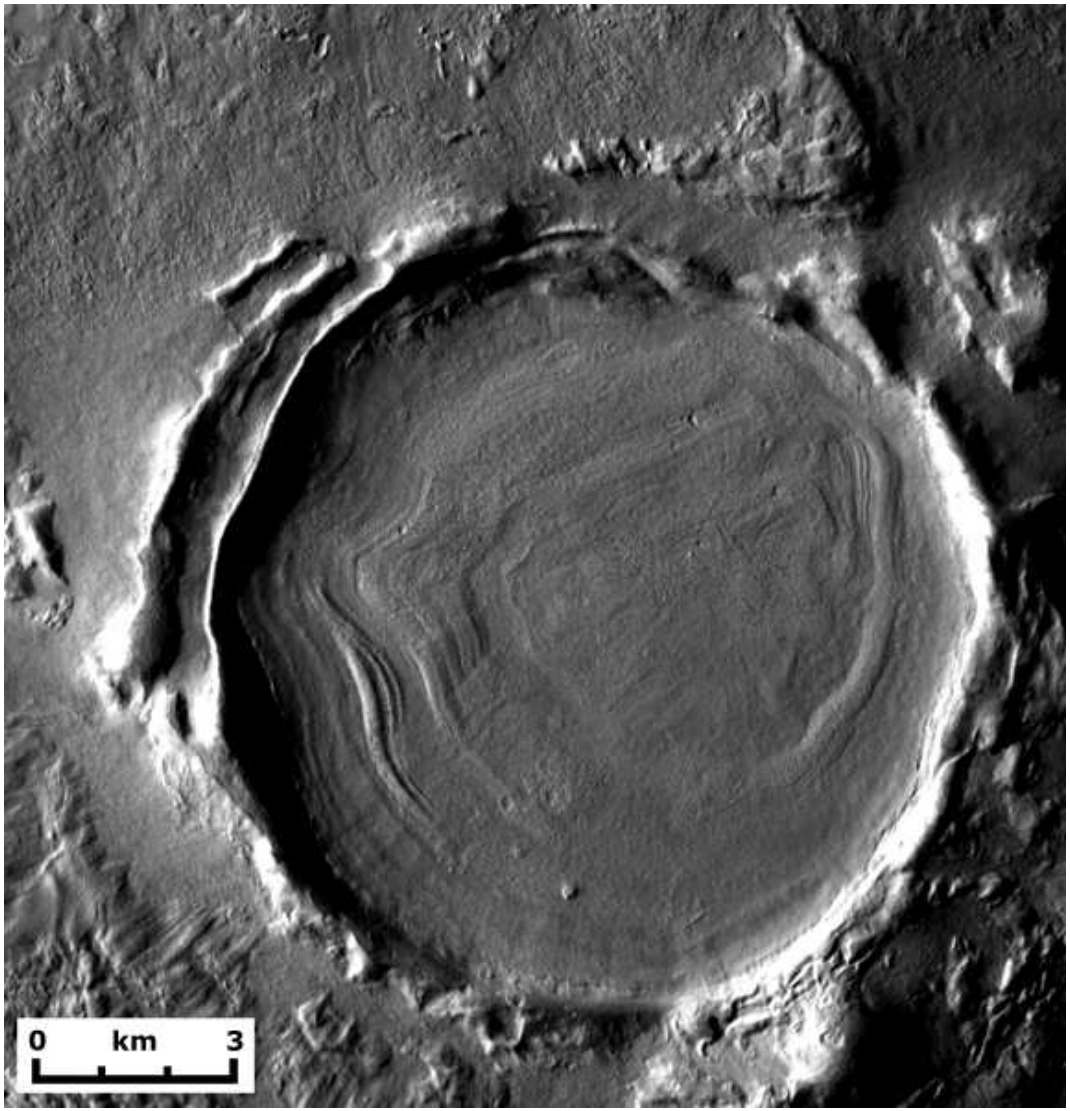

Figure D.2: Phlegra Montes 40^{o}N-165^{o}E : Viscous flow features inside a crater.
THEMIS image V11840006

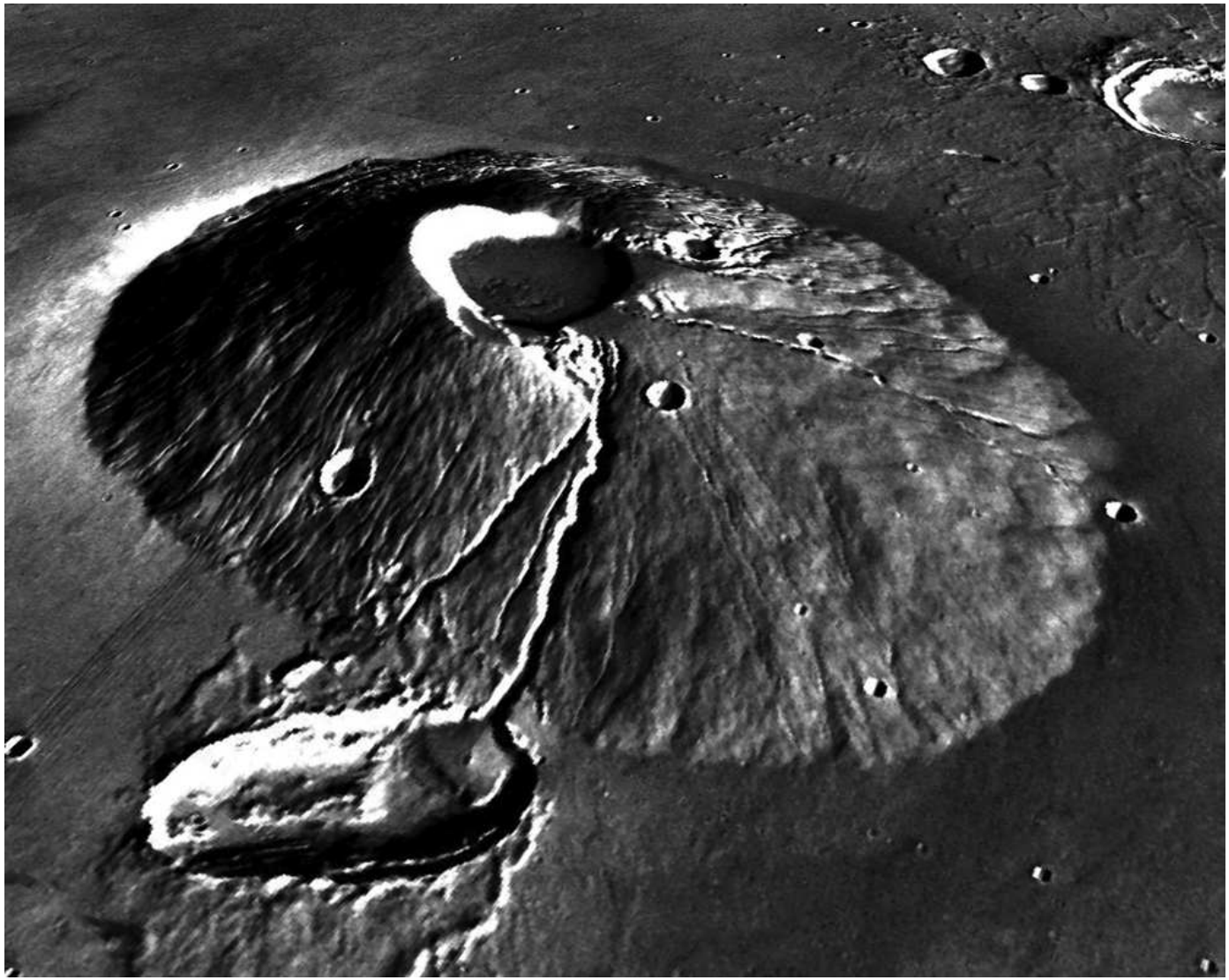

Figure D.3: Ceraunius Tholus 24^{o}N-97^{o}W : Radial channels on the flank of the volcanoe.
Mars Express HRSC image

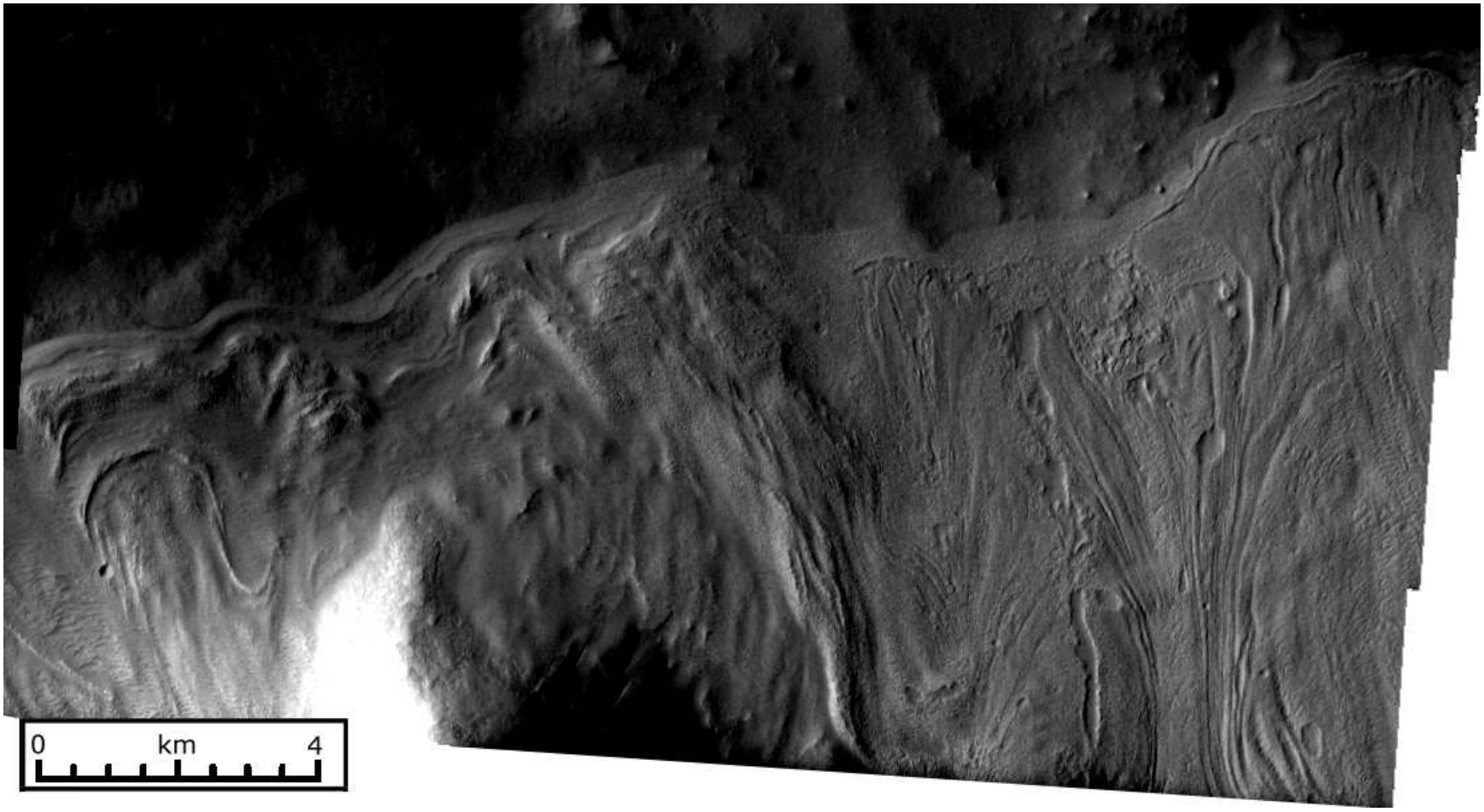

Figure D.4: Deuteronilus Mensae 40°N-30°E : Lobate debris aprons.
THEMIS image V12356003

Figure D.5: Ismeniae Fossae 40^oN-37^oE : Transition from lobate debris aprons to lineated valley fill.

THEMIS image V04406006